



Event reconstruction for Dark Photon searches at NA64

Dissertation

zur

Erlangung des Doktorgrades (Dr. rer. nat.)

der

Mathematisch-Naturwissenschaftlichen Fakultät

Fachgruppe Physik

der

Bergischen Universität Wuppertal

vorgelegt von

Srijan Sehgal

aus

Bonn

Wuppertal 2019

Angefertigt mit Genehmigung der Mathematisch-Naturwissenschaftlichen Fakultät der Bergischen Universität Wuppertal

1. Gutachter: Prof. Dr. Bernhard Ketzer
2. Gutachter: Prof. Dr. Jochen Dingfelder

Tag der Promotion:
Erscheinungsjahr:

Acknowledgements

(Rewrite ...) Even though this thesis has my name on the front a number of people were involved in shaping its final form both in person and in spirit.

First and foremost I would like to thank my late grandfather Shanti Sarup Sehgal and grandmother Kusum Sehgal. Their constant motivation and belief in my abilities has and will always inspire me to achieve more.

I am very grateful to Professor Bernhard Ketzer for giving me an opportunity to write my thesis in his group. In spite of my many shortcomings and failures he has always been patient and supportive during the entire time and has been a role model I look up to. I would also like to thank Professor Jochen Dingfelder. I have always admired your lectures and am thankful that you agreed to be my second supervisor.

A special thanks to PhD students Michael Hösgen and Martin Hoffmann for helping with the editing of this thesis. Thank you to Michael for always answering my various questions and solving my problems without which this thesis would have never been completed. A big thanks to the whole AG Ketzer group for both the academic and moral support.

I am grateful to my father Ravi Sehgal, my mother Rajni Sehgal and my brother Sambhav for all the sacrifices they have made. Without their constant support studying at Bonn would have just remained a pipe dream. Lastly, I am thankful to the wonderful set of friends I am lucky to have. Thank you Svenja ,Georgios and Amitayus for the countless Mensa lunches which helped me remain sane throughout the thesis.

Contents

1	Introduction	1
2	Ultra High Energy Cosmic Rays and Neutrinos	5
2.1	Ultra High Energy Cosmic Rays	5
2.1.1	History	5
2.1.2	Origin	6
2.1.3	Propagation	8
2.1.4	Latest results	10
2.2	Ultra High Energy Neutrinos	15
2.2.1	History	15
2.2.2	Origin and Propagation	16
2.2.3	Neutrino Interactions and Detection	18
2.2.4	Latest results	22
2.3	Multimessenger Astronomy	23
3	Extensive Air Showers	27
3.1	Development	27
3.1.1	Heitler's Toy Model	28
3.1.2	Hadronic Extension	28
3.1.3	LPM effect	30
3.1.4	Neutrino induced EAS	30
3.2	Characteristics	31
3.3	Detection	33
3.3.1	Fluorescence Detection	33
3.3.2	Cherenkov Detection	33
3.3.3	Radio Detection	34
3.3.4	Particle detector arrays	34
3.3.5	Towards detecting Neutrino Induced Extensive Air Showers	35
4	The Pierre Auger Observatory	37
4.1	Fluorescence Detector	38
4.2	Surface Detector	39
4.2.1	Calibration of SD	40

4.2.2	SD Trigger system	40
4.3	AugerPrime	43
4.4	The Offline Framework	44
4.4.1	Advanced Data Summary Tree	45
5	Neutrino Analysis $60^\circ < \theta < 75^\circ$	47
5.1	SD Neutrino signature $60^\circ < \theta < 75^\circ$	47
5.2	Neutrino Simulations	48
5.2.1	Atmospheric Shower simulations	49
5.2.2	Surface Detector Response	51
5.3	Shower Reconstruction	52
5.3.1	Event reading and pre-selection	53
5.3.2	Angular Reconstruction	55
5.3.3	Posterior selection and Export	57
5.4	Reconstructed ν simulations	57
5.5	ν selection	58
5.5.1	Samples Used	58
5.5.2	Pre-selection Cuts	59
5.5.3	Fisher linear discriminant analysis	60
5.5.4	Time evolution of selection parameters	63
5.5.5	Neutrino Detection Efficiency	64
6	Detector exposure and Limits to the diffuse flux	69
6.1	Exposure Calculation	69
6.2	Systematic uncertainties	71
6.3	Data unblinding	71
6.3.1	20% test sample	72
6.3.2	Reevaluated 20% test search sample and 60% search sample	72
6.4	Diffuse limit for the UHE neutrino flux	73
6.4.1	Feldman and Cousins limit	74
6.4.2	Rolke approach	74
6.4.3	Conrad approach	75
6.4.4	Final calculation	75
7	Source follow-up analysis	77
7.1	Procedure for point source analysis	77
7.1.1	Source visibility	77
7.1.2	Effective area and Exposure	78
7.2	Point-source neutrino flux limit	79
8	Conclusion and Outlook	81

Bibliography	85
A Testing hadronic models	107
B Adapting DGH analysis to current Offline	113
List of Figures	115

Introduction

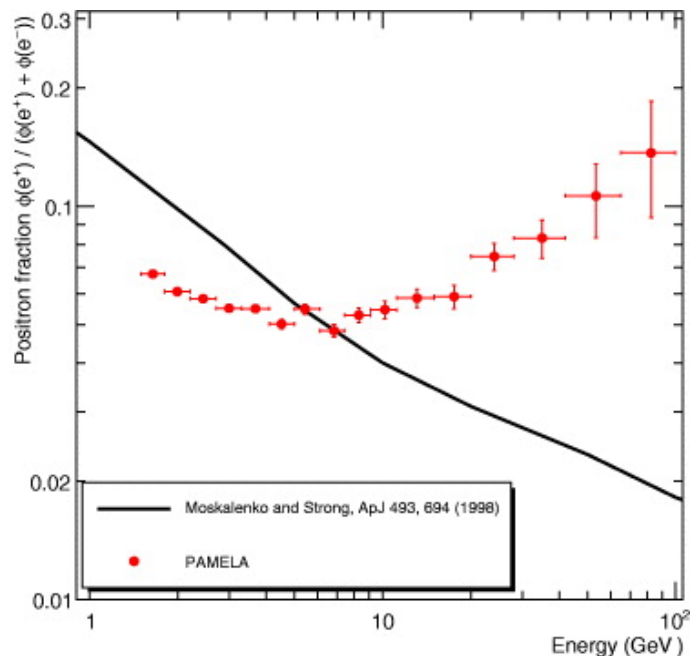


Figure 1.1: Positron fraction measured by PAMELA (red) along with a theoretical model (black) []

The need to understand how something works or why something is? is ingrained in every human. While attempting to find answers for these questions one either answers them conclusively or finds oneself asking additional questions stemming from the original. One such question which bothered physicists at the beginning of the 20th century and eventually led to the field of *astro-particle physics* was of so-called "atmosphere electricity" or ionization of air. After the pioneering discoveries by Theodor Wulf [1] and Victor Hess [2] who found the increase of this ionization rate with altitude and theorized the origin of this radiation to be not earth but something above our atmosphere, the name *cosmic rays* was coined by Robert Millikan who believed these rays were originating from primary photons. This hypothesis

Draw a fig. for introduction? The window?

was rejected by the measurements done by Jacob Clay [3, 4] in 1927 who observed a latitude dependence of the intensity of cosmic rays concluding this to be a deflection of the primary cosmic-rays(CRs) by the geomagnetic field of the earth which indicated that these rays must be charged particles. After this came the efforts of B. Rossi [5], German group [6] and P. Auger [7] all independently discovering coincident signals in separated Geiger counters which they explained by the counters being struck by an extensive particle shower triggered by a primary cosmic ray. The phenomenon was named *sciama* by Rossi, *Luftshauer* by the German group and "Auger showers" by Auger and his collaborators. Auger went one step further by further estimating the primary energy of the cosmic ray via his superior setup giving rise to some questions about CRs which are yet unanswered, how are they created and where are they coming from. One of the known sources which is the Sun is too close to explain some other high energy CRs constantly hitting the Earth's atmosphere. Since then the field has only expanded with numerous experiments set up to characterize these cosmic rays.

The biggest of these experiments which looks for ultra-high energy cosmic rays(UHECRs) exists in 3000 km² patch of Argentinian pampa just outside Malargue called the Pierre Auger Observatory [8]. It uses a combination of 1660 Water Cherenkov tanks which form the Surface Detector of the observatory and observe the air shower particles arriving at the ground along with Fluorescence Detectors/Telescopes which can look at the development of shower as it travels through the atmosphere. Built primarily to answer the question of the cut-off of the cosmic ray spectrum also known as Greisen–Zatsepin–Kuzmin limit(or GZK cut-off), the observatory has provided immense contributions not only in the field of CRs but also in the fields of Geophysics(elves) [9], Dark matter(composition) [10] and multi-messenger physics(neutrino+photon searches) [11, 12]. Currently, the Surface detector is undergoing an upgrade which will add a scintillator and radio detector on top of the Water Cherenkov tanks further increasing the sensitivity of the Observatory especially to the composition of the cosmic rays.

The non-electrical neutrality of the incoming CRs provides one of the biggest hindrance for finding their sources. This means that CRs do not travel in straight lines from their sources and are affected by the magnetic fields and can also interact with the matter along the way [13, 14]. Combined with the fact that the possible sources are light years away from us, without knowing the magnetic fields of the Universe it is very hard to detect the sources of CRs. Ultra High Energy Neutrinos ($\text{UHE}\nu_s$) can help in this challenging search for the sources of CRs [15]. Being electrically neutral and having a very low interaction cross-section these particles can travel large distances unaffected by the intervening matter and magnetic fields. Several scenarios which are discussed later in section. 2.1.4 describe how the $\text{UHE}\nu_s$ can be produced by cosmic-rays and can tell us about their sources. Moreover, $\text{UHE}\nu_s$ are also interesting as they can also help constrain or explain different production and propagation scenarios for various sources helping us see known astrophysical and cosmogenic objects in a new way. The success of IceCube Neutrino Observatory, a neutrino observatory located in the South Pole, in detecting the first astrophysical neutrinos and observations of the first steady source NGC 1068 [16] and transient source [17] have reinvigorated the astro-particle

field. The Pierre Auger Observatory has also contributed to the search for $\text{UHE}\nu_s$ by trying to detect the Extensive Air SHowers (EASs) that can be induced by them. With its stellar sensitivity at high energy, searches at Pierre Auger Observatory have provided some of the strictest upper limits on the diffuse flux of UHE neutrinos [18]. This has already led to constraints on various hypothesized models explaining cosmogenic neutrino production.

The last decade with the successes of LIGO/VIRGO [19] in measuring the first Gravitational waves and IceCube in detecting the first astrophysical neutrinos has also rekindled a field which displays the true spirit of harmony in science and is called multi-messenger astronomy. The aim of the field is to establish a network that can coalesce all the information available through various messengers via which we can see the Universe and maximise the resources and experiments available at Earth. This also allows us to understand the sources better since the observation or non-observation of different messengers can help constrain the mechanisms behind their functioning. The beginning of this field can be traced back to the observation of the first cosmic rays in conjunction with solar flares further cementing the important role Pierre Auger Observatory can play for this field. One of the most important success stories of this field is the August 2017 detection of the neutron star collision [20] first by the LIGO/VIRGO detector since the Gravitational waves are the fastest messengers and then 1.7s later by the Fermi Gamma ray space telescope and INTEGRAL. 11 hours later already alerted by these two experiments the optical counterpart was detected by multiple telescopes like Las Campanas Observatory and the Hubble Space Telescope. The event was also further seen in Ultraviolet(Neil Gehrels Swift Observatory), X-ray(Chandra X-ray Observatory) and radio(Karl G. Jansky Very Large Array). The non observation of neutrinos by both the IceCube and the Pierre Auger Observatory helped reach the important conclusion about the orientation of the jets which is hypothesized to be off-axis i.e. not pointing directly towards the Earth. Since neutrinos and Gravitational waves are the fastest of the messengers to reach the Earth, alerts issued by IceCube and LIGO/VIRGO are regularly used to follow up the events with other experiments. Subsequent observations of the blazar TXS 0506+056 [21] with IceCube, FERMI-LAT and MAGIC and the observations of neutrinos from the plane of the Milky Way galaxy [22] have helped establish the continued importance of multi-messenger astronomy.

In this thesis performance of one of the upgrades of the Pierre Auger Observatory done in 2013 is evaluated in the context of neutrino search. This upgrade consisted of introducing new triggers called Time over Threshold deconvoluted(ToTd) and Multiple of Positive Steps(MoPS) to reduce the muonic background and effectively decrease the energy threshold for the array. Such triggers can be particularly important in the context of neutrino searches between 60° - 75° since they help in getting a better signal background separation. The effect of these triggers for both the search of a diffused neutrino flux and point like sources of neutrinos is investigated. The thesis also focuses on maximising the previously done neutrino searches in the zenith region 60° - 75° by investigating and updating the analysis presented in [18], [23].

The thesis is structured as follows, The next chapter 2 gives the theoretical background for UHE cosmic rays and UHE neutrinos and other important messengers in regard to the

Pierre Auger Observatory. It also aims to discuss the various theoretical scenarios involved in their production and propagation. The chapter also aims to summarize the important recent results for these messengers and the various interesting open questions for them. The next chapter 3 describes the phenomenon of Extensive Air showers which is used to indirectly detect both the cosmic rays and neutrinos at the Pierre Auger Observatory. To continue with understanding the detection in a more experimental context the next chapter 4 gives a detailed description of the Pierre Auger Observatory. The objective of the chapter is to try to give an exhaustive description of all the tools at the Pierre Auger Observatory necessary to detect neutrinos with a particular focus on the Surface Detector which is of primary concern for the analysis presented in this thesis. A small section is also dedicated to the recently completed AugerPrime upgrade and the exciting potential it offers especially for multi-messenger searches.

The second part of the thesis is dedicated to the neutrino search in the zenith angular region 60° - 75° (Down-going low, DG_{low}). This part begins with the chapter 5 that gives a description of the neutrino search in the angular range 60° - 75° which is also the primary focus region for this thesis. The chapter is dedicated to provide a complete description of the choices made for the analysis with the proper reasoning. It reports the areas of potential improvements and also communicates the observed improvements to the neutrino search with the new triggers. A new *blind* search is performed to look for neutrinos in the data recorded at the Pierre Auger Observatory. The results are summarised at the end of this chapter and due to the non-observance of any neutrino like events, the corresponding limits to the neutrino flux are presented. The Observatory can also detect showers in zenith angle range 75° - 90° (Down-going high, DG_{high}) and up-going showers in the zenith angular region 90° - 95° (Earth-skimming, ES) with the Surface Detector and 90° - 180° (???) with the Fluorescence Detector, but these searches are not performed in this thesis and only their final results are included for comparison and to provide a holistic feel for the neutrino search at Pierre Auger Observatory.

The last part of this thesis presents an example of a neutrino follow-up analysis for point-like sources in chapter 7. Due to the non-observance of any neutrinos in the data at the Pierre Auger Observatory an upper limit set by this analysis is also provided for interesting point source neutrino candidates. All the important results are then finally summarised in chapter 8 and a short outlook of the future directions for the analysis and the neutrino search at the Pierre Auger Observatory is put forward. The dissertation is completed by three appendices. The first describing the independent work done to compare the various hadronic interaction models for neutrino simulations and the second contains a technical overview of the changes made to implement the 75° - 90° neutrino search within Offline, the software framework of the Pierre Auger Observatory.

Ultra High Energy Cosmic Rays and Neutrinos

2.1 Ultra High Energy Cosmic Rays

2.1.1 History

As already mentioned in the introduction cosmic rays have been a source of investigation for more than a century now. Even before the balloon flight by Victor Hess, it was Henry Becquerel, the discoverer of radioactivity who believed that the *atmospheric electricity* (ionization of air) was due to the radioactive substances present on Earth. In such a scenario the ionization rate should decrease the higher up you go in the atmosphere. The first measurements disproving this theory were performed by Theodor Wulf in 1909 with his own developed electrometer. His measurements published in the *Physikalische Zeitschrift* indicated a higher level of radiation at the top of the Eiffel Tower as compared to its base. Unfortunately, the measurements were not widely accepted, and it would take three years till Victor Hess via his several balloon flights provided irrefutable measurements corroborating Wulf's observations.

Between 1911 and 1912 Victor Hess performed nine (2 in 1911 and 7 in 1912) balloon flights going as high as 5350 m a.s.l to measure the dependence of ionization rate to altitude. He carried with him three Wulf electrometers, two tuned for γ rays and the third tuned for β rays [24] which along with α were the only three known radioactive decays. His measurements published in the Proceedings of the Viennese Academy of Sciences [2] showed that the radiation level decreased slightly up to a certain altitude (1 km) but after this height, the radiation increased significantly and at the highest flown altitudes reached levels about twice in comparison to the ones at sea level. Some of his measurements were done during the night and one during a partial solar eclipse which further made him rule out the Sun as a source of this radiation. With further confirmations via the measurements by Werner Kolhörster in 1914 and Robert Millikan, in 1925, Victor Hess was awarded the Nobel

Prize in Physics in 1936.

Cosmic rays were still presumed to be gamma rays. This supposition was quickly negated by the efforts of Jacob Clay who via his measurements of the cosmic ray intensity at different latitudes while sailing from Java to the Netherlands in 1927 [3] showed that the geomagnetic field had a significant effect on the intensity. Further observations of the *East-West* effect, the directional dependent intensity due to the charge of the primary cosmic rays, predicted by Bruno Rossi [25], by various experiments [26] [27] concluded that the intensity was greater from the west proving that cosmic ray primaries have a positive charge.

Today we use CRs to describe the highly energetic charged particles/nuclei travelling at very high speeds through space. The Earth is constantly bombarded by CRs, some originating from the Sun but most of them from outside our Solar System. In more than 100 years since Victor Hess's balloon flight, we have gathered a lot more information and have achieved a better understanding of CRs. We have detected CRs up to to energies 10^{20} eV [28] which is an impressive feat since at these energies the expected flux drops below one particle/ km^2 . We know a lot more about the composition of the CRs and have also proposed models explaining their origin and their journey to Earth. CRs continue to be a source of fascination. Some of the achievements are summarised below along with some unanswered questions about CRs.

2.1.2 Origin

To understand the sources of cosmic rays one needs to understand the mechanisms that could impart huge amounts of energies to the tiny particles that actually reach the Earth. We already know that the low energy CRs which reach our Earth are predominantly coming from the Sun. The evidence for this comes from the observation of an increase in these with a coincidence to the violent activity of the sun. Most of the CRs and Ultra High Energy Cosmic Rays (UHECRs, $E > 10^{18}$ eV) do not exhibit this temporal coincidence and are thought to have originated in our Galaxy or beyond respectively. Two different mechanisms could explain how the CR particles are accelerated to such high energies over large distances: *bottom-up* [29–31] and *top-down* [32, 33]. The *top-down* approach assumes that the UHECRs are produced due to the decay or annihilation of extremely massive or exotic particles. Both of these mechanisms have been investigated with various experiments including the Pierre Auger Observatory. With the current observations, the top-down models face significant challenges. The extremely high energies required for the annihilation of the hypothesized exotic particles and the lack of evidence for their existence make it very difficult to both verify and rule out the top-down mechanism. The continued improvement in understanding of astroparticle physics and the early universe makes the study of UHECRs an exciting and active area for research with the mystery of their origin and propagation still waiting for a solution.

Bottom-up scenario

There are many proposed ways in which CRs could get accelerated by astrophysical sources. One of the most widely accepted descriptions that can explain most of the observed CRs that originate from our Galaxy is the diffusive shock acceleration also known as Fermi acceleration [34]. Qualitatively one can explain Fermi acceleration as follows: When a massive star reaches the end of its life cycle it can undergo a supernova explosion. During this, the star core collapses and an intense shockwave propagates outwards towards the star's outer layers. As the shock wave progresses and moves through the interstellar medium (ISM) it sweeps up and compresses the surrounding gas and magnetic fields creating a region of very high pressure and magnetic turbulence known as the shock front. The charged particles can get trapped in such a shock front and repeatedly cross over this region of magnetic turbulence experiencing magnetic irregularities and constantly changing direction in a collision-less way thus experiencing electric fields each time they cross which accelerate them to higher energies. An illustration is shown in fig. ???. The shock front is turbulent, and particles can cross it multiple times, gaining energy at each passage. Eventually, some particles can acquire enough energy to escape the shock region and travel the required distances to reach the Earth. Such an explanation can explain the CRs originating in our Galaxy and point towards supernovae and its remnants as potential sources but to explain the UHECRs ($>10^{19}$ eV) we need other sources and mechanisms. The energy that can be produced by the accelerator is limited by the gyroradius of the accelerator. This has been illustrated by Hillas [29] where he illustrated the potential sources of CRs on a plot of magnetic field strength vs size. A modified version of his original plot with the inclusion of modern sources is shown in Fig. ???.

Other accelerating mechanisms are as follows:

1. Supernova Remnants: Interactions of CRs with the magnetic fields within the remnants could lead to further acceleration [35].
2. Active Galactic Nuclei (AGNs): These are regions in the centre of galaxies that are capable of producing highly energetic particles. The source of this capability is theorized to be supermassive black holes. The extreme conditions near the black holes such as strong magnetic fields and high-energy jets could accelerate UHECRs. [36]
3. Magnetar Outbursts: Magnetars are neutron stars having a magnetic field 1000 times that of a normal neutron star. They are known to produce magnetically powered bursts which could potentially accelerate particles to UHECR level energies. [37]
4. Pulsar Wind Nebulae: Rapidly rotating neutron stars, also known as Pulsars emit beams of electromagnetic radiation. Such beams can collide with ISM creating a pulsar wind nebulae, a region similar to a shock wave front and can lead to production of UHECRs. [38]
5. Galaxy Clusters: These are regions of massive galaxy populations bound together by gravity. These highly dense structures can accelerate particles either by themselves or via the shock waves associated with a potential merging of different galaxy clusters. [39, 40]
6. Relativistic shocks: Other types of astrophysical shocks such as those occurring in gamma-ray bursts or colliding stellar winds could also create scenarios that could accelerate

particles to UHECR level energies. [41, 42]

The validity of all such hypothesized mechanisms can be checked by corroborating their spectral index predictions with those observed by the experiments.

Top-down scenario

This is an alternative approach to explaining UHECRs. The main idea behind these models is that the UHECRs are produced due to the decay or interaction of hypothetical, supermassive, or exotic particles that were produced in the early universe. Some of the proposed hypotheses are mentioned below:

1. **Supermassive Dark Matter Particles:** This is an extension of a concept that was first proposed to explain dark matter. In this hypothesis, it is assumed that dark matter is composed of long-lived supermassive particles. If such particles exist they could potentially decay and produce UHECRs. [43, 44]

2. **Cosmic Strings:** These are one-dimensional topological defects that could have formed during phase transitions in the early Universe. The decay of these massive strings could also lead to the production of UHECRs. [45, 46]

3. **Other Topological effects:** These include defects like monopoles or domain walls which could also produce exotic particles which can further decay into UHECRs. [47]

There are other scenarios such as the breakdown of Lorentz invariance which attack the problem of UHECRs not by suggesting a new mechanism for their production but their propagation which can also have a major effect on the observations of CRs and UHECRs we observe on Earth. Some of these models can be constrained by again looking at the flux of the UHECRs. There are also experiments that try to directly look for these exotic particles []. So far, no evidence has been found to support the existence of these particles.

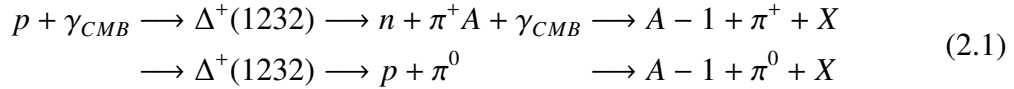
2.1.3 Propagation

However, production is just one part of the life of CRs/UHECRs. To get detected on Earth the CRs and UHECRs have to travel large distances through ISM during which they can suffer various losses which ultimately affect the spectrum we see on Earth. Some main processes include losses by ionization due to collision with ISM, Coulomb Scattering which can cause random changes to the direction, and Synchrotron Radiation which can lead to the emission of high energy photons and, consequently, energy loss for the cosmic ray particle and through collisions with high-energy photons from radiation fields leading to breakage of CR nuclei also known as Photo-disintegration. Other propagation effects such as Bremsstrahlung and Inverse Compton Scattering due to interactions with the cosmic microwave background radiation (CMB) are the reasons high energy cosmic ray electrons cannot propagate large distances. A few other mechanisms include Adiabatic Energy Loss which can occur when a CR particle traverses through regions of high pressure or magnetic field strength to regions of lower pressure and magnetic field strength leading to a decrease in its velocity, Scattering due to going through magnetic turbulent areas or even an escape of UHECRs from our

Galaxy can all affect the spectrum of CRs and UHECRs we see at Earth. One of the critical phenomena to understand cosmic ray propagation and to realize a theoretical limit to the energy of UHECRs is the Greisen-Zatsepin-Kuzmin (GZK) cutoff. This is discussed in more detail below.

GZK Limit

The GZK cutoff was first proposed by Kenneth Greisen, an American physicist in 1966 in a paper titled "End to the Cosmic-Ray Spectrum?" [48]. He discussed the potential energy loss of high-energy cosmic rays due to interactions with the CMB. He calculated a threshold energy above which cosmic rays in his case protons would lose energy through interactions with CMB. In the same year, two Soviet physicists, Georgiy Zatsepin and Vadim Kuzmin, arrived at a similar prediction. Their calculations published in their paper "Upper Limit of the Spectrum of Cosmic Rays" [49] were consistent with Griesen's work and reinforced the concept of the GZK cutoff. The energy cutoff calculated is about 5×10^{19} electronvolts(eV) or about 8 joules. The dominant mechanisms via which the proton can interact with the photons of the CMB are given below.



These processes are also called "Photopion Production". The thresholds for these reactions are of the order of a few hundred megaelectronvolt ($\text{MeV} = 10^6 \text{eV}$) for protons and GeV per nucleon for other nuclei. The predicted cutoff for protons is 50 Exa-electron-volt ($\text{EeV} = 10^{18} \text{eV}$) whereas for heavy nuclei it can range from about 80 EeV to several hundred EeV depending on the mass of the incident nucleus. The mean free path which represents the average distance a cosmic ray particle can travel before undergoing a significant interaction is 6 megaparsec (Mpc) for protons. This leads to the outcome that if a UHECR proton with energy above the GZK cutoff travels over a distance larger than 50Mpc then such a proton will suffer catastrophic losses and will never be observed on Earth. However, this consequence doesn't hold for heavy nuclei since for them Photopion production is not the dominant process via which they can lose energy. For ultra-high-energy cosmic rays (UHECRs) composed of heavy nuclei (e.g., iron, uranium), the dominant energy loss process during their propagation through the universe is photodisintegration. It can be described as:



The mean free path is still of the order of $\sim 10 \text{Mpc}$. Even though, the Pierre Auger Observatory observes a suppression in the cosmic ray spectrum above the GZK cutoff [50], it does not claim it to be just due to GZK limit. It has also observed cosmic rays above the GZK cutoff. This issue along with its implications is discussed later in sec. 2.1.4. One of the other

consequences arising from the interaction with the CMB is the interaction of high energy photons(gamma rays) to produce electron-positron pairs, $\gamma_{UHECR} + \gamma_{CMB} \longrightarrow e^+ + e^-$. This is an important consequence that alters both the expected UHECR spectrum and the CR spectrum at Earth and also just leaves neutrinos as one of the only known cosmic ray particles that can point back directly to their sources.

The production of these high energy neutrinos arising from the pions produced during the Photopion interaction is discussed later in sec. 2.2

2.1.4 Latest results

The study of CRs to constrain their properties and the relevant sources requires measurements on Earth. The measurements which provide valuable information are the energy spectrum or flux observed at Earth, the composition of the primary CRs arriving at Earth, their arrival direction and other relevant observations such as measurement of other messengers such as high energy photons and neutrons. These measurements and their implications are discussed in more detail below. The high energy neutrinos, relevant for this thesis are discussed in a separate section.

Cosmic Ray spectrum

The cosmic ray spectrum measured by several experiments on Earth is summarised in figure. ???. Extending in energy from a few 100 MeV(solar CRs) it spans about 12 orders of magnitude up to the highest observed CRs 10^{20} eV. The flux decreases with increasing energy and follows a varying power law description:

$$\frac{dN}{dE} \propto E^{-\gamma} \quad (2.3)$$

where γ is the spectral index. The spectral index varies between 2.7 to 3.3 as measurements are made for higher energies. This signifies a decrease in the observed flux as the energy increases. The flux falls from $\sim 1\text{m}^{-2}\text{s}^{-1}$ at 10^{11} eV to $\sim 1\text{m}^{-2}\text{yr}^{-1}$ at 10^{16} eV to about $\sim 1\text{km}^{-2}\text{yr}^{-1}$ at 10^{19} eV. Such a steep fall also poses challenges for the experimental design and the corresponding size. This also affects the detection mechanisms employed to measure this spectrum, due to the very low flux expected at high energies, the measurements of the direct primaries become nearly impossible and an indirect detection using the property of the cosmic ray to trigger an air shower in our atmosphere is employed. This phenomenon and how it is used to measure CRs is discussed in the next chapter 3.

To better deduce the features in the cosmic ray spectrum one can scale the flux in the fig ?? by energy. The corresponding figure is shown in Fig. ??. Below 10^{13} eV CRs from the Sun dominate the spectrum. The galactic or extragalactic CRs of these energies cannot enter our solar system because of a variety of reasons. These include a combination of the Heliosphere, Termination Shock and solar modulation which block the low energy CRs. The Heliosphere which is a region influenced by the Sun's magnetic field and solar wind acts

as a protective bubble around the solar system. Beyond the Heliosphere, the solar wind interacts with the ISM creating a region of termination shock which can cause scattering and deflection for incoming low energy CRs. Additionally, the solar activity cycle can cause changes to the Heliosphere which in turn also affects the incoming CRs. Beyond a few gigaelectronvolts ($\text{GeV} = 10^9 \text{eV}$) the Sun as a source of CRs drops off due to reaching its maximum acceleration potential. Between 10^{13}eV and 10^{18}eV the spectrum is dominated by CRs of galactic origin. This has been verified by comparing the spectral indices of the proposed acceleration mechanisms with the measured spectrum as mentioned before. A second proof also comes from the composition of the CRs observed in these energies, but this is discussed later. *Supernovae* and *supernovae remnants* remain the most promising sources which could explain their origin. The spectral index, $\gamma \sim 2.7$ gives a good description of this region. Around 5×10^{15} one observes a steepening of the spectrum known as the *knee*. At this point γ changes from 2.7 to 3.1. This is attributed to the galactic accelerators reaching their maximum potential for accelerating protons. Above the knee, the sources are expected to reach their maximum potential for other heavier particles until galactic sources cannot accelerate CRs any further. This point is thought to be the origin of the second knee at 10^{17}eV . At this point the γ changes from 3.1 to 3.3. This is theorized to be a transition region in which the spectrum is believed to change from one of galactic origin to extragalactic origin. This region ends at about 10^{18}eV whereon the spectrum hardens noticeably to a $\gamma \sim 2.6$, originating what is referred to as the *ankle*. Further, with increasing energy the spectrum again steepens to $\gamma \sim 5.1$ reaching an eventual cutoff. The suppression of flux at these energies and the cutoff is still not properly understood yet and could be due to the following possibilities:

1. **GZK Limit:** One of the most prevalent ideas behind the suppression and the cutoff is the GZK mechanism which was discussed above. Due to the observations of CRs above the cutoff of 10^{19}eV by the Pierre Auger Observatory and a non-observance of expected composition(non-proton primaries) and neutrino flux(GZK pion decay), GZK as the only reason for the observed cutoff in the spectrum is currently disfavoured. However, tensions between the composition measurements of the Pierre Auger Observatory and the Telescope Array (TA) [51], the second-largest CR observatory, make this topic still a subject of debate.

2. **Maximum Rigidity:** In this scenario, the cutoff is due to the sources of the extragalactic CRs reaching their maximum potential for acceleration for different particles i.e. maximum rigidity. Such a scenario is already observed in the spectrum for Galactic sources(*knee*). An indirect proof of this mechanism can come from the observed composition from the *ankle* region to the cutoff. If the composition shifts from lighter to heavier nuclei this would be proof of a cutoff at the potential extragalactic sources.

3. **Photo-disintegration:** This effect was also discussed before in sec. 2.1.3. However, for such a scenario the cutoff would appear in steps depending on the mass of the nuclei.

It is likely that the cutoff and the suppression are not just because of one of the above-mentioned scenarios but are due to a combination of all three. In theory, GZK and Photo-disintegration could explain the observed spectrum but the non-observance of GZK neutrinos and the composition measurements gather otherwise. It also shows that even though the CR

spectrum gives a very nice overview, other crucial measurements of composition and multi-messengers play an equally important ally to the spectrum measurements for constraining the origin and propagation of CRs.

Cosmic Ray composition

The types of particles the cosmic ray flux at Earth is made up of is called the cosmic ray composition. Such measurements with respect to energy offer a very useful insight into their origin. Direct measurement of the primaries is only possible for low energies and one e.g. is the AMS detector at the International Space Station [52]. For higher energies, the mass of the primary is reconstructed by measuring the phenomenon of Extensive Air Shower(EAS) which is described in more detail in Chapter 3. EASs are created when high-energy CRs interact with the Earth's atmosphere producing a cascade of particles resembling a shower. Depending on the mass of the primary, the EAS induced in the atmosphere by the said primary has characteristic differences. For the same energy lighter nuclei such as protons will interact and produce an EAS much deeper in the atmosphere compared to heavy nuclei such as iron. There are various ways one could estimate the mass of the primary. The estimator used for this at the Pierre Auger Observatory is $\langle X_{max} \rangle$ which is the average depth at which the EAS development in the atmosphere reaches a maximum. The $\langle X_{max} \rangle$ values are also energy dependent, and it is observed that iron nuclei typically have values 100 g cm^{-2} lower than proton. The fluctuation in the spread can also be used to gauge the mass. For e.g. fewer fluctuations are expected for iron compared to proton. Other quantities such as the lateral distribution of the shower which is just the number of particles in a shower as a function of distance from the point of first interaction (core) also show differences based on the primaries. For lighter primaries, the distribution is broader i.e. the number of particles decreases more gradually with distance from the core compared to a narrower distribution in the case of heavier primaries. The ratio of electromagnetic to muonic components first used by KASCADE [53] can also be used to differentiate between the primaries, the lighter primaries have a greater electromagnetic component whereas the heavier primaries have a greater muonic component in the initiated EAS.

The process of estimating the mass requires a very robust simulation that can reconstruct an EAS perfectly for a certain primary and a direct observation of X_{max} . At the Pierre Auger Observatory The Fluorescence Detector, cf. section 4.1, is used to directly measure the X_{max} on an event by event basis. The recent results from the Pierre Auger Observatory are shown in fig ?? . In both the figures the composition initially turns lighter and then seems to change from lighter to heavier nuclei at E 18.5 EeV. This could be an indication of the switch from a galactic component to an extragalactic component around the *ankle* consistent with the maximum rigidity scenario as mentioned in the section above.

However, the duty cycle of the Fluorescence Detector 14% compared to the Surface detector 100% leads to very limited statistics. Currently, this problem is solved by defining a new observable described in [54] which has helped increase the number of events used to estimate the mass composition by nearly 14 times. The results for this are shown in fig. ??.

Additionally, the energy dependent mass composition can be fitted simultaneously with the cosmic ray spectrum observed at the Pierre Auger Observatory with the only required assumption being about the model used to produce and propagate the cosmic rays from the sources. The result of one such analysis [55] is shown in fig ?? . With the current Pierre Auger Observatory measurements for different mass components are required to best describe the data with proton component completely disfavoured for the highest energies.

The future advancements of the AugerPrime [56] will further increase the capability of the Pierre Auger Observatory in measuring mass composition. The addition of a Radio Detector can present an independent measurement of the X_{max} offering an important cross-check on the Fluorescence Detector measurement.

re-write
after look-
ing at the
paper

Cosmic Ray arrival directions

Even though the CRs are mostly charged particles and can easily get deflected by the magnetic fields [57] present in the cosmos one can still estimate the arrival directions of these CRs with the help of a good pointing resolution and an understanding of these magnetic fields. The pointing resolution depends on the detector and the Pierre Auger Observatory already has an excellent pointing accuracy of 0.7° [58]. The magnetic fields on the other hand are complicated to deduce and model. However, this lack of knowledge can be ignored by just looking at CRs of high energies since the expected deflections for such CRs are expected to be small. At Pierre Auger Observatory the arrival directions of more than 2,600 CRs above 32EeV were estimated and analyzed to look for potential sources of these CRs [59]. The results are shown in Fig. ?? The figure clearly shows the presence of Anisotropies which are deviations from uniformity across the sky. The anisotropies are also pointed away from the Galactic centre indicating that the UHECRs have an extragalactic origin. The hypothesis is further confirmed by the increase in anisotropy with energy shown in []. The presence of these anisotropies not far from the Galactic spiral arm as shown in fig ?? also gives further proof of an extragalactic origin of these UHECRs. Further, for low energies $E > 0.03$ EeV studies looking at large scale structures such as dipolar flux modulation in [60] also show a shift of the anisotropy dipole more towards the galactic center with decreasing energy with a significance of 6σ . This can again be interpreted as a transition in CR sources from Galactic to extragalactic component. Even though this result is corroborated by the measurements done by KASCADE-Grande, IceCube and IceTop due to the decrease in sensitivity of the Pierre Auger experiment for these energies the result is not conclusive yet.

Some proposed sources for these UHECRs due to observations of excess UHECRs in their surrounding regions by the Pierre Auger Observatory are presented in [61](ICRC proceeding). These include the Centaurus A region(4σ significance), starburst galaxies(3.8σ) such as NGC4945, M83 and NGC253. The Telescope Array has also found an excess close to the Perseus-Pisces supercluster(PPSC) with a significance of $3.0-3.2\sigma$. However, this has been negated by the Pierre Auger Observatory and remains a topic of discussion. With the continued data taking and upgrade of the Pierre Auger Observatory, the excess in the Centaurus A region is expected to reach a 5σ significance by 2025 which could make it the

first steady source of UHECRs ever observed.

Other Messengers

The scenarios for the production and propagation of CRs discussed above also predict the production of other messengers such as photons, neutrinos and neutrons. Neutrons and photons are discussed in this section and neutrinos are discussed in the next. Neutrons being neutral and thus not affected by the magnetic fields of the Universe during their propagation can be useful for arrival direction studies. They are expected to be produced at the CR source via photopion production or other nuclear reactions near the sources. One such e.g. is a collision between an ultra-high energy proton to an ambient proton/photon. Although, neutrons can lose a significant amount of their acquired energy very quickly via β decay (mean lifetime 879 s) [62] in the ultra-relativistic regime neutrons originated in our Galaxy can still make it to Earth. At Auger, a neutron produces a non-distinguishable EAS as compared to a proton. Hence, only a source catalogue correlated search can be performed at the Pierre Auger Observatory. The results of such a search are given in [63]. No neutron like events have been found at Auger, but these results have already helped constrain some theorized production mechanisms for CRs. Future searches looking at transient or short-lived sources for neutrons are currently underway.

Photons again offer another window to look into the origin, propagation and sources of the CRs. They can either be produced via interactions of CRs with matter or radiation fields or during propagation through interactions with the CMB as mentioned in sec. 2.1.3. They along with neutrinos can also help constrain various top-down scenarios and help paint a more complete picture of the CR landscape. Observations for high energy photons have been carried out by specialized experiments such as ground-based Cherenkov telescopes like the High Energy Stereoscopic System (HESS) [64], Fermi Gamma-ray Space Telescope [65], and the upcoming Cherenkov Telescope Array (CTA) [66]. The Pierre Auger Observatory can also contribute to this search in the ultra-high energy regime by looking for photon-induced EAS. Such EASs are expected to be different from the ones induced by CRs as they have a larger electromagnetic component and a rather small hadronic component. A more detailed description of the signature is provided in [67].

Summary of the results of photon searches performed at the Pierre Auger Observatory have been summarised in fig ?? together with the predicted flux from some popular production models. Due to the non-observance of photon-like events at Auger, the collaboration has set some of the stringiest limits for expected photon flux at high energies. This has already helped constrain some top-down scenarios ultimately leading to a much better understanding of the origin of UHECRs. Further, searches will also help constrain the mystery of the cutoff. UHE photon searches are also very useful for a multimessenger approach to astronomy and these contributions are discussed more in section 2.3.

2.2 Ultra High Energy Neutrinos

2.2.1 History

Neutrino(ν) [68] (neut-neutral, ino-small) is an elementary particle belonging to the fermion class with a $1/2$ spin. It was named by Enrico Fermi but first postulated by Pauli in 1930 as an explanation for the conservation of energy, momentum and angular momentum in β decays. It rarely reacts in nature and only scatters via weak interaction. The neutrino was first observed in 1956 by the Cowan-Reines neutrino experiment [69] by detecting the annihilation of neutrons and positrons produced by antineutrinos created in a nuclear reactor. Neutrinos can have three flavours electron neutrinos (ν_e), muon neutrinos (ν_μ), or tau neutrinos (ν_τ) depending on the charged lepton (electron, muon or tau) accompanying them in their production. There are various mysteries involved with understanding this "ghost particle". One of these is the phenomenon of neutrino oscillations which is the intermixing of different neutrino flavors as they propagate through space. This has been observed in various experiments such as the Super-Kamiokande Observatory [70] and the Sudbury Neutrino Observatories [71] and was the recipient of the 2015 Nobel Prize for Physics since it was the first indication that neutrinos have some mass. This has led to various efforts to determine the mass of the three neutrinos (Under Neutrino Properties [62]). Currently, only a hierarchical differentiation can be established [72], the configuration of which is also not completely understood, and further experiments like Karlsruhe Tritium Neutrino experiment [73] are underway to solve this mystery. Also, the very mechanisms with which neutrinos can acquire mass are currently not completely understood [74]. Neutrinos arriving at Earth through astrophysical sources such as the Sun have also played an important role in increasing our understanding of CRs and physics in general. The solar neutrino observations ultimately led to the postulation and discovery of neutrino oscillations. The observations of neutrinos from SN 1987A, a type II supernova in the Large Magellanic Cloud by Kamiokande II [75] before the observation of any other messenger marked the dawn of non-solar neutrino astronomy and displayed the importance of neutrinos for multi-messenger physics. One of the most important experiments in this field has been the IceCube Observatory. Located at the South Pole the IceCube Observatory has revolutionised both neutrino and multi-messenger astronomy. It has led to the first detection of astrophysical neutrinos [76] and provided a measurement of their spectrum for high energies [77]. It has also contributed to the study of the neutrino oscillations [78] and could also help with ν mass hierarchy [79]. Recently, IceCube has further found the first source of steady-state neutrinos in our cosmos which is the NGC1068 [16] and has also led to the groundbreaking measurement of the neutrino spectrum from our Galaxy [22]. These results and their implications are discussed in more detail in section 2.2.4. Its contributions to multi-messenger astronomy are also discussed later in section 2.3. For the highest of energies, the Pierre Auger Observatory remains the only facility capable of detecting neutrinos. Neutrinos can help to understand various astrophysical processes such as the Big Bang where the neutrinos are hypothesized to have decoupled 1 second after leading to cosmic neutrino background (CMB) [80] to the nuclear processes

inside stellar objects. Each such process speculates a unique neutrino spectrum which can be probed with experiments to garner their viability. Figure ?? shows the unified neutrino spectrum with respect to energy. For this thesis, the following sections are constrained to only the neutrinos of the highest energies ($\text{UHE}\nu_s$) above 10^{16} eV. How neutrinos can help decipher the mysteries of UHECRs is also discussed below.

2.2.2 Origin and Propagation

$\text{UHE}\nu_s$ can be broadly classified into three categories based on their origin. These are astrophysical, originating from known/hypothesized astrophysical sources, cosmic/cosmogenic, originating from the interactions of UHECRs with the CMB or the extragalactic Background light(EBL) and exotic, emerging from processes such as the Big Bang, dark matter annihilation etc. The reactions for the mentioned processes are as follows:

Astrophysical Neutrinos

Astrophysical neutrinos are thought to be produced by or around known sources of UHECRs. The most important ingredients that are required to produce $\text{UHE}\nu_s$ are the interactions of high-energy protons and nuclei with matter or radiation fields which result in photo-meson production followed by a charged pion decay. The decay length of pions is much shorter than the distances of the sources to Earth thus they decay and give rise to secondary neutrinos.

$$\begin{aligned} p + \gamma &\longrightarrow \Delta^+(1232) \longrightarrow n + \pi^+ \\ &\longrightarrow \Delta^+(1232) \longrightarrow p + \pi^0 \end{aligned} \quad (2.4a)$$

$$p + \bar{p} \longrightarrow \pi^- + \pi^+ + \pi^0 \quad (2.4b)$$

$$\pi^0 \longrightarrow \gamma + \gamma \quad (2.5a)$$

$$\pi^+ \longrightarrow \mu^+ + \nu_{\mu} \longrightarrow e^+ + \nu_e + \bar{\nu}_{\mu} + \nu_{\mu} \quad (2.5b)$$

$$\pi^- \longrightarrow \mu^- + \bar{\nu}_{\mu} \longrightarrow e^- + \bar{\nu}_e + \nu_{\mu} + \bar{\nu}_{\mu} \quad (2.5c)$$

Other interactions such as Neutron Decay ($n \longrightarrow p + e^- + \nu_e$), electron/positron capture and β decays can also contribute to neutrino production. In most of these scenarios the expected flux ratio per flavor can be either $\nu_e : \nu_{\mu} : \nu_{\tau} = \bar{\nu}_e : \bar{\nu}_{\mu} : \bar{\nu}_{\tau} = (1 : 2 : 0)$ or $(1:0:0)$ with no direct known process for ν_{τ} production at the source. However, since neutrinos can oscillate which is a consequence of the mixing between the flavor $|\nu_{\alpha}\rangle$ and mass eigenstates $|\nu_i\rangle$ of neutrinos, given by the following relation:

$$|\nu_{\alpha}\rangle = \sum_i U_{\alpha i} |\nu_i\rangle \quad (2.6)$$

where $U_{\alpha i}$ is the mixing matrix formulated by Pontecorvo-Maki-Nakagawa-Sakata (PMNS) [81, 82]. In a standard case where three neutrino flavors are considered this matrix is a 3x3 matrix parameterized by the three mixing angles ($\theta_{12}, \theta_{23}, \theta_{13}$) and a single phase called δ_{CP} . Starting from the expected source flavor ratio one can calculate the flavor ratio at Earth by knowing the above four mentioned parameters. One example of such propagation is shown in fig. ?? . Since high energy tau neutrinos are not expected to be present in the atmospheric neutrino background the detection of such neutrinos at Earth could be an indication that the neutrino had an astrophysical origin.

Another important aspect to fully understand the origin and propagation of astrophysical neutrinos is determining the expected energies these neutrinos can acquire. On average the energy fraction that pions can get from the CR nucleons is about 20%. These relativistic pions can then further pass on between $\sim 20\text{-}26\%$ depending on the flavor and type of the neutrino. Approximately, the Energy fraction for the produced neutrinos concerning the gamma and Nucleon is [83]:

$$\langle E_\nu \rangle \simeq \frac{1}{2} \langle E_\gamma \rangle \simeq \frac{1}{20} \langle E_N \rangle \quad (2.7)$$

Depending on the type of source and how far the said source is one can calculate the maximum energy potential for sources. With the measurement of the diffused astrophysical flux [84] by IceCube up to 10^{16}eV , these calculations can be directly constrained by measurement [85]. Since extragalactic sources can produce UHECRs up to 10^{20}eV which is corroborated by measurements of the Pierre Auger Observatory one can calculate an upper limit to the diffuse flux for neutrinos. Some of these calculations can be found in [86] for Starburst galaxies, [87] for AGNs and [88] for Magnetars. The non-detection of $\text{UHE}\nu_s$ at Auger can thus also act as an important tool to constrain the production mechanisms hypothesized for these sources. The potential of this is discussed later in section 2.2.4.

Cosmogenic Neutrinos

Cosmogenic neutrinos are produced either as a consequence of the GZK mechanism discussed in section 2.1.3 or due to the interactions of UHECRs with EBL. They were first suggested by Berensinsky and Zatsepin in 1969 [89]. The processes involved are similar to those for astrophysical neutrinos albeit the proton/nuclei interact with the CMB/EBL photon instead of the photons from the radiation fields. The two main processes are the same as that for the GZK mechanism i.e. photo-pion production 2.1 and photo-disintegration 2.2. CMB mainly affects the protons [90] during their propagation which form a large fraction of the UHECRs traversing the universe while the EBL plays an important role in the case of other nuclei [91]. Since the processes are the same the flavor flux expectations at Earth remain the same. However, the expected energies that the cosmogenic neutrinos can acquire differ drastically as compared to astrophysical neutrinos. The energy threshold for neutrinos produced due to interactions with CMB in the case of photo-pion production is of the order of 10^{18}eV while for photo-disintegration it is of the order of 10^{18}eV [91]. In the case of interactions

with EBL, this lowers to about 10^{15} eV and 10^{14} eV for the two types of interactions. The exact properties of the neutrinos produced are directly dependent on the parent UHECRs that produce them. The properties of UHECRs such as the total flux, composition, maximum energies, production spectrum at the sources and their cosmological evolution (adiabatic losses) are all crucial factors that affect the secondary cosmogenic neutrinos produced by these UHECRs. A collection of some examples of the expected cosmological fluxes for different scenarios can be found in [92] [93]. An example is also shown in fig ???. The two distinct humps are due to the two associated production processes with the lower one being the photo-disintegration.

Measurements of cosmic ray observatories such as the Pierre Auger Observatory can also be used to calculate an expected neutrino spectrum based on assumptions on the composition and the cosmological evolution of the sources. Neutrinos thus can act as a very important tool in constraining the composition of the incoming UHECRs and furthering their actual sources. They can also help to solve the question of the cutoff observed in the UHECR spectrum whether this is due to the GZK mechanism (proton-dominated composition) or sources reaching their maximum potential as theorized by Hillas (mixed composition). The current results regarding this important study are discussed in section 2.2.4

Exotic Neutrinos

Neutrinos can also be produced as a result of self-annihilation or decay of dark matter particles. In dark matter annihilation scenarios, two dark matter particles come together and annihilate, leading to the production of standard model particles as a result. The specific flux of the neutrino depends on the properties of the dark matter particle. One such candidate for such a process could be a Weakly Interacting Massive Particle (WIMP), which is its own antiparticle (a Majorana fermion). In regions with a high concentration of dark matter, such as the centers of galaxies or galaxy clusters, WIMPs can come together and annihilate into standard model particles [94]. One of the annihilation channels of interest for producing very high-energy neutrinos is the annihilation into pairs of intermediate bosons, such as $W^+ W^-$ (W-boson pair), or $Z^0 - Z^0$ (Z-boson pair). These intermediate bosons can subsequently decay into quarks, leptons, and other particles, including neutrinos. The final state neutrinos can be very high-energy, potentially reaching energies in the peta-electronvolt (PeV) range and beyond. For dark matter decay, a stable dark matter particle is supposed to spontaneously transform to other standard model particles including neutrinos [95].

(2203.17223.pdf)(CNB probably do not want to discuss this)

2.2.3 Neutrino Interactions and Detection

(<https://indico.mitp.uni-mainz.de/event/277/attachments/2666/3013/Scholberg1.pdf>)

The low interaction cross-section (σ_ν) [96] of neutrinos which allows them to travel for large distances also makes them almost impossible to detect. They can pass through vast amounts of material without leaving a significant trace. While at low energies processes

such as Inverse Beta Decay are used to detect the neutrinos, at high energies neutrinos can interact via Charged Current (CC) and Neutral Current (NC) Interactions. In CC interaction, a neutrino interacts with a target nucleus with an exchange of W boson, transforming into a charged lepton corresponding to the flavor of the incoming neutrino and a hadron. The NC interaction is flavor blind and occurs with an exchange of the Z^0 boson and a nuclear recoil. Both reactions are shown in the equations below:

$$\nu_l(\bar{\nu}_l) + N \xrightarrow{\text{CC}} l^-(l^+) + X \quad (2.8a)$$

$$\nu_l(\bar{\nu}_l) + N \xrightarrow{\text{NC}} \nu_l(\bar{\nu}_l) + X \quad (2.8b)$$

The products from the CC and NC interaction i.e. a lepton and a hadron can be detected in multiple ways. Antineutrinos can also interact with atomic electrons leading to a W^- boson production called the Glashow resonance [97]. The threshold antineutrino energy for such a reaction to occur is ~ 6.3 PeV. This process dominates the CC and NC interaction albeit only in a small energy range. Proposed in 1959, it was first observed at the IceCube Observatory [98]. Both CC and NC when interacting with the Nucleon undergo Neutrino-Nucleon Deep Inelastic scattering (DIS) where the interacting neutrino scatters off individual quarks inside nucleons (protons or neutrons), leading to the fragmentation of the nucleon and the creation of hadrons (Particles made of quarks). At low center-of-mass energies ($\sim \text{TeV}$) accelerators can provide most of the information about the neutrino interaction with matter and the corresponding cross-section but at energies this estimation can either only be calculated via the detection of astrophysical and cosmogenic neutrinos or via a robust theoretical estimation based on quantum chromodynamics (QCD). The description of QCD at such high energies is still not completely understood, Moreover, physics beyond the Standard Model can also be introduced for these energies which can further affect the neutrino cross-section estimation [99]. For the purpose of this thesis, the neutrino cross-sections calculated in [100] are used. [100] provides an updated $\nu - N$ cross-section calculations with corresponding uncertainties, taking into account the full HERA [101] data release and combining it with the DGLAP [102–104] formalism of QCD. Based on the expected flux the cross-section and the energy of neutrinos it is easy to calculate minimum detector sizes for high-energy neutrinos. For example, for a neutrino of energy $E_\nu \sim 1 \text{ PeV} = 10^{15} \text{ eV}$, the expected flux is $\frac{d^2 N_\nu}{dt dA} \sim \frac{1}{\text{cm}^2 \times 10^5 \text{ yr}}$, the cross-section is $\sigma_{\nu N} \sim 10^{-8}$, $\sigma_{pp} \sim 10^{-33}$ and the targets can be estimated as $N_N \sim N_A \times V / \text{cm}^3$ where N_A is the Avogadro's number then the rate of expected events is given by:

$$N_\nu \sim N_N \times \sigma_{\nu N} \times \frac{d^2 N_\nu}{dt dA} \sim \frac{1}{\text{yr}} \times \frac{V}{1 \text{ km}^3} \quad (2.9)$$

Therefore, to detect a neutrino at this energy range a detector with a minimum size of 1 km^3 is required. The type of such large volume detectors for $\text{UHE}\nu_s$ depends on the particular

techniques used to detect the products of neutrino interaction with nucleon.

The charged lepton can produce detectable signals via ionization, Cherenkov radiation or scintillation. Moreover, the lepton and hadrons can also trigger EASs which can also be detected. Both the lepton and the hadron can lead to a cascade. Depending on the flavor of the neutrino the interaction also leads to unique signals. The electron produced in the CC interaction of ν_e produces electromagnetic cascades in the propagation medium while a muon rarely produces a cascade like signature only undergoing radiation losses. In contrast, a tau lepton produced from ν_τ can propagate without interaction for a certain distance and then lead to a cascade. For NC reactions the leptonic cascade is missing and only a hadronic cascade can be observed. Low-energy neutrinos or neutrinos produced in the atmosphere can also lead to similar cascades and act as background for high-energy neutrino searches. Depending on the location and techniques employed such background is dealt with in different ways. Some examples of different detectors based on the medium and the methodology employed for detection are as follows:

Ice and Water Cherenkov Detectors: IceCube Neutrino Observatory [105] and its predecessor AMANDA [106] are examples of in ice Cherenkov detectors. IceCube is located at the South Pole and uses a cubic-kilometer array of Antarctic ice to detect high-energy neutrinos. It consists of 80 strings carrying 60 photomultiplier detectors situated between 1500m and 2500 m below the surface. Neutrinos interact with the optically clear ice nuclei, producing secondary particles that emit Cherenkov radiation. The detector's photomultiplier tubes capture the Cherenkov light, allowing reconstruction of the neutrino direction and energy. Muon tracks resulting from CC interactions can also be observed. Being underground partly shields IceCube from the atmospheric neutrino background, and it can also use the Earth as a shield to look for PeV upward-going neutrinos. The Observatory also consists of a surface array (IceTop) of ice Cherenkov tanks which further help in atmospheric background rejection and CR studies.

Water based Cherenkov detectors have been used for neutrino detection since the first detection of neutrinos. Kamiokande II [107] used a large underground water tank surrounded by PMTs to observe the first astrophysical neutrinos from SN 1987A [75]. Since the required detector volume for detection of a sufficient rate of neutrinos is very large, large stable natural water reservoirs are used to build such detectors. Some examples include the ANTARES [108] and KM3Net [109] located in the Mediterranean sea off the coast of France and the upcoming BAIKAL-GVD [110] and P-ONE [111] located in Lake Baikal, Russia and the Pacific Ocean off the coast of British Columbia, Canada respectively. The actual detector and the principle remain the same as IceCube with the only change being the medium and upgrades in detector technology depending on the advances in the field.

- **Radio Detectors:** These detectors are based on the detection of the Askaryan effect [112, 113] initiated by the neutrinos. The Askaryan effect is a phenomenon in which high-energy charged particles moving through a dense dielectric medium, produce coherent

electromagnetic radiation in the radio frequency range. When the high-energy particles interact with the atoms and molecules in the dielectric medium, they generate a shower of secondary charged particles. As these secondary particles move through the medium they undergo a charge separation leading to the emission of coherent Cherenkov radiation in the radio frequency range. The effect typically produces radiation in the radio frequency range, from a few hundred megahertz (MHz) to several gigahertz (GHz). Experiments like ANITA [114] have tried to detect the radio emission produced when neutrinos interact with the Antarctic ice [115]. RNO-G [116], an in ice radio antenna array, is also under construction at Summit Station in Greenland to search for neutrinos above PeV energies. Detectors like AERA and GRAND could also use such a technique to detect EAS produced by neutrinos. The planned upgrade of IceCube, IceCube-Gen-2 [117] also plans to employ a large in ice radio array to increase its sensitivity to both astrophysical and cosmogenic neutrinos.

- **Acoustic and Radar Echo Detectors:** The cascade of secondary particles produced in a neutrino interaction in a medium can also generate an acoustic shockwave, also known as a "thermoacoustic pulse," due to rapid heating and expansion of the medium. The resulting acoustic signal travels through the medium as a pressure wave and can be detected by sensitive acoustic sensors. Typically, large volumes of water or ice are used as the detection medium. The acoustic signal propagates through the medium and can be detected by underwater microphones (hydrophones) or other acoustic detectors. This technique has not yet yielded a neutrino observation. It has been used at ANTARES as AMADEUS [118] and at IceCube as SPATS [119] to test the acoustic properties. ANDIAMO [120] is a proposed acoustic neutrino detector that could use this technique in the future.

Radar Echo Telescope [121] is a detector that aims to detect neutrinos using the radar echo method. The method is based on the reflection of a transmitted radar signal by the in ice neutrino cascade which acts as a short-lived mirror. The reflected signal is then detected at a receiving antenna. This technique is currently being tested in Greenland for Cosmic ray showers and might be employed to detect neutrinos in the future.

- **Air Shower Detectors:** Even though, the typical interaction lengths of $\text{UHE}\nu_s$ are way larger than the atmospheric depth the neutrinos can still induce an EAS. Such EASs develop deep into the atmosphere in comparison to cosmic rays offering a distinguishing aspect for detection at cosmic ray observatories like the Pierre Auger Observatory. Pierre Auger Observatory tries to use the said property to observe EeV neutrinos. EASs and the expected signature at the Pierre Auger Observatory for both cosmic rays and neutrinos are discussed in the next Chapter 3.

2.2.4 Latest results

Astrophysical Neutrinos

spectrum After the measurements of astrophysical neutrinos at the IceCube Neutrino Observatory, the first plot and estimation of flux has been possible for high-energy neutrinos. The flux spectrum as measured by IceCube is shown in fig ???. The flux was first published in 2013 [122] and has since been refined with various analyses [84]. The plot shows the results of the summary of the currently published analysis. The diffuse flux spectrum agrees across the various analyses within the overlapping energy regions. However, there is a slight tension between the estimate of the spectral index which is obtained after fitting the flux spectrum. The measurements are also not enough to decide on the nature of the flux across the whole energy range and more measurements in the future would help understand the neutrino spectrum in more detail.

Sources Since neutrinos arrive at Earth pointing directly back to their source, plotting the candidate astrophysical neutrino events measured by the neutrino telescopes over a sky map can localize their sources of origin. Such studies have been performed by various neutrino telescopes such as ANTARES [123], AMANDA [124], BAIKAL-GVD [125] and IceCube [16]. Only IceCube has found the most significant excess of 81 events in the TeV arriving from the region within 0.18 degrees of active galaxy NGC1068(M77). The fig ??? taken from [16] shows the hottest spot along with the excess. This observation has a significance of σ in comparison with ?. Hosting an active AGN surrounded by a dust torus makes it one of the ideal candidates for neutrino production [126, 127]. The same analysis has also pointed out other potential neutrino source candidates PKS 1424+240 and TXS 0506+056. The latter of these is also important in the context of multi-messenger physics and is discussed later.

In 2023 IceCube also published the first observation of diffuse emission of high-energy neutrinos from the galactic plane of our own galaxy, the Milky Way [22]. The result is at the 4.5σ level of significance when compared to a background-only hypothesis. However, the signal could also be due to a population of unresolved point sources near the galactic plane. This observation has opened a new way to observe our Milky Way galaxy and offers an evidence based proof confirming our understanding of both cosmic ray and neutrino physics. It also opens a new avenue for the application of multi-messenger astronomy. The fig ?? shows the plane of the Milky Way galaxy as seen by different messengers.

Cosmogenic Neutrinos

Limits Both the Pierre Auger Observatory and the IceCube neutrino Observatory have also performed searches to look for $\text{UHE}\nu_s$ which have a cosmogenic origin. These searches have led to some of the stringiest limits for such fluxes. These limits are shown in fig ???. The results from the Pierre Auger Observatory dominate for energies above 10^{18}eV and for lower energies, IceCube provides the best limits. The lack of observations can help

constrain various models for high-energy neutrino production. These results can also help better our understanding of cosmic ray physics and in particular their composition. The lack of observation of the expected neutrino flux predicted by a pure proton composition scenario for CRs is an important result in favor of mixed composition scenarios. This result further points towards the spectrum cutoff being more likely due to a maximum rigidity limit for the sources rather than a GZK limitation. The detection of cosmogenic neutrinos can help complete the picture of the neutrino and cosmic ray sky.

2.3 Multimessenger Astronomy

Combining the various messengers via which we can see the Universe can help better understand the mechanisms behind their production and propagation. By combining the observations of various dedicated experiments for gravitational waves(LIGO/VIRGO), Gamma rays(FERMI-LAT, CTA), neutrinos(IceCube) and cosmic rays(TA, Pierre Auger Observatory) a wholistic overview of an astrophysical process can be gathered. The detection from one messenger/experiment and a non-detection from another can also be informative since it helps refine our understanding or might even reveal a new phenomenon [128, 129]. One of the most important aspects of this field is a fast communication network via which all the different experiments can share their observations as fast as possible. Supernova Early Warning System (SNEWS) [130], established in 1999 and The Astrophysical Multimessenger Observatory Network (AMON) [131], created in 2013 are some examples of the networks used in multi-messenger astronomy. Some of the key observations of this field and the corresponding publications are summarised in table 2.1. As mentioned in the Introduction, the Pierre Auger Observatory continues to contribute to these searches [132]. One of the best examples of this collaboration is [133] where a spatial correlation search for neutrinos and CRs was performed as a joint effort between ANTARES, IceCube Observatory, Pierre Auger Observatory and the Telescope Array. The GW 170817 [20] multi-messenger analysis using more than 70 observatories cemented the benefits and the potential of multimessenger astronomy.

The production and detection mechanisms discussed offer us the basic ingredients needed to set up an experiment for the detection of A' . One of the simpler layouts for such an experiment is an electron beam dump experiment. NA64 falls in this category, the setup of which is discussed in the next chapter.

Multimessenger picture					
Astrophysical Event	Electromagnetic	Cosmic rays	Gravitational Waves	Neutrinos	Example
Solar flare	yes	yes	-	-	-
Supernova	yes	-	predicted	yes	SN1987a
Neutron star merger	yes	-	yes	predicted	GW170817
Blazar	yes	possible	-	yes	TXS 0506+056
Active galactic nucleus	yes	possible	-	yes	NGC1068
Tidal disruption event	yes	possible	possible	yes	AT2019dsg AT2019fdr

Table 2.1: Table to test captions and labels.

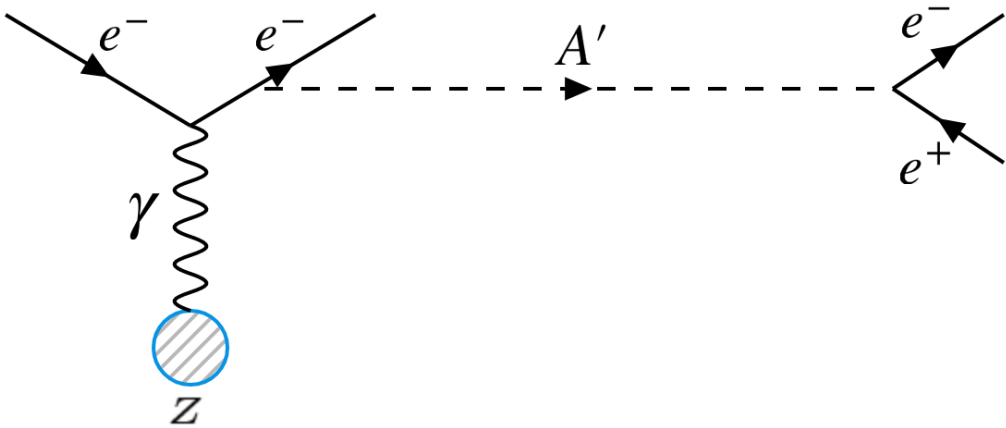


Figure 2.1: Visible mode

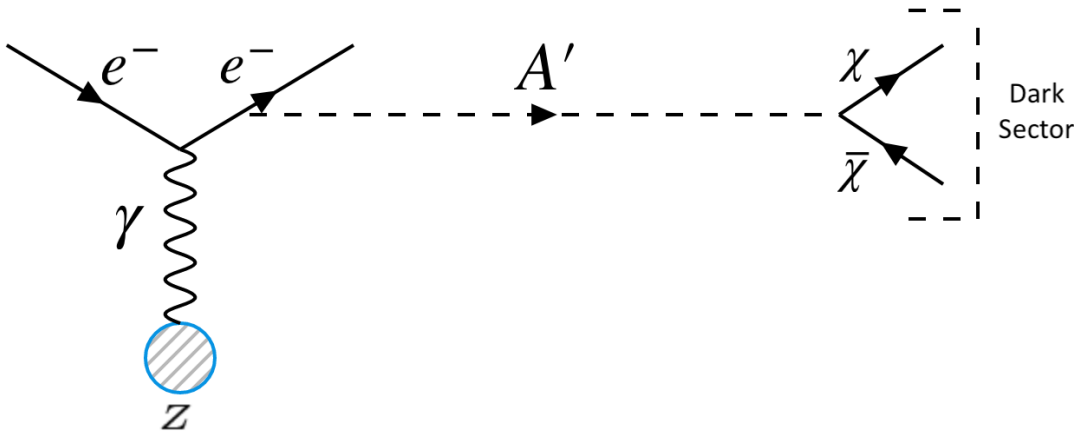


Figure 2.2: Invisible mode

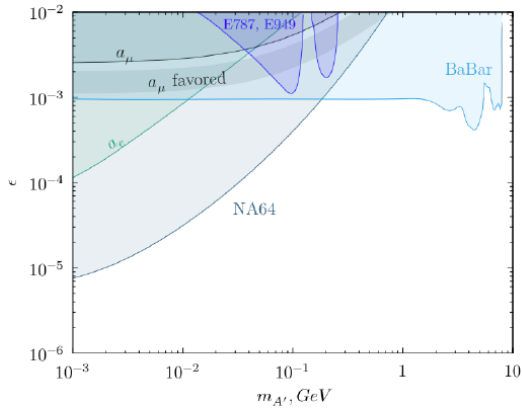


Figure 2.3: Current limits for invisible mode for 90% C.L. exclusion region in the $(m_{A'}, \epsilon)$ plane [1].

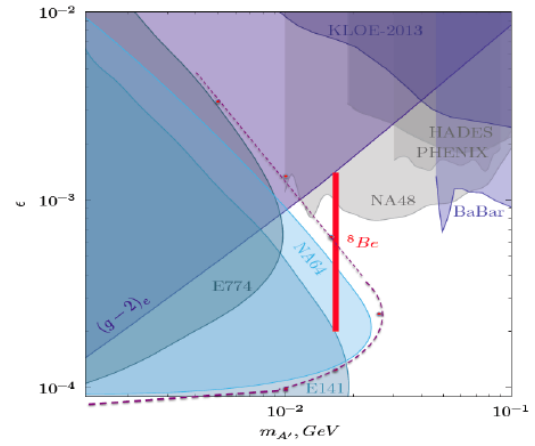


Figure 2.4: Current limits for invisible mode for 90% C.L. exclusion region in the $(m_{A'}, \epsilon)$ plane. The blue plane is with 2017 data and the dotted line is with 2017+2018 data for NA64. The red line is the region that might explain the X17 boson [1].

Extensive Air Showers

As mentioned in the previous chapter An Extensive Air Shower (EAS) is a cascade of high-energy particles that is produced when an ultra-high-energy cosmic ray, typically a proton or a nucleus, collides with a particle in Earth's atmosphere. This cascade can span over hundred to thousands of meters based on the energy of the initial particle and the incoming angle. EASs offer the best way to look for UHECRs since the low flux of these particles make direct detection using detectors mounted on balloons and spacecrafts not feasible. The EAS can be detected at the ground via an array of detectors. To infer the properties of the CR from the EAS it creates, one needs to model and understand how an air shower develops in the atmosphere. This chapter describes the process of the initiation and the development of the shower induced by CRs and neutrinos. It also aims to describe the important characteristics of EASs which help in extracting the relevant information and the last section is devoted to the detection of the EASs using different detector systems.

3.1 Development

As the CR particle which is predominantly a proton collides with the nuclei of the atmosphere (N_2 , O_2 etc.) it produces pions and a few kaons. The neutral pions produced immediately decay to pairs of photons which in turn produce electrons via the process of pair-production. These electrons can then further produce photons via bremsstrahlung initiating a chain reaction which alternates between these two processes and forms the *electromagnetic component* of the shower. The charged pions can survive for a while but eventually decay to muon and a corresponding anti neutrino. These muons can either survive till the shower reaches the ground and form the *muonic component* or can also decay to electron thus contributing to the electromagnetic part. The neutrinos due to their low interaction cross-section mostly survive till they reach the ground and even further. Though not causing any problem for an EAS detector such neutrinos are the biggest background for a neutrino telescope. Kaons and charged pions due to their long lifetimes can also interact with the atmospheric nuclei producing additional pions which form the *hadronic component* of the

shower. The hadronic component can further contribute to both the electromagnetic and muonic component as more the shower propagates lesser the overall hadronic component becomes. A schematic of all the reactions with the different components is presented in fig ??.

To understand the cascade of particles a detailed modelling of each component is required. These models help extract the basic properties of the cascade. A simplified model describing the electromagnetic component called the Heitler's toy model, its hadronic extension and a generalised cascade equation are all discussed below. The specific development of a neutrino induced EAS is also discussed.

3.1.1 Heitler's Toy Model

Proposed by Heitler in 1954 [134], Heitler's Toy Model is a simplified perfect binary tree to understand and model an EAS development. The model characterises an EAS as a perfect binary tree. In such a scenario all particles produced in a shower equally share the primary energy available at the time of their creation. At each step, which has a fixed size related to radiation length of the medium λ , the number of particles are supposed to be doubled, with each having the same energy. The energy losses which may occur due to collisions are completely ignored. The shower development or splitting process is supposed to continue till a critical point where the energy required to create more particles becomes the same as energy lost by particles in the medium. At the critical point, the shower has the maximum number of particles given by, $N_{max} = E_0/E_c$, which is the ratio of the original energy (E_0) to the critical energy (E_c). After this point the shower keeps getting absorbed in the atmosphere. The radiation length at this point is called the shower maximum denoted by X_{max} . This can be calculated to be $X_{max} = X_0 + \lambda_r \ln(E_0/E_c)$ where X_0 is the first interaction point in the atmosphere. A visualisation of the shower development according to the Heitler's model is shown in fig ??.

Such a simplified model works quite well for estimating the properties of the electromagnetic cascades although the N_{max} estimations do not match perfectly. The reason for this is the difference in the energy loss values for electrons and photons. For hadronic cascades an extension to the model was made. Other important properties of the shower such as lateral and longitudinal spread, also require taking into account the emittance direction and losses due to collision which are not taken into account for a simplified model. These are discussed in sec 3.2. Even with its shortcomings the Heitler model gives a very good estimation for electromagnetic cascades and helps clearly categorise an air shower into three phases, the growth phase, the critical point phase and the tail phase.

3.1.2 Hadronic Extension

The Heitler model was extended by Matthews [135] to characterise the hadronic cascades in an EAS. In his approximation when a hadron with Energy E interacts with a nucleon the total particles produced have a two-third charged component (π^\pm) and a one-third neutral

component (π^0) with the initial energy equally divided based on the number fraction. The neutral component decays quickly and contributes its share of energy to the electromagnetic component. The charged hadrons, provided they have not reached their critical energy in air (~ 20 GeV), interact again repeating the initial process. Muons are only produced when the charged hadrons acquire an energy below the critical energy. The energy transfer for each component after n generations is given as $E_{had} = \left(\frac{2}{3}\right)^n E_0$ and $E_{em} = \left[1 - \left(\frac{2}{3}\right)^n\right] E_0$. Deeply penetrating air showers i.e a primary with high energy and a low enough cross-section in air, results in a lower number of muons produced, and observed at ground. This fact is important as based on the ratio of muons to electrons observed at ground, the type of the primary can be estimated. The number of muons (N_μ) can be estimated in this model directly from charged hadrons when their energy reaches below the critical energy. For n generations $N_\mu = n_{ch}^n$ where n_{ch} are the number of charged hadrons and n can be written as $n = \frac{\ln(E_0/E_c)}{\ln(n_{tot})}$. Generalising by eliminating generations:

$$N_\mu = \left(\frac{E_0}{E_c}\right)^\alpha, \quad \alpha = \frac{\ln(n_{ch})}{\ln(n_{tot})} \quad (3.1)$$

All the parameters in this model need to be estimated using detailed simulations [136]. α has been estimated to be in the range 0.82...0.9. Other factors such as production of particles which do not decay such as baryon-anti-baryon pairs [137] can also affect the calculated values in this model. Other than the shower maximum and number of muons, the change of the depth of the shower maximum per decade in energy also called the elongation rate is given by $D_{10} = \frac{\langle X_{max} \rangle}{d \log_{10} E_0} = 2.3 \lambda_r$. The elongation rate of electromagnetic showers in air is about $\approx 85 g/cm^2$. The elongation rate theorem [138] states that the upper limit to the elongation rate for hadronic showers is also D_{10}^{em} in the presence of Feynman scaling.

The first interaction with the nucleon was presented in a simplified way by Matthews as the superposition model. In this model a nucleus with mass A is assumed to be a superposition of A independent nucleons, each with energy $E_h = E_0/A$. With such an assumption one can reach the following conclusions:

$N_{em,max}^A(E_0) = A N_{em,max}^h(E_h/E_c) \approx N_{em,max}(E_0)$ i.e. the fraction of energy transferred to the EM component at shower maximum, has only an indirect dependence on mass via the dependence on primary energy.

$X_{max}^A(E_0) = X_{max}(E_0/A)$. This shows how the shower maximum has an inverse dependence on the mass of the primary i.e a shower initiated by heavier nuclei will develop higher in the atmosphere compared to one initiated by lighter nuclei.

$N_\mu^A(E_0) = A \left(\frac{E_0/A}{E_c}\right)^\alpha = A^{1-\alpha} \left(\frac{E_0}{E_c}\right)^\alpha$. This shows that heavier primaries will produce a larger number of muons compared to lighter primaries. For e.g. Iron showers contain 40% more muons than proton showers [139].

$D_{10} = D_{10}^{had} \left(1 - \frac{d\langle \ln A \rangle}{d \log E} \right)$ Since Feynman scaling is known to be violated for higher energies, the hadronic elongation rate is always less than the electromagnetic rate. Thus, an increase in elongation rate towards 85 g/cm^2 is a direct indication of change of the mass composition.

Simulations have shown that the superposition model gives a more realistic description of many features of the shower [140]. However, it is still not a perfect description especially for heavier nuclei. Studies with photographic emulsion techniques have tried to create a better picture of the fragmentation of heavier nuclei [141]. This field is continuously evolving with better models and theoretical predictions being worked on based on our continually increasing database of observations.

Although these models help understand the principle, a full Monte Carlo simulation and a generalised analytical solution of the cascade equations is needed to fully recreate the EAS. Even after such efforts a few discrepancies such as the muon puzzle which is the mismatch in the number of muons predicted by the simulations in comparison to the measurements [142].

3.1.3 LPM effect

Another process that can directly impact the development of high energy electromagnetic showers since it is the reduction of the bremsstrahlung and the pair-production cross-section is the Landau–Pomeranchuk–Migdal effect [143, 144]. All the above models work under the assumption that the energy range is low enough for the LPM effect to not be applicable. If the medium is dense enough or at high energies the LPM effect also becomes important to fully estimate the development of an air shower. The implications of the LPM effect for air showers implemented in simulations can be found in [145].

3.1.4 Neutrino induced EAS

The development of a neutrino induced shower in comparison to a CR shower is important in the context of this study. Understanding the differences helps to identify the unique signature at a CR observatory like the Pierre Auger. The differences in the shower development can also help increase the sensitivity of a neutrino observatory like the IceCube. Unlike a cosmic ray particle a neutrino can interact at any depth. This is due to the low neutrino cross-section at $10^{18} \approx 10^{-33} \text{ cm}^2$ in comparison, for e.g. the proton-nucleon cross-section which is $\approx 10^{-27} \text{ cm}^2$. Thus, neutrino-induced showers require significantly higher neutrino energies to produce interactions with observable effects. The main channel via which an ultra-high energy neutrino can interact is either a CC or NC interaction as mentioned in the last chapter. Neutrino-induced showers involve fewer particles in the initial interaction and often have a lower multiplicity of secondary particles compared to CR-induced showers. The development of the shower and the unique signature depend on the flavor of the neutrino as shown in fig ??.

An electron neutrino, ν_e , interacting via CC interaction produces an initial hadronic cascade which has fewer particles in comparison to a hadron-initiated shower from the CRs. The high energy electron/positron produced in the same initial interaction also produces an electromagnetic shower. At high energies the two showers are overlapped and the fraction of energy carried by the electron/positron governs the ratio of the electromagnetic to hadronic component for the shower.

A muon neutrino, ν_μ , also produces an initial hadron cascade but in contrast to the electron neutrino interaction the resulting muon has a very low probability to decay and mostly passes through the detector undetected. The energy carried by the muon which is usually a large fraction is lost and only the hadronic cascade can be detected.

Tau neutrinos, ν_τ , have a unique and particularly interesting signature even among neutrino showers. The initial interaction remains the same with the production of a hadronic cascade, but the resulting tau lepton has a decay length $\approx 10\text{km}$. This means that depending on the depth of the atmosphere the tau encounters on its way to the ground, it can either decay and produce an electromagnetic cascade much later than the initial hadronic cascade or not decay at all. The asynchronous cascade signature is also known as "double-bang" effect and can occur both in air or a specific medium. Tau neutrinos can also be a source of upward-going air showers which can also be detected at an EAS detector. In this case the tau neutrinos can interact in the Earth's crust or in some natural obstruction like mountains around the detector leading to production of a hadronic cascade which gets absorbed and a tau lepton which can escape and produce an electromagnetic cascade in air that can be detected. The process is unique to tau neutrinos for an EAS detector since for an ν_e both the hadronic cascade and the electron is absorbed by the obstacle whereas for the muon neutrino the resulting muon is almost impossible to detect.

All three neutrino flavors can also undergo NC interactions. These also result in an initial hadronic cascade and a neutrino which usually does not interact and escapes being detected especially for an EAS detector. Thus, the signature is indistinguishable in comparison to a muon neutrino CC interaction. The probability of NC interaction is also lower than a CC interaction which also affects the overall number of EASs induced due to this channel.

3.2 Characteristics

Apart from the shower maximum and the number of muons at ground other observables are also required to fully characterise the shower and estimate the important quantities such as the mass, energy and the arrival direction of the incoming primary CR or UHE ν . Fig ?? gives an overall picture of the evolution of an EAS in air. The amount of atmosphere penetrated is measured in units of slant depth X , with a unit of g/cm^2 . The first interaction depth, X_0 , is the slant depth until the first interaction of the primary particle with the nucleon. The shower begins from this point on and the vector along which the shower develops from the first interaction point is called the *shower axis*. The development continues till the shower reaches a maximum which was defined earlier and is denoted by X_{max} . After this point the

shower depopulates which is caused by particle energy loss due to absorption or decay. The *longitudinal development profile* plotted in fig ?? gives a relation between the number of shower particle in dependence to the atmospheric depth. This relation is also called the Gaisser-Hillas function [146] parametrised as follows.

$$N(X) = N_{max} \left(\frac{X - X_0}{X_{max} - X_0} \right)^{\frac{X_{max} - X_0}{\lambda}} \exp \left(\frac{X_{max} - X_0}{\lambda} \right) \quad (3.2)$$

X_0 and λ can be estimated by fitting the profile based on the above function and depend on the composition and energy of the primary. N_{max} is the number of particles observed at X_{max} . The integral of the longitudinal development profile gives an estimate of the total calorimetric energy deposited by the shower. The point where the shower axis vector intersects the ground is called the *shower core*. Shower axis is thus defined by the zenith θ , azimuth ϕ and the shower core position. If one looks at the shower head on the large thin disc like appearance consisting of highly energetic particles is called the *shower front*. The shape is due to the path length differences between the shower particles travelling away from the shower axis to the one travelling in the direction of the shower axis. The disc is thus thinner near the shower core and widens away from it. As the shower front intersects the ground, the density and the timing of the particles detected at the detector form what is called the *shower footprint*. It is the primary observable used by a ground level EAS detector to measure and characterise the shower. The arrival time of the particles in the footprint can help determine the shower geometry whereas the density can be used to reconstruct the energy of the primary. The density is estimated as a function of the radial distance from the shower core on the ground, by the *lateral distribution function* (LDF). The modern LDF function is an extension on the parameterisation given by Greisen [147] and by Kamata and Nishimura [148] and is given as:

$$\rho_e(r) = \frac{N_e}{2\pi R_M^2} C(s) \left(\frac{r}{R_M} \right)^{(s-2)} \left(\frac{r}{R_M} + 1 \right)^{(s-4.5)} \quad (3.3)$$

Define other variables

with $s = \frac{3}{1 + 2X_{max}/X}$ and the Moliere radius $R_M = 0.0265X_0(Z + 1.2)$.

Another important characteristic of an EAS are its universality features first pointed out by Hillas for electromagnetic showers [149]. In this formulation around the shower maximum the average development of an air shower is universal. An individual shower can be defined as a function of shower age, s , defined earlier give by:

$$s = \frac{3}{1 + 2X_{max}/X} \quad (3.4)$$

This feature is a result of the nature of the development of the cascade process which hides the initial primary dependent fluctuations [150]. Simulations have used such a universal feature to fit shower profiles reasonably well independent of the primary mass and energy [151]. Air shower universality only holds for air showers induced by gamma rays, electrons, or positrons and breaks down for a hadronic cascade. It can still be used if each individual component

of the shower can be disentangled. Although, not applicable for this study, Universality is an important characteristic of the shower and has been used to estimate the proton-air cross-section [152] and other CR studies [153].

3.3 Detection

At high energies due to the low flux EAS offer the best way to detect CRs. Low cost ground based detectors can be spread over large areas offering a cost-effective way to study UHECRs. The shower can be seen through different emissions such as the Cherenkov, fluorescence and radio. The particles arriving at ground can also be directly detected. The different emissions which can be detected in context of EAS are described in this section along with an expected EAS signatures of a neutrino induced EAS which relates to the analysis presented in this thesis.

3.3.1 Fluorescence Detection

The phenomenon of fluorescence emitted by air showers above 10^{17} eV, known as "atmospheric fluorescence", involves the production of faint optical and ultraviolet (UV) light by the interaction of high-energy particles from extensive air showers with the nitrogen molecules in Earth's atmosphere. The energy levels of the nitrogen molecules determine the wavelengths of light that are emitted. The UV light emitted during the de-excitation process is typically in the near-ultraviolet range. The number of photons emitted directly correlates to the energy deposited by the shower particles. At altitudes between 5 and 10 km, the yield has a height dependent rate of 4-5 photons per meter per charged particle. The photons can be seen at large distances up to 35 km. The measurement of the light intensity through fluorescence telescopes with the help of the geometry of the shower axis offers a way to reconstruct the longitudinal profile of the shower and a subsequent energy estimation of the primary. Fluorescence telescopes are limited in their operational duty cycle which is about 10-15 % since they can only be operated on clear moonless nights. A proper reconstruction of shower variables via the emitted fluorescence light also requires constant monitoring of the atmosphere to account for light yield corrections. The pioneering fluorescence light detection of EAS include experiments at Volcano Ranch [154] and Fly Eye experiment [155, 156]. Currently, this technique is also used at the Pierre Auger Observatory and the Telescope Array (TA).

3.3.2 Cherenkov Detection

Charged particles moving through the atmosphere can also produce Cherenkov light [157]. The EAS can be either detected via Imaging Cherenkov telescopes (IACTs) which can detect showers between 20 GeV -100 TeV or non-imaging Cherenkov detectors can be set up akin to a ground based particle detector array. Both are techniques are used for both gamma-ray

astronomy and CR studies. Since the Cherenkov cone is collimated around the shower axis the detectors need to be located with small spacing between them. For e.g. for a particle at 10 km height, the Cherenkov cone has a radius of 120 m. This property and the similar operational limitations akin to the fluorescence detection for the IACTs, makes this technique impractical to detect UHECRs. The currently operational experiments using the non-imaging Cherenkov technique for EAS detection include Yakutsk [158] and Tunka [159] etc. IACTs are very popular for gamma-ray astronomy and multimessenger detections with H.E.S.S. [64], MAGIC [160] and CTA [66] currently operational.

3.3.3 Radio Detection

An EAS traversing through the atmosphere can also produce radio signals. The radio emission can be due to the geomagnetic field [161] or the Askaryan effect [112] described before. For air showers the emission due to the geomagnetic effect is supposed to dominate with the Askaryan effect only contributing in the order of 10-15% [162]. This affect arises due to the deflection of electrons and positrons produced in the shower leading to the formation of an electric dipole moving through the atmosphere at the speed of light. This results in a forward focussed radio signal with a lateral distribution similar to Cherenkov emission. The radio signal depends on the orientation of geomagnetic field and the atmospheric conditions at the detector. Around 100 m from the shower core the expected frequencies are in the MHz range [163] while near the shower core they are in the GHz range. For such frequencies and primary energies $>10^{17}$ eV the emissions from the two different mechanisms is superimposed. The measured electric field scales with the primary energy of the shower. Typically, to detect radio emission of an EAS several radio antennas are deployed over a wide surface area. These antennas are triggered by particle detector arrays. Self triggering is also being developed which will make the radio antennas a standalone functional unit for EAS detection. Some e.g. of currently operational radio antenna arrays for EAS detection include LOFAR [164] and AERA [165]. The Pierre Auger Observatory is also adding a radio antenna on each unit of their particle detector array which is supposed to become operational by 2024. Other planned experiments include GRAND [166]. Neutrino observatories like RNO-G [116] and IceCube-Gen-2 [117] could also potentially detect EAS.

3.3.4 Particle detector arrays

This is one of the oldest detection techniques used to measure and study CRs. It consists of setting up a set of particle detectors (stations) spaced by large distances, depending on the desired energy range sensitivity of the experiment which is also dependent on the altitude of the experiment. The detectors are usually arranged in a regular pattern, and they are able to detect the secondary particles of EAS at ground by searching for time coincidences between neighbouring stations. By measuring the signal and time delay between the triggered stations the incoming direction of the primary can be estimated to $1 - 0.5^\circ$ of zenith resolution. The core position can also be determined by using the lateral distribution function (eq. 3.3) to fit

the recorded signal at the surface detector array. The energy can also be estimated through the measurement of number of muons at ground or cross calibration with other detector systems. Different types of detection methods have been used to combine and act as particle detector arrays. These include Geiger counters at Harwell [167], hodoscopes at Kiel [168], scintillators at Volcano ranch [169] and water or ice based Cherenkov detector. Currently, scintillator based surface detector arrays and water OR ice based Cherenkov tanks are the popularly used EAS detection techniques.

Water/ice based Cherenkov tanks/detectors can also detect the secondary particles of EAS at ground. These are sensitive to the Cherenkov light which can be produced by these charged particles while travelling through the medium of the detector. The subsequent light is measured using a photomultiplier tube (PMT). This light signature is different depending on the type of the particle and thus can effectively help in differentiating between muons and electrons. The Pierre Auger Observatory uses an array of water Cherenkov tanks in conjunction with four fluorescence detectors for EAS measurements. IceCube also contains an array of ice based Cherenkov detectors which are used for cosmic ray studies and as a veto for their underground neutrino detectors. More details about the Pierre Auger Observatory are presented in the next chapter 4

Scintillator based particle detector arrays can be used to distinguish between the different secondary particles of an EAS. These consist of scintillating material which produced detectable photons if a charged particle traverses through the material. If deployed at the surface, such detectors can act as excellent discriminators for electron and muons whereas if deployed underground they can only detect muons. The size of the scintillating material controls the zenith angle sensitivity which typically decreases as the inclination of the shower increases. TA uses a vast array of scintillator based detectors along with three fluorescence detectors to measure EAS. The Pierre Auger Observatory is also testing an array of underground muon detectors which are situated directly below its surface array stations.

3.3.5 Towards detecting Neutrino Induced Extensive Air Showers

Neutrino induced air showers can be differentiated from a regular CR induced EASs by their unique signature. These showers are supposed to start much deeper in the atmosphere in comparison to ordinary CR showers, in particular proton showers which act as the primary background for their detection. The deeper interaction means less shower development till the shower front reaches the ground in comparison to a cosmic ray induced EAS. This difference in development can be measured by the muon to electron ratio at ground via a particle detector array. Since, the neutrinos are only expected to interact to induce an EAS if the volume of the atmosphere through which they traverse is large enough, for zenith angles less than 60° either the neutrinos are not expected to interact till they reach the ground or and even if they do, due to the general amount of atmospheric volume at these angles the CR induced EASs are supposed to be indistinguishable from a neutrino shower, at least for a particle detector array at ground. This is due to the fact that the CR induced EASs have not developed enough to significantly reduce or lose their electromagnetic component. This

leaves the primary distinguishing factor i.e. the muon to electron ratio the same for neutrino and CR induced EASs. The terminology used to determine the development of the shower in the atmosphere is the shower age and typically showers having a larger muonic component at ground are called *old showers* while showers having a larger electromagnetic component at ground are called *young showers*.

Thus, to detect a neutrino induced EAS using surface detector arrays the smoking gun signal is an inclined (\approx zenith angle $> 60^\circ$) "young" shower. A perfect neutrino air shower detector should have a good angular resolution and a large electron-muon signal separation. However, this signature also not completely background free. Such a signature can also be caused by deeply interacting CR primaries or highly energetic muons emitting bremsstrahlung photons both of which can also induce a young shower at large zenith angles. B meson could also be misidentified as a neutrino as shown in [170]. Other processes such as low energy showers coincident with an EAS could also act as background for a neutrino detection. These have been studied in detail in [23] and are negated in the analysis through the techniques developed in the reference.

The Pierre Auger Observatory

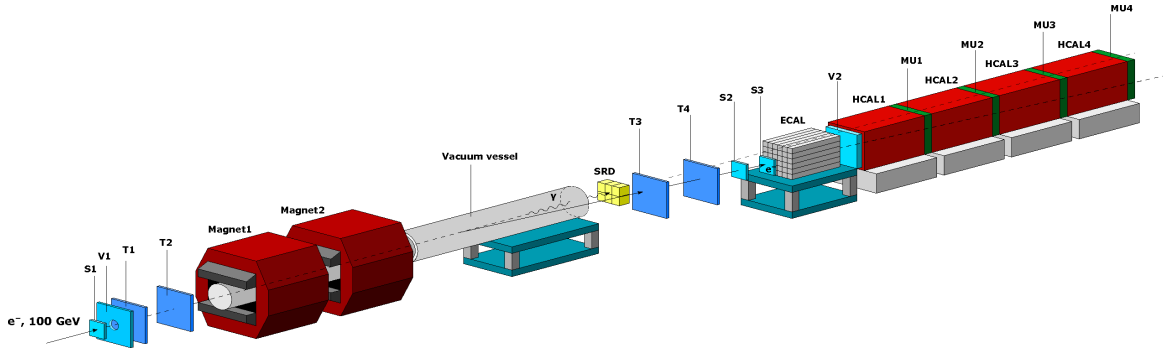


Figure 4.1: Invisible mode setup []

The Pierre Auger Observatory [8] is the largest CR observatory in the world. Located outside Malargüe in the Argentinian *pampas*, the observatory spans across an area of 3000km^2 . Originally conceptualized in the 1990s, the Observatory was built in the early 2000s and fully completed in 2008. Geographically the site is located near the base of the Andes at an altitude of 1400m above sea level and is relatively flat across its whole span. The Observatory was designed to detect CR-induced EASs having primary energy of 10^{17}eV to 10^{20}eV and beyond. It does so by identifying the EAS via two different complementary detecting components: *Surface Detector* array (SD) and the *Fluorescence Detector* (FD). A schematic of the observatory is shown in fig. ???. The SD consists of 1660 water Cherenkov tanks spread in a triangular grid with 1.5 km spacing. The FD consists of four sites with 27 telescopes located at the edges of the ground array and overlooking the sky above. The Observatory also consists of various atmospheric monitoring devices such as LIDARs [171], laser facilities CLF and XLF [172, 173] and other weather sensors to constantly monitor the atmosphere which is important for FD operation. With the AugerPrime upgrade of the Observatory which is scheduled to be finished in 2024 two new detecting components are being added: The *Radio Detector*(RD) [174] and the *Underground Muon Detector*(UMD) [175]. The SD

is also being upgraded with the addition of a scintillator on top of the tanks [176]. Each individual component of the new upgrade is not discussed in detail since they are not used in the context of this thesis but only AugerPrime as a whole and its potential for detecting neutrinos at the Pierre Auger Observatory is discussed.

Even though, the primary objective of the Pierre Auger Observatory is UHECR physics it is also sensitive to the neutrino induced EAS signature via both the SD and FD. The low neutrino interaction probability requires a detector that is always active. The high duty cycle of the SD $\approx 100\%$ compared to a limited duty cycle of the FD $\approx 10 - 15\%$ makes SD the more probable of the detector to detect neutrinos. This has already been shown in previous neutrino searches at Auger where the search with the SD provides the stringiest limits for neutrino searches at the Observatory [18]. This chapter aims to provide a short review of the different components of the Observatory with a focus on the SD and its trigger system since it is the primary detector used for the analysis presented in this thesis.

4.1 Fluorescence Detector

The Fluorescence Detector system at the Pierre Auger Observatory consists of an array of Fluorescence telescopes that are constantly looking inwards over the surface detector array trying to measure the nitrogen fluorescence induced by the EAS. The FD consists of 24 telescopes located at four different small hills (Coihueco, Los Morados, Loma Amarilla and Los Leones). The Coihueco site also consists of High Elevation Auger Telescopes (HEAT) which can be tilted upwards to extend the field of view at the Coihueco site. Each of the 24 telescopes has a field of view of $30^\circ \times 30^\circ$ in azimuth and elevation. The combination of the telescopes gives an azimuth coverage of 180° . The HEAT telescopes can extend the field of view by a further 30° in elevation. This gives a 100% triggering efficiency for EAS above 10^{19} eV for FD and above 10^{17} eV with the inclusion of HEAT. Currently, the FD is always operated in combination with SD. As mentioned before the measured fluorescence light gives the deposited shower energy which is about 90% of the total. The remaining 10% which is carried by non-fluorescence producing particles such as neutrinos and muons is corrected with simulations [177]. The expected fluorescence yield (combined for all wavelengths) is affected by the temperature, pressure and humidity of air [178]. This is constantly monitored at the Observatory via several monitoring instruments. Each FD site is equipped with a LIDAR station which continuously monitors the aerosol profile, cloud and sky cameras which photograph the sky to estimate the cloud coverage and wind and rain sensors for the safe functioning of the FD telescopes. Two laser facilities Central Laser Facility (CLF) and eXtreme Laser Facility (XLF) have also been functional since 2003 and 2008 respectively. These help provide hourly measurements of the atmospheric aerosol content and can also be used to measure FD performance.

Fig ?? shows an FD site along with the schematic of an FD telescope. The fluorescence light enters through the UV filtered window which is surrounded by a corrector ring. A spherical segmented mirror is used to gather the incoming light and focus it onto a 440 pixelated

PMT camera. The camera records the light pulses every 100ns and based on a hierarchical trigger [177] saves the event. For reconstructing the energy and the geometry of the shower the recorded information is combined with the information detected by the SD (hybrid) or other FD telescopes (stereo) [179]. A relative calibration of the PMTs is performed for each camera before and after each night of data taking [177]. A regular absolute calibration procedure called the X-Y scanner has also been developed and is currently being deployed at each FD telescope.

The FD acts as an important calibration tool for the SD, especially for the energy estimation where the hybrid detection of EAS is used to provide a simulation free primary energy estimate for the SD. It can also be useful for looking into high energy atmospheric phenomena such as ELVES [180]. The low duty cycle of the FD is $\sim 15\%$ which is due to its operation being limited to clear moonless nights, limits its overall capabilities, especially for a neutrino analysis. However, the FD has been used for up-going neutrino searches [(ANITA Paper)] and also has a potential use to look for atmosphere skimming CRs or neutrinos.

4.2 Surface Detector

The Surface Detector is a Water Cherenkov Detector(WCD) array which is used to detect the EAS on the ground particularly the footprint by detecting the shower particles that reach the ground. Each WCD [181] comprises a tank with 3.6 m diameter and 1.2 m height. It also consists of a reflective inner liner containing 12,000 liters of ultra-pure water. Three 9-in PMTs look into the water and detect the Cherenkov light produced by the charged shower particles as they traverse through the water. With the AugerPrime upgrade the WCDs have also been equipped with a scintillator, additional PMT and a radio detector on top. These are described later in section 4.3. Each WCD tank also has its own electronics and communication system. All of the components are powered using a solar panel. An artistic representation along with all the components is shown in fig. ??.

The 1.5 km grid spacing is commonly referred to as SD-1500. There are further sub-arrays within the SD, SD-750 also called the infill and SD-433 with the numbers representing the distance between the tanks in the sub-arrays in meters. Each WCD can be operated on its own with each PMT signal first recorded at the station and then combined using a Central Data Acquisition System (CDAS) [8] which uses a ranked system of triggers to decide if the combination of all WCDs is a candidate for an EAS event. The data taking process of the SD is described in more detail in the following sections. Due to its autonomous nature, the SD array is easy to maintain and has a duty cycle $\sim 100\%$. The array is only affected if there is a communication outage or if the solar panel cannot generate power for an extended time period both of which are rare at the site of the Pierre Auger Observatory.

4.2.1 Calibration of SD

The PMT signals in the WCDs are digitised by a 40MHz 10 bit *flash analog-to-digital converters* (FADCs) [182]. One of the signals is taken from the anode of the PMT and is called the *low gain* (LG) channel and the other is taken by the last dynode and is amplified by a factor of 32 and is called the *high gain* (HG) channel. The two signals provide sufficient precision and range to record both the signals produced near the shower core (~ 1000 particles/ μ s) and those produced far from the core (~ 1 particles/ μ s). The signal trace is recorded at a sampling rate of 40MHz with a total of 768 bins leading to each bin width corresponding to 25ns. Due to varying electronics across the WCDs a robust procedure is needed to calibrate each station to a universal unit of measurement for the SD. Also, due to the remoteness of the WCDs such a procedure needs to be performed locally for each station to allow for its functioning even in the case of individual broken PMTs. The unit of measurement used to calibrate the SD stations is called *vertical equivalent muon* (VEM). This is the charge deposited by a vertically central through-going (VCT) muon in the WCD station. The SD station by itself cannot select these particular muons but the normal SD measurement of all atmospheric muons has been studied in comparison with a muon telescope that only triggers these VCTs for a reference tank [183]. This measurement is used to calibrate the SD.

To perform the calibration charge distribution, Q_{VEM}^{peak} , and the pulse height, I_{VEM}^{peak} , both for the individual PMTs and their sums, are compared to the measurements done with a muon telescope as shown in fig. ???. The first peak in the figure for the PMT measurement is caused due to low energy particles while the second peak is produced by the atmospheric muons. This peak corresponds to $Q_{VEM}^{peak} \sim 1.03$ VEM for the sum and ~ 1.09 VEM for each PMT. The shift in comparison to the muon telescope measurement is caused by the convolution of photo-electron statistics on an asymmetric peak in the track length distribution and local light collection effects. This peak is used to obtain a conversion for the integrated signal of the PMT to VEM units. In addition to this, since the subsequent trigger for the SD also requires a measure of the current I_{VEM} , this value also needs to be converted and calibrated to VEM units [182]. The same technique as the charge calibration is employed since the VCTs also produce a peak in the pulse height histograms. The calibration is performed every 60s and sent to CDAS thus for an incoming event, calibration data is available for the preceding minute ensuring high calibration accuracy.

4.2.2 SD Trigger system

There are three types of different types of station level triggers scalar, calibration and shower trigger. The scalar trigger records signals for very low thresholds and is useful for supplementary physics such as space weather [184]. The calibration trigger, as explained in the previous section, helps store and calculate the calibration parameters. The main shower trigger, used to record the EAS events is a hierarchical system consisting of two local triggers (T1 and T2) implemented at the station level, a third level trigger (T3) implemented by a CDAS and further event selection triggers (T4 and T5) stored by the SD but only

used depending on the analysis and the quality of data required by the said analysis. The hierarchical nature arises from the limits on the wireless communication network required for a vast autonomous array. The trigger aims to reduce the rate especially for the expected muonic background and at the same time maximising the EAS event detection. A schematic of the logic of the trigger system is shown in fig ??.

Old triggers

The T1 trigger consists of two parts/modes both of which need to be satisfied for an event to be checked for the possibility of higher level triggers. One of them is a basic threshold trigger (TH) that requires the signal for each of the three PMTs to be above $1.75I_{VEM}^{peak}$. If there are only one or two PMTs active then the requirement changes to $>2.8I_{VEM}^{peak}$ or $>2I_{VEM}^{peak}$ respectively. The TH mode is used to select large signals which are expected for very inclined CR induced showers ($\theta > 60^\circ$) which are dominantly muons. It reduces the rate for the atmospheric muons from 3KHz to a 100Hz. The second mode for the T1 trigger is called time-over-threshold (ToT). ToT requires 13 or more of the 25ns time bins within a $3\mu s$ window to be above a threshold of $0.2I_{VEM}^{peak}$ for at least two PMTs. Since this mode filters for signals spread in time it is sensitive to low energy vertical showers nearer to the core and also high energy inclined showers far from the shower core. It is also very effective in filtering random muonic background which typically has a spread of 150ns compared to the 325ns spread for ToT fulfilment. The rate for ToT at each detector is ~ 1.2 KHz with the main contribution being two consecutive muons arriving within the time window.

New triggers

In June 2013, two additional T1 trigger modes were implemented in the Pierre Auger Observatory to reduce the influence of muons and reduce the energy threshold of the array. The two modes both of which build upon the ToT condition are time-over-threshold-deconvolved (ToTd) and multiplicity-of-positive-steps (MoPS).

The ToTd trigger was first proposed internally in [185](Change to correct). The trigger aims to deconvolve the FADC trace, suppressing the exponential tail of the diffusely reflected Cherenkov emission before applying the ToT condition. This helps in compressing the signal from a muon which typically has a fast rise time in one or two time bins before the application of the ToT condition. The trigger has an expected rate of 0.2-3Hz. ToTd also requires the integrated signal to be above 0.5 VEM. An example of the functioning of the trigger is shown in fig. ??.

The MoPs trigger [185] was implemented to achieve a similar goal as ToT and ToTd i.e. a better separation between the air shower signal from the mostly muonic background. It is designed to do so by counting the number of positive steps(cumulation of successive increases) in the FADC trace within a $3\mu s$ sliding window. These steps are expected to be above a certain threshold (5xRMS noise) and below a maximum value (~ 0.5 VEM). The MoPs trigger is satisfied if more than 4 positive steps are counted during the sliding window

in at least 2 PMTs. The expected rates both from simulations and data taking are found to be $< 2\text{Hz}$. MoPs is even better at recovering lower signals compared to ToT and ToTd, thus improving the overall trigger efficiency. Both ToTd and MoPs are implemented as an OR logic with the ToT condition.

These triggers particularly improve the trigger efficiency and sensitivity for photon and neutrino induced EAS. The trigger efficiencies for the different T1s implemented at the Pierre Auger Observatory are shown in fig ?? . By rejecting the signals caused by muons or other low energetic particles the triggers are expected to increase the low energy threshold for the detection of these particles. They also help in recording more low electromagnetic like signals which is the expected signature for photons and neutrinos.

Array Level Triggers

T2 level triggers aim to apply higher constraints to T1 triggers. A T1-ToT trigger is automatically updated to a T2-ToT trigger while a T1-TH trigger requires the signal to pass a higher threshold condition of $> 3.2 I_{VEM}^{peak}$ for three coincident PMTs to get upgraded to T2-TH. For two (one) working PMTs the threshold is stricter at > 3.8 (4.5) I_{VEM}^{peak} . After the T2 level, the expected station rate of events drops to $\sim 23\text{Hz}$. The T2 level triggers from all stations are sent to the CDAS to form a global trigger.

The T3 level aims to build a condition based on both spatial and temporal combinations of stations that have passed the T2 condition. It again has two modes with only one needed to be satisfied to form a successful T3. Both of these conditions use a unit of detector called the crown, C_n . The crown as shown in fig ?? is a set of concentric hexagons centred around each station with n giving the order of the surrounding hexagons, 1 being the nearest. The first mode $ToT2C_1 \& 3C_2$ (??) requires three SD stations which have passed T2-ToT criteria. It further requires at least one station to be located in the first crown denoted by $2C_1$ and the last to be located in the second crown ($3C_2$). The trigger is efficient in selecting compact vertical showers ($\theta < 60^\circ$) and selects about 90% of the physical events at the array. The second mode $2C_1 \& 3C_2 \& 4C_4$ (??) is less restrictive and aims to select showers with moderate compactness. It requires a 4-fold coincidence of stations having any type of T2s (T2-ToT or T2-TH). The first two neighbouring stations must be again located in the first and second crown, but the last station can be as far as the fourth crown. This mode is more efficient in selecting inclined showers which typically being rich in muons have a sparse detector triggering pattern. Along with the spatial requirements both of the modes also require each of the T2 triggers in the stations to be within $(6+5C_n)\mu\text{s}$ of the first one. Once either of the modes is satisfied all the FADC signals from the detectors passing T2 as well as signals from the detectors only passing T1 which are within $30\mu\text{s}$ of the T3 are stored by CDAS as a part of the event. This process is described in more detail in [8]. With the present trigger setup, the Observatory records about 3 million SD events per year [8].

The next two triggers T4 and T5 are used to improve the data quality. Unlike T1-T3 these are implemented off-line. Both check for the geometry and the timing compatibility to select showers in the T3 events. The T4 trigger uses either of the two different criteria to select

showers. The first is the requirement of a 3-ToT compact configuration i.e. three nearby stations satisfying the T2-ToT condition in triangular patterns shown in fig. ???. The second criterion, 4C1 requires the main triggered station to have at least three triggered tanks out of its six first neighbours as shown in fig. ???. Both the criteria work in collaboration with each other, 3ToT configuration has a selection efficiency of $\sim 99\%$ for showers below 60° and the 4C1 configuration helps to recover the rest $\sim 1\%$ showers lost below 60° and also selects low energy events above 60° . This trigger is not used for the neutrino analysis.

The T5 fiducial triggers help improve the quality of the showers selected, especially for an accurate energy and angular reconstruction. The trigger ensures the selection of showers that are well contained in the detector array to avoid miss-reconstruction of the core. There are two severity levels for the triggers called 6T5 and 5T5. The former requires all six stations in the first crown around the station with the highest signal to be functional while the latter only requires five. The 6T5 condition helps negate the showers that might fall at any hole in the detector array. These holes can be due to natural obstacles or non-functional tanks. Since 6T5 also improves the angular resolution and improves the overall quality of the selected showers this criterion is used in the search for neutrinos, especially for angles below 75° . Above 75° since most of the events expected are elongated along a single line the fulfilment of the T5 criteria is very difficult, thus this trigger is not used.

4.3 AugerPrime

AugerPrime [56] also called Auger Phase 2, is the ongoing upgrade of the Pierre Auger Observatory to improve its sensitivity and detection capabilities. The upgrade aims to both improve the already present detector systems and also plans to add new components to the Observatory. One of the key aims of the *AugerPrime* upgrade is to improve the estimation of the primary CR mass measured by the SD. This is done by the installation of plastic scintillators (*Surface Scintillator Detectors* (SSDs) [176] on top of the WCD tanks. The differing responses of WCDs and the SSDs to the electromagnetic and muonic components help enhance the overall mass sensitivity of the detector for vertical showers. The upgrade also replaces the SD electronics (*unified board* (UB) and SD front-end board) with the *upgraded unified board* (UUB) [186] and adds a *small* PMT (sPMT) [187] to the WCD. The UUBs allow for better station level processing power to account for the SSD and also add a faster sampling rate and better timing accuracy for the SD. The sPMT helps increase the dynamic range of the WCD by reducing the saturated signals in the stations closest to the shower axis. The *AugerPrime* upgrade also includes the deployment of plastic scintillators beneath the WCD tanks, the *underground muon detector* (UMD) [175] as an extension of AMIGA [188] across the SD-750 and SD-433 sub arrays. The UMD is sensitive to the penetrating muon component of the EAS is very useful for extending the lower energy detection range of the Observatory and can also help in photon searches [189]. Deployment of radio antennas on top of each WCD to form *radio detector* (RD) [174] is also a part of *AugerPrime*. This will allow for the measurement of the radio component of the EAS which

originates primarily from the electromagnetic component. Such a measurement especially at very inclined zenith angles will allow for an improved mass estimation even for higher zenith angles where the SSD is insensitive. Additionally, increasing the duty cycle of the FD by operating the telescopes during higher night sky brightness periods with reduced PMT gain is also a part of the upgrade.

In the context of this thesis, the data from the ongoing upgrade and the preceding test array were not used. However, it is important to mention that the higher sampling rate available with the UUBs and the addition of RD could offer a way to improve the current neutrino analysis. The higher sampling rate could help in reducing the effect of the background muons especially at lower zenith angles ($\sim 60^\circ$) whereas the RD in conjunction with WCD could help improve the neutrino detection efficiency for higher zenith angles ($\gtrsim 75^\circ$) by improving the T3 efficiency. Also, a general increase in the statistics and continued data taking till the 2030s will help enhance the limits in case of non-detection of cosmogenic neutrinos which have further important implications for the CR spectrum especially for the cutoff as discussed before. The upgrade will also help improve the multi-messenger astronomy capabilities of the Observatory.

4.4 The Offline Framework

The Offline framework [190, 191] is the C++ based software developed internally by the Pierre Auger Observatory to reconstruct air showers and perform cosmic ray analysis. It can process and reconstruct both air shower simulation outputs from generators such as CORSIKA [192], Aires [193] etc. and the data recorded at the Observatory. Offline aims to standardize basic quantities such as detector response for simulations and important variables inferred from reconstructing an EAS for the entire Collaboration. This helps in providing the collaboration with a homogenous backbone to build physics analysis. It also allows for the physics analysis to be stored and implemented within the framework which helps in leading and optimising productivity. The modular design allows it to be constantly updated for the addition of new functionality and detectors. The framework is available internally on Gitlab to the entire Collaboration with regularly planned public releases. Offline consists of three fundamental constituents as shown in fig. ???. These are summarised below:

Detector description: This part acts as an input and consists of information about the individual detector systems of the Pierre Auger Observatory. The information is available to the data processing modules as needed but cannot be modified. The static information such as the layout of the detector is stored in XML files whereas the time dependent information such as atmospheric conditions, hardware changes, calibration information etc. is stored in MySQL databases. For real events this allows for an almost perfect duplication of the conditions and for simulations it offers a vast range of available detector configurations.

Event data: This part is used to store the important event variables required by modules or the end physics analysis. This includes basic detector level information such as measured or reconstructed signal traces, trigger information etc. to reconstructed variables such as energy, direction or X_{max} . The information is transferred to the data processing modules based on the use case. For a simulation, the event information is first provided to the modules to generate the detector response which is then further reconstructed. In such cases true MC values, detector response and the reconstructed quantities are all stored in the event data. Whereas, for real recorded data since the detector response is already present only the reconstruction is performed by the data processing modules. Event data acts as both an input and output for the data processing component of the framework.

Data processing: The type of task performed by the Offline is controlled using the data processing components. The different tasks are implemented using individual modules where each module is a self-contained algorithm with the ability to read the detector description. The modules can also read and write event data. Since the modules do not interact with each other they can be easily updated and new modules can be used in an analysis in a plug and play fashion. The different modules can be implemented sequentially in a chosen order based on the analysis. This is controlled via an XML file called Modulesequence.xml. The modules also have adjustable parameters which can either be controlled using individual XML steering files of each module or using a central XML file called bootstrap.xml. There are various standard pre-defined sets of module sequences and bootstraps available in the Offline framework which can be directly used without any alterations. For this analysis, one standard reconstruction SdDglNeutrinoReconstruction was tweaked to perform a neutrino search with MoPs and Totd. Two new reconstruction modules SdDghNeutrinoReconstruction and SdNeutrinoSimulation based on previously done analyses were also adapted and added to the Offline framework. The exact modules used in the different neutrino analyses and a description of their functionality are mentioned in the following chapters.

4.4.1 Advanced Data Summary Tree

Advanced Data Summary Trees(ADSTs) are ROOT [194] based file structures developed internally within the Pierre Auger Collaboration to store the output of the reconstruction. Additionally, it can also be used to store low level information such as detector description, calibration information and also the configuration of the Offline framework used to produce the ADST. ADSTs can be used to browse through individual events via the Eventbrowser and carry out higher level physics analysis. Since the structure is based on ROOT ADSTs can be read through different programming languages. In the context of this analysis the ADSTs are interfaced within C++ directly and in python using modules such as Python Instrumentation Kit (PyIK) [195] and uproot [196] in Python.

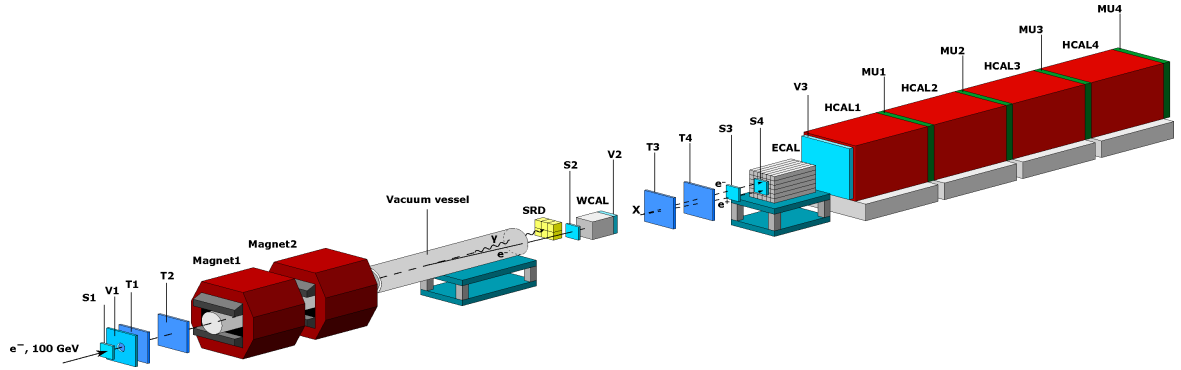


Figure 4.2: Visible mode setup 2017 []

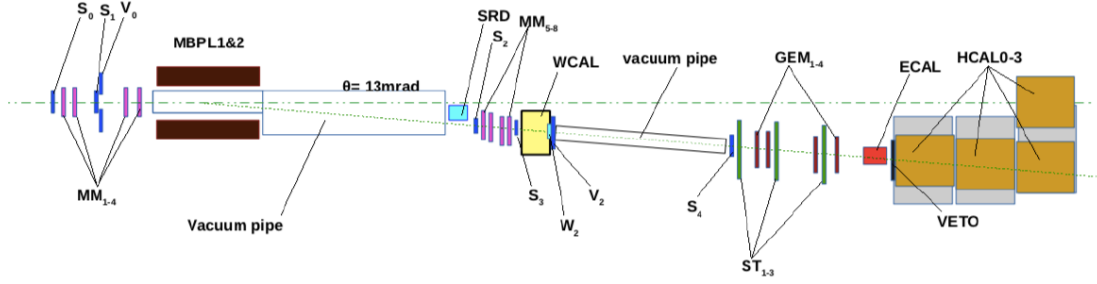


Figure 4.3: Visible mode setup 2018-top view []

Invisible Mode: $A' \rightarrow \chi\bar{\chi}$ signature:

$$\begin{aligned}
 & \text{Beam}(p \simeq 100 \text{ GeV}), \\
 & E_{\text{ECAL}+PS} (< 100 \text{ GeV}), \\
 & V_2 (< E_V^{\text{th}} \simeq 1 \text{ MIP}), \\
 & E_{\text{HCAL}} (< E_{\text{HCAL}}^{\text{th}} \simeq 1 \text{ GeV}).
 \end{aligned}$$

Neutrino Analysis $60^\circ < \theta < 75^\circ$

This chapter gives a brief summary of the neutrino search performed for the zenith range $60^\circ < \theta < 75^\circ$. The neutrino search is separated into different angular ranges to maximize the performance of the detector array, in this case the SD, for the search. The chapter aims to cover the expected signature in terms of measurable quantities in the Pierre Auger Observatory for the particular angular range, a description of the neutrino simulation used to develop the analysis and the reconstruction chain used to reconstruct the neutrino simulations with the Offline framework. Further, the quality cuts used are analysed in more detail, especially in the context of improving the capability of the search by the usage of MoPS and ToTd. In the end, the improvements to the neutrino detection efficiency with the inclusion of MoPS and ToTd is quantified.

5.1 SD Neutrino signature $60^\circ < \theta < 75^\circ$

The strategy and method to detect neutrino showers in this angular range with the SD remain the same as mentioned before in sec. 3.3.5 i.e. to try detecting showers that develop late and have more electromagnetic or "young" shower front at ground. In terms of signal in the SD array, the young shower is expected to be spread over a longer time period, typically hundreds of nanoseconds, and have a lower maximum peak compared to signal induced by older showers which are spread over tens of nanoseconds and have a higher maximum peak. A comparison of the difference between the induced SD signal from a young and old shower arriving from the same zenith angle is presented in Fig. ???. However, such differences in signals and the ability of the SD to differentiate between a neutrino induced and a proton/heavy nuclei induced shower disappear for vertical showers ($\theta < 60^\circ$). For vertical showers, a UHECR induced EAS does not have enough time to develop because of the limited thickness of the atmosphere. At these zenith angles a high energy UHECR induced EAS can mimic the expected young shower signature of a neutrino induced EAS at the ground. Thus, currently, the neutrino searches at the Pierre Auger Observatory are limited to zenith angles above 60° where it is much easier to separate a neutrino induced

EAS from a UHECR induced EAS. Since we are also searching for young showers which have not fully developed till they are detected at the ground, reconstructed energy cannot be used as a discrimination criterion.

To select the longer signals in the SD one of the variables that was used in erstwhile neutrino searches at Auger is the fraction of ToT-T2 triggered signals in the recorded event. As mentioned in the previous chapter this trigger is tuned to select broader signals, which for an inclined shower is evidence of a young shower. For the search presented in this thesis along with the ToT-T2, the ToTd and MoPS are also used. Both ToTd and MoPS as mentioned in sec. 4.2.2 help further increase the selection efficiency for broader signals by reducing the impact of low energy muons. These muons form the majority of the background at low zenith angles of the selected search range. Thus, these triggers are impactful in increasing the separation power for low energy (≤ 1 EeV) neutrino showers. Another important variable that is used to judge the width of the signals is Area Over Peak (AoP). The AoP is defined as the ratio of the integrated signal of the station over the biggest value or peak of the signal. The AoP is calibrated in such a way that narrow or old shower signals have $\text{AoP} \sim 1$ while broad/old shower signals have $\text{AoP} \geq 1$.

5.2 Neutrino Simulations

To characterize the neutrino search ability of the Pierre Auger Observatory Monte Carlo simulations of EASs induced by UHEVs are required. There are six possible neutrino interaction channels due to the three possible neutrino flavors with each having two possible channels (CC or NC). However, for simulations these are envisioned to be characterised by just two sets of simulations. For the NC channel since the EAS induced by three neutrino flavors has the exact same signature for our detector only ν_e NC simulations were performed for to estimate the NC contribution of all the three flavors to the final detection efficiency.

For the CC interactions, in the case of ν_μ the resulting high energy muon has a high probability of evading detection. This signature very similar to the NC interaction where the resultant secondary neutrino also carries approximately 80% of the primary energy and probably evades detection. Thus, after taking into account the appropriate cross-section, in principle, the NC simulations can be used to also estimate the contribution of ν_μ CC channel to the detection efficiency.

In the case of ν_τ CC interactions where the resulting τ especially at higher energies (≥ 1 EeV) can decay and also initiate a secondary shower resulting in a "double bang" like signature in the Observatory. In the context of this thesis, such signatures are not accounted for and the ν_τ CC interaction is treated in the same way as the ν_μ CC interaction resulting in a possible underestimation of the detection potential of the Observatory to ν_τ events. A future ν_τ simulation library is currently being prepared by the Pierre Auger Collaboration Monte Carlo task and could help extend this analysis in the future.

Thus, in summary, ν_e CC and NC simulations can be considered to be good approximations to estimate the contributions of all the other channels to the overall exposure of the

Observatory. The simulations were produced in two parts by the Pierre Auger Collaboration Monte Carlo task based on the GAP note [23] and input from the author. The first part entails the simulation of the ν induced EAS in the atmosphere and the second consists of simulating the appropriate detector response for the corresponding shower.

5.2.1 Atmospheric Shower simulations

CORSIKA (COsmic Ray Simulations for KASCADE) [192], a simulation software for modelling extensive air showers in the Earth's atmosphere was used to generate the EAS initiated by a ν primary. The simulation parameters are defined through files known as input cards. An example of the input cards used to generate simulation for this analysis is provided in Appendix ???. The first step involved simulating the primary neutrino-nucleon interaction which is performed in CORSIKA using the HERWIG [197] code. Further, options such as CHARM to track charm secondaries are not used. Also since only ν_e simulations are simulated, the TAULEP option which handles ν_τ and $\bar{\nu}_\tau$ is also not used. The systematic uncertainties related to the primary interaction estimator are discussed later in section 6.2. CORSIKA further tracks and simulates the interactions of the primary interaction products as they travel in the atmosphere toward the ground constituting the air shower. It offers a wide variety of choices regarding the hadronic interaction models it uses to simulate these interactions. For the simulations used in this study separate high and low energy hadronic interaction models were used. For energies higher than 200 GeV three high energy hadronic models QGSJET-II.04 [198], SYBILL 2.3d [199] and EPOS-LHC [200] were compared. The results of the comparison are mentioned in detail in Appendix ???. Since the differences between the models are not that significant for the neutrino analysis SYBILL 2.3d was chosen as the high energy interaction model. For lower energies FLUKA [201, 202] was chosen. The systematic uncertainties arising from different models are discussed in section 6.2.

To account for the curvature of the Earth which is especially important for the zenith angles studied, the EGS4 [203] Monte-Carlo method is chosen to simulate the electromagnetic component of the shower. The analytical NKG method based on eq. 3.3 which is also available but is not used for these simulations since it vastly underestimates the maximum of the electromagnetic component due to the fact it does not account for a curved atmosphere. Global Data Assimilation System (GDAS) measurements at Malargue [204] were used for atmospheric profile chosen for the simulations. The magnetic field components are taken to be the default values at the Malargue site ($B_x = 19.52\mu\text{T}$ and $B_z = -14.17\mu\text{T}$).

Further, since the computing times taken for shower simulations scale roughly with the primary energy, for primary energies $>10^{16}\text{eV}$ these times become extremely long. Though parallel computing provides a viable solution, the technique of "thin sampling" or thinning [205] offers an alternate way to reduce the computation times while simultaneously avoiding the waste of resources. The thinning algorithm is applied to all particles below the adjustable fraction of the primary energy that emerge from an interaction. Only one of these particles is followed, and a proper weight is assigned to this particle to account for the untracked ones which are dropped based on the thinning level ($\epsilon_{\text{th}} = E/E_0$). Additional

Add The
CORSIKA
steer file to
appendix

information about the application and the improvements to this process can be found in [206, 207]. A thinning value of 10^{-6} is used for the simulations in this study.

The simulations were performed using the GRID technology [208, 209]. Both CC and NC showers were simulated for fixed energy steps of $\log(E/\text{eV}) = 0.5$ in the range $10^{17} - 10^{20.5} \text{eV}$. The number of simulated showers was varied depending on the Energy, atmospheric depth of interaction and the injected zenith angle. More showers were simulated at lower energies and the energy dependent numbers are tabulated in table 5.1. Further, for both the interaction channels within the zenith angle range $60^\circ - 70^\circ$ the neutrinos were forced to interact at fixed atmospheric depths in steps of 100 g cm^{-2} . The injection points both close to the ground where a neutrino shower might have a lower trigger efficiency and close to the top of the atmosphere where a neutrino induced shower might mimic one induced by a proton are rejected for the simulations. The azimuthal angle is left free and can take any value between 0° and 360° . The simulated depths for each zenith angle bin are also summarised in table 5.1. The values for the simulations are exactly the same as used in the previous analysis [23].

$\log_{10}(E/\text{eV})$	16.5	17.0	17.5	18.0	18.5	19.0	19.5	20.0
# Showers per (θ, X)	300	200	150	50	50	50	50	50
# Resampling in Offline CC	100(200)	50(100)	50(100)	10(50)	10(50)	10(50)	10(50)	10(50)

θ_{MC}	60°	63°	66°	69°	72°	75°
Interaction Depths (X)	13	14	17	19	23	29
Max interaction depth (g cm^{-2})	1640	1820	2040	2330	2720	3270
Min. interaction depth (g cm^{-2})	140	220	140	230	120	170

Table 5.1: Table to test captions and labels.

Based on (E, θ_{MC}, X) bin the number of CORSIKA showers simulated vary. Higher values were chosen for lower energies to increase the statistics since at these energies the simulated shower has a lower chance of being detected by the detector.

After the simulation is completed CORSIKA produces a normal particle output file that contains information about the surviving particles at the ground level which is set based on the detector elevation. The file contains the relevant information such as energy, momentum, and timing all segregated for each particle based on its Particle Data Group Code [62]. It also produces a ".long" file that contains the longitudinal distribution of various particle numbers along with the energy deposited which is relevant analyses that use the FD. For this work, the normal particle output files were used for further processing to simulate a response in the Pierre Auger Observatory SD.

5.2.2 Surface Detector Response

The next step required to complete the ν -induced shower simulation is to generate an appropriate detector response in the SD array for each simulated atmospheric shower. This is done using the Offline framework (sec. 4.4). The framework can read in the CORSIKA output files, undo the applied thinning, simulate the Cherenkov light which will be produced as the particles travel through the WCDs and then also mimic the corresponding WCD electronics outputting the trigger and event information for each simulated shower akin to how real showers are measured at the Observatory. Each step is performed using special modules. The module sequence used to simulate the detector response for ν -induced showers in this thesis is given below:

```
<sequenceFile>
<enableTiming/>
<moduleControl>
  <loop numTimes="unbounded" pushEventToStack="yes">
    <module> EventFileReaderOG </module>
    <!-- increase numTimes if you want to throw the shower
    into the array more than once -->
    <loop numTimes="5" pushEventToStack="yes">
      <module> EventGeneratorOG </module>
      <!-- simulation of muon background -->
      <module> SdAccidentalInjectorKG </module>
      <module> G4StationSimulatorOG </module>
      <loop numTimes="unbounded" pushEventToStack="no">
        <module> CachedShowerRegeneratorOG </module>
        <module> G4TankSimulatorOG </module>
      </loop>
      <module> SdSimulationCalibrationFillerOG </module>
      <module> SdPMTSimulatorOG </module>
      <module> SdFilterFADCSimulatorMTU </module>
      <module> SdBaselineSimulatorOG </module>
      <module> TankTriggerSimulatorOG </module>
      <module> TankGPSSimulatorOG </module>
      <module> CentralTriggerSimulatorXb </module>
      <module> CentralTriggerEventBuilderOG </module>
      <module> EventBuilderOG </module>
      <module> EventFileExporterOG </module>
    </loop>
  </loop>
</moduleControl>
</sequenceFile>
```

The *EventFileReaderOG* reads in the CORSIKA output file. The following steps are performed assuming an "ideal" SD array with every station operational and fully efficient within the design limits. The steps are also repeated for an individual shower between 300-10 times depending on the primary energy to further increase the statistics for each (E, θ, X) bin. The first module, *EventGeneratorOG*, sets the core position, time and event ID for Monte Carlo events. In this analysis similar to [23] the core position is only allowed to be randomized over a $5 \times 5 \text{ km}^2$ area around a fixed station at the centre of the array. This is done to increase the overall simulation statistics for this study and also allows for an in depth study of how core position could impact the reconstruction which is discussed later. In the next step, the *CachedShowerRegeneratorOG* reads in the list of the shower particles and un-thins each particle injecting a set of new particles based on its unique weight [210]. It can then create a list of particles for each SD station which is then passed to the next module, *G4TankSimulatorOG*. *G4TankSimulatorOG* uses Geant4 [211–213] to simulate the particle trajectories in the WCD and the corresponding Cherenkov light produced by these particles. It also handles all possible absorption and reflections the light can suffer before it is measured by the PMT. Following this the *SdSimulationCalibrationFillerOG* simulates the detector calibration constants described in sec.4.2.1 and the *SdPMTSimulatorOG* takes in the information from the tank simulator and simulates a corresponding PMT signal (trace). *SdFilterFADCSimulatorMTU* and *SdBaselineSimulatorOG* further simulate the processing of the PMT signal by the electronics at each station with the former applying the filter response and the FADC sampling and the latter adding baseline and simulated noise to these traces.

The next two modules decide whether the simulated event fulfils the hierarchical trigger system of the Observatory explained in sec. 4.2.2. *TankTriggerSimulatorOG* checks if the signal fulfils the local station criteria i.e. T1 and T2 condition. Following this the *CentralTriggerSimulatorXb* further combines all the stations which fulfil the T2 criteria to form the T3, simulating the task performed by CDAS for real data. The *CentralTriggerEventBuilderOG* and *EventBuilderOG* then facilitate the transfer of events passing the T3 criteria from the simulation container class to the event class with the last module *EventFileExporterOG* responsible for exporting all the processed showers now with the applied detector response in a file which can be used for further reconstruction.

5.3 Shower Reconstruction

The event reconstruction is a necessary step before any further analysis can be performed. This procedure is developed first for neutrino simulations to enhance their identification efficiency and to study the possible background. Once fixed the reconstruction is also applied on the measured data to look for neutrino like events. Shower reconstruction is also performed within the Offline framework with a module sequence that contains a combination of some standard reconstruction modules and some specific modules developed for neutrino identification in GAP note [23]. The reconstruction is again performed with the help of the MC task on the GRID framework based on the particular reconstruction chain developed for

neutrinos. The Module sequence used to reconstruct simulated neutrino showers is given below:

```
<sequenceFile>
<enableTiming/>
<moduleControl>
  <loop numTimes="unbounded" pushEventToStack="yes">
    <module> EventFileReaderOG </module>
    <module> EventCheckerOG </module>
    <module> SdGainRatioCorrectorKG </module>
    <module> SdStationCheckerOG </module>
    <module> SdHistogramFitterKG </module>
    <module> SdBaselineFinderKG </module>
    <module> SdTraceCalibratorOG </module>
    <module> SdSignalRecoveryKLT </module>
    <module> SdMonteCarloEventSelectorOG </module>
    <module> SdEventSelectorOG </module>
    <module> SdTopDownSignalSelectorUGR </module>
    <module> SdPlaneFitOG </module>
    <module> LDFFinderKG </module>
    <module> DLECorrectionWG </module>
    <module> SdEventPosteriorSelectorOG </module>
    <module> RecDataWriterNG </module>
  </loop>
</moduleControl>
</sequenceFile>
```

The sequence remains similar to the one used in [23] apart from the iterative development performed by the Offline developers over the years. For data reconstruction, the *SdMonteCarloEventSelectorOG* is omitted from the sequence. The chain can be subdivided into three main parts which are "event reading and pre-selection," "angular reconstruction" and "posterior selection and export" which are discussed in the next few sections.

5.3.1 Event reading and pre-selection

The first module in this part of the reconstruction is again the *EventFileReaderOG* which depending on the input format can parse the file. In the reconstruction sequence, it is used to read in either the detector response simulated file for simulations or the measurement files obtained from the SD. The *EventCheckerOG* further checks if the stations in each read event have proper timing information. After this point, the FADC traces are processed with various modules to covert them to VEM units. The *SdGainRatioCorrectorKG* corrects for the gain ratio for the electronics followed by *TriggerTimeCorrection* which further corrects for differences in electronics especially related to timing for data over the course of its

operation. The *SdStationCheckerOG* further checks the station quality and appropriately sets silent stations if they do not contribute to the final trigger formation. After this point the *SdHistogramFitterKG*, *SdBaselineFinderKG* and *SdTraceCalibratorOG* which get the calibration constants from the calibration traces, fit the baseline and convert the traces to VEM units. Further, *SdStationPositionCorrection* corrects the positional differences that might arise due to faulty GPSs which is important for correct timing information, *SdBadStationRejectorKG* sets known bad stations in the array to be non-operational and the *SdSignalRecoveryKLT* which tries to recover signals from the saturated PMTs if any by looking at the undershoot value [214, 215]. An extra module *SdPMTQualityCheckerKG* is also used in the case of data reconstruction to estimate the quality of the detector.

The next three modules are used to fine tune the selection of signals and later events to improve both the quality of simulated and measured data to increase the efficiency of neutrino detection. The first one is the *SdEventSelectorOG* which applies a basic SD event selection which is also used in other analyses. The module sets conditions based on T4, T5 and other station based parameters if appropriate. The different operations performed by the module are as follows:

- **Bottom-up Selection:** This selection helps in deciding the non-participating stations if the stations are not compatible with a planar shower front propagating at the speed of light hypothesis [216]. Such stations can arise due to random noise in the array or due to random coincidences between non-air shower events with air shower events. The selection requires a minimum of three stations that fit the planar front of the shower within lenient time tolerances. It also removes isolated stations by checking the distances to nearest neighbours. Although the selection is applied, it is not very effective for inclined showers ($>60^\circ$) since the showers above these angles are not geometrically compact. Thus, this selection is supplemented with an extra top-down selection implemented in *SdTopDownSignalSelectorUGR* which is discussed later.
- **T4 and T5 trigger:** The module also calculates the T4 and T5 criteria discussed in sec. 4.2.2. It then further discards events if they do not fulfil these criteria. In this study, the T4 criteria was not used but a stringent 6T5 criteria was required for the selection.
- **Lightning Rejection:** The lightning events can be detected in the SD stations by looking for an oscillatory signal in the FADC trace of all three PMTs [217]. For this analysis, if any lightning like signal is detected in any one of the stations the whole event is rejected from the analysis.
- **ToTd and MoPS trigger:** The module can also silence particular triggers before applying the selection. This feature is used to produce two sets of reconstruction files one with the triggers turned off and one with them turned on to check the impact of the new triggers. This can impact the number of events fulfilling the 6T5 conditions and thus the overall number of events which can be seen later.

The *MonteCarloEventSelectorOG* further removes stations with distance in shower plane coordinates smaller than the inner radius used in the CORSIKA simulations. It also removes dense stations i.e. virtual stations which are sometimes used for MC studies since these are not representative of the regular SD array.

The *SdTopDownSignalSelectorUGR* is a module developed specifically to carry out a top-down selection and accidental signal rejection for neutrino like events. A summarised overview of what this module aims to accomplish is given next with a detailed description of the module already published in [1](Billor?). The Top-down procedure is applicable for both the simulations and measured data whereas the accidental signal treatment is only applied for measured data. The procedure is based on [2] and [3]. Top-down selection requires a minimum of three stations with the shower front time tolerance compatibility dependent on the zenith angle. If the fit does not converge stations are successively removed and re-tested until a satisfactory fit is achieved. At the end of the procedure stations which do not contribute to the final fit are rejected while the others are marked as candidate stations. Further, the Top-Down procedure also takes into account the individual traces and uses the shape for 3-fold topologies. It also rejects isolated signals akin to the Bottom-up selection but with larger tolerances to account for the wider footprint of inclined events. The module also applies an accidental signal rejection procedure before the top-down procedure is applied to account for the atmospheric muon background. The atmospheric muons and also local showers can either trigger isolated stations or even real event stations affecting the start times and in turn the zenith angle reconstruction. This miss-reconstruction can either cause problems with the fitting of the top-down procedure and can also lead to non-neutrino like or background events past the analysis cuts affecting the overall neutrino detection efficiency. The module discards stations with total signals below 3 VEM which rejects the muonic background which typically peaks at 1 VEM. The discarding procedure is implemented only till the minimal number of stations present in the event is below 6.

Since the parameters of the module were evaluated without the consideration of MoPS and ToTd especially for the segment selection procedure slight changes were made to the module. The segmentation procedure was not applied to the stations which had a MoPS/ToTd trigger. These stations were only subjected to the top-down selection procedure. Further, the accidental station cut was lowered till the minimum number of stations present in the event are below 5 compared to 6 to account for the increased number of stations expected with the inclusion of new triggers. This was done after the partial unblinding of the test sample and is described in more detail in sec. 6.3.1. These changes were only implemented for the sample where the new triggers are included and the sample where they are not remains unchanged.

5.3.2 Angular Reconstruction

The angular reconstruction forms the basis for neutrino detection using the SD especially since for inclined neutrinos the primary energy estimation algorithms typically used for CRs at the Pierre Auger Observatory become unreliable. The angular reconstruction is performed by the *SdPlaneFitOG* and *LDFFinderKG*. The primary energy estimation using the SD is

typically done using the *LDFFinderKG* which fits a lateral distribution function to the SD signal based on the NKG approximation. The NKG approximation is typically inaccurate for inclined showers above a zenith of 60° thus alternate methods based on muon maps are used for CR inclined showers. These also fail for neutrino induced showers which in our detection scenario usually have a large electromagnetic component. Thus, without a reliable energy reconstruction, angular reconstruction becomes vital for neutrino induced shower detection at the SD. A summary of the method and the procedure is presented below based on a detailed description which can be found in [215].

The angular reconstruction procedure uses the timing information from the stations to fit either a plane or a spherical shower front. The axis of shower \hat{a} is initially assumed to intersect the ground at some time using a signal weighted barycenter x_b and bary-time t_b of selected stations located at x_i with start time t_i given by :

$$\vec{x}_b = \frac{\sum_i S_i x_i}{\sum_i S_i} \quad \text{and} \quad t_b = \frac{\sum_i S_i t_i}{\sum_i S_i} \quad (5.1)$$

The choice of the weights taken as \sqrt{S} with S being the signal of the stations has been previously evaluated using Monte-Carlo studies to give the best results. The barycenter also serves as the first estimate of the impact position of *shower core* at the ground but is later estimated more accurately. The shower core is assumed to be moving in the $-a$ direction. Under the plane-front assumption the particles in the shower front move in a plane perpendicular to the shower axis (*showerplane*) with the same speed as the core of the shower which is the speed of light, c , the time, $t(\vec{x})$ when the shower plane passes through some chosen point, \vec{x} (e.g. a station on the ground) can be inferred through a simple projection onto the shower axis as,

$$ct(\vec{x}) = ct_b - (\vec{x} - \vec{x}_b) \cdot \hat{a} \quad (5.2)$$

Assuming a minimal change in altitude which is true for the SD location and precise knowledge of station locations the deviations in estimating the geometrical shower parameters can be due to the uncertainty of the observed start times σ_i . Thus, the following function needs to be minimized to fit the model for the measured signal start times

$$\chi^2 = \sum_i \left(\frac{t_i - t(\vec{x}_i)}{\sigma_{t_i}} \right)^2 \quad (5.3)$$

Add the
schematics

where t_i are the start time of the signals of station i located at $x_i = \vec{x} - \vec{x}_b$. The minimization of the χ^2 is performed using MINUIT [218]. For the start time variance determination the standard model described in [215] is used. Modifications for new triggers have been suggested in [(Coleman thesis)], but these have not yet been approved by the Collaboration for wider use. Replacing the axis with $a = (u, v, w)$ and the station coordinates with $x = (x, y)$ (ignoring altitude z). Adding the constraint $u^2 + v^2 + w^2 = 1$ the χ^2 can be easily solved. The solution only fails if the stations used while fitting have a linear dependence (three stations in a line) but for higher station multiplicity this is highly improbable, especially for the theta

range explored for the DG_{low} channel.

Another shower front estimation technique based on a curved shower front approximation is also used to fit the measured stations. The reconstruction called the *Observer*, assumes the shower development starting at time t_o from a point of origin x_o propagating toward the ground as a concentrically expanding sphere with the speed of light, c . The arrival time of the shower front at point \vec{x} can thus be estimated as:

$$t(\vec{x}) = t_o + \frac{|\vec{x} - \vec{x}_o|}{c} \quad (5.4)$$

As can be seen by the equation, the spherical fit is decoupled from any prior knowledge of the shower core or the shower axis. It is only dependent on the point of origin. Quantities such as the shower axis can be determined later when the impact point, \vec{x}_c has been estimated as $\hat{a} = (\vec{x}_o - \vec{x}_c)/(\vec{x}_o - \vec{x}_c)$. The expected solid angle differences between the two fits are of the order of half a degree. The curvature shower front fit is only used for station multiplicities greater than five. This is so because for lower station multiplicities the degrees of freedom are not enough to solve for the shower-front curvature. A side by side comparison for an event for both plane fit and spherical fit is shown in fig. ??.

5.3.3 Posterior selection and Export

The last part of the shower reconstruction chain includes the application of the *SdEventPosteriorSelectorOG* module which computes the 6T5 *posterior* trigger differing from the 6T5 criteria mentioned earlier. The 6T5 posterior requires the 6 stations in the first crown from the nearest station to the reconstructed shower axis to be active or alive during the event. The events which do not pass this criterion are rejected. The last module *RecDataWriterNG* exports all the relevant information to ADST 4.4.1 files. In the case of reconstructed simulations, both the simulated and reconstructed information are stored while for measured data only the reconstructed information is stored.

5.4 Reconstructed ν simulations

This section includes some sanity checks to check and verify the quality of the ν simulations. Fig shows the Efficiency of the reconstructed showers as a function of the zenith angle and the slant depth. The next figure shows the frequency of reconstructed events based on the core position. The non-uniform distribution with minimal events for core positions close to the stations can be explained arising due to two reasons. The first is the removal of stations if the PMTs for the particular station are saturated. This saturation can occur for stations very close to the core. The second reason What to include here? Theta distributions, AoP distribution comparisons, Core position distributions, Residuals, Xmax distributions etc.

Expand with plots

5.5 ν selection

This section tries to describe the decisions made to select ν induced air showers. The selection is optimized and evaluated on the above-mentioned neutrino simulations and a part of the measured data is used as an estimate for the expected background. Since a *blind search* strategy is envisioned for the search. The rest of the measured data forms the *search sample* and will be used to look for neutrino like events during the *unblinding*. In the first part the selection used to identify ν showers is described in more detail. The selection consists of some pre-selection cuts applied to enhance the reconstruction quality of the selected events followed by a Fisher Linear Discriminant [219] based on experimental observables which is the main criteria of differentiation between a ν induced air shower and background. In the second part, the performance of the selection is further evaluated based on temporal changes such as ageing in the surface detector and the neutrino detection efficiency is quantified. Comparisons to previously used selection are also presented especially in the context of the performance improvements achieved by using new triggers for neutrino detection.

5.5.1 Samples Used

As mentioned above to devise an efficient neutrino selection good quality training samples for both signal and background are required. Monte-Carlo simulations described in 5.2 are used for the signal sample. For the background sample a portion of real data (20%) is used. Due to the low flux prediction of neutrinos a large portion of the measured data if not all is expected to be nucleonic air showers. Simulated showers could also serve as background sample, but this is not done due to the following reasons. For the energies that are investigated in this search the high uncertainties observed for the air shower simulations, particularly due to hadronic interaction models could lead to errors. Further, the simulations are still incomplete i.e. they tend to sometimes ignore some physical processes and also do not account for all the possible and sometimes unpredictable detector effects which could be important for the neutrino search. Using measured data as background is advantageous here as it already contains all the possible effects. Also, due to the vast parameter space looked at for the neutrino search such a simulated background sample would require huge amount of computing resources.

The number of 20% of the measured data sample for the time period 2014-2021 is arrived at to keep the search sample i.e. the rest 80% large enough to look for neutrinos but still have enough events in the training sample for Fisher analysis. The training data for the time period corresponds to 1.29+/-?? years of the continuous measurement of a full array composed of 1420 T5 hexagons. Periods of instability or large outages marked as "BadPeriods" are rejected. The events are chosen at random across the time period from the full sample of measured data by only taking those events where the Auger SD event ID is divisible by 5. The time period is chosen to be starting from the year 2014 since by this time the array had full coverage of MoPS and ToTd. The end date of December 31, 2021 was decided in discussions with the collaboration as the end of Phase 1 of data taking of the Pierre Auger

Observatory since after this point significant changes were made to the electronics of the Surface Detector tanks as a part of AugerPrime activities as previous mentioned in sec. 4.3.

The remaining sample which consists of events with SD ids not divisible by 5 which is 80% of the full sample was unblinded in two parts. A 20% test sample was unblinded first to check if there was any need for further optimisation of the analysis and the rest 60% constituted the search sample and was used to look for neutrino candidates.

Samples Used	
MC ν training sample	Simulated events Detailed info tab. 5.1
Analysed data period - 01.01.2014 till 31.12.2021	
Background training sample	20% analysed data $1.29 \pm \dots$ yr of full Auger equivalent exposure (SD event IDs divisible by 5)
Signal search sample	20% + 60% analysed data $6.45 \pm \dots$ yr of full Auger equivalent exposure (SD event IDs non-divisible by 5)

Table 5.2: Table to test captions and labels.

5.5.2 Pre-selection Cuts

The pre-selection cuts are applied based on the unique properties of "young" neutrino like showers in comparison to older nucleon like showers. The cuts are the same as used in GAP 2013 with a slight modification to include MoPS and ToTd. These pre-selection cuts are applied in the same way to both the neutrino and background training samples.

Inclined Shower Selection: This cut aims to select showers which fall in the given angular window. The reconstructed zenith of each event is required to be in the range $58.5^\circ < \theta_{\text{rec}} < 76.5^\circ$. The range is extended by 1.5° on both sides in comparison to the simulated values from the simulations to account for the angular resolution of the detector. Further, the error on the reconstructed angle, $\Delta\theta_{\text{rec}}$ is required to be smaller than 3° to ensure the quality of angular reconstruction. The efficiency of this cut is found to be ... for CC(NC) neutrinos. The angular distribution of the background sample is shown in fig. ??.

Fiducial Quality Cut This cut also remains unchanged when compared to the previous analysis. The main aim of the cut is to ensure that the shower core for the selected event is completely contained inside the array and the stations which are used for the analysis of the event are operational. This is ensured by requiring the event to satisfy the 6T5 trigger condition. The efficiency of the cut is 100% for the neutrino simulations

by design and for the background sample this cut leads to a reduction of ... as shown in fig. ??

Young Shower Selection This cut tries to ensure the selection of events with a high electromagnetic component at ground. For this purpose events with stations having FADC traces spread in time need to be selected. As mentioned previously ToT, ToTd and MoPS triggers being more sensitive to the presence of high electromagnetic component can be used for this young shower selection. This cut ensures that more than 75% of stations in the T5 hexagon satisfy the ToT/MoPS/ToTd condition. the 75% fraction is calculated overall per event basis and the hexagon could have stations with mixtures of these triggers. The cut retains most of the neutrino events and at the same time is highly effective in rejecting background especially for high angles as shown in the fig. ??.

Angular Fit Quality A few erroneous events were discovered to have a bad geometric fit. This problem though discovered with the analysis with new triggers has always affected the neutrino analysis. To mitigate this problem a fit quality cut based on the goodness of the geometry fit was devised. The cut only accepts events which have a goodness of geometrical fit less than 200. The efficiency of the cut is ~99% for the neutrino simulations and for the background sample this cut leads to a reduction of <0.1% of events. The goodness of fit comparison for background and neutrinos is shown in fig. ??. Although the cut has minimal impact it, it ensures that one of the fundamental pillars of the analysis i.e. the geometry of the shower especially the zenith angle is well reconstructed.

5.5.3 Fisher linear discriminant analysis

The last step for the ν selection and identification involves Fisher Discriminant Analysis (FDA) also known as Linear Discriminant Analysis(LDA). This is a statistical method used to find a linear combination of features i.e. Fisher polynomial that characterizes and separates the two classes, in our case, signal and background distributions. The goal of FDA is to find a projection that maximises the distance between the projected class means while minimising the variance within each class. This ensures that the classes are well-separated in the reduced space. Mathematically, if we have a signal class represented by X_s with mean μ_s and a background class X_b with mean μ_b then the optimal discriminating hyperplane represented by w can be found by solving the equation $S_B w = \lambda S_W w$. The solution is the eigenvector corresponding to the largest eigenvalue λ . S_B is called the between-class matrix and represented as follows:

$$S_B = \sum_{i=X_s, X_b} n_i (\mu_i - \mu)(\mu_i - \mu)^T \quad (5.5)$$

with $\mu = \frac{n_s \mu_s + n_b \mu_b}{n_s + n_b}$ is the overall mean

The between class matrix S_W is given as

$$S_W = \sum_{i=X_s, X_b} \sum_{j=n_s, n_b} (x_j^{(i)} - \mu_i)(x_j^{(i)} - \mu_i)^T \quad (5.6)$$

After finding the weight vector, the projected data for each sample is given as $z_i = w^T x_i$, z_i from here on is referred to as Fisher value, \mathcal{F} . The elements of the normalised transposed weight vector are called Fisher coefficients. The method has been implemented in a standalone python program with the help of [220] and has been verified with the inbuilt LDA module of python [221] with both results agreeing within 0.01%.

Fisher polynomials and training

It is really important to find the correct features or variables to train the algorithm to achieve the best possible separation. Various combinations of input features were tested and evaluated based on the level of separation along with the shape of the tail of the background description which is important for the cut evaluation procedure. As mentioned before AoP will remain the primary feature used for discrimination. It was also shown in [23] that for the DG_{low} channel AoPs of the earliest stations closest to the core provide the best level of discrimination between data and background. This also visualized in figs. ???. Further, the zenith angle range for the search, $58.5^\circ < \theta < 76.5^\circ$ is subdivided into five sub-regions similar to [23] as shown in fig []. This is done to incorporate shower age while training the Fisher polynomial. The first four angular regions are 3° each whereas the last region is 6° . This is due to the small amount of statistics expected for higher angles which required a larger window size. For each angular window the Fisher polynomial is trained separately to maximise the analysis performance.

Different forms of the Fisher polynomial were tested, and their performance was evaluated based on the MC neutrinos passing the evaluated Fisher cut which described in the next section. In this section only two forms are mentioned, the baseline polynomials were taken to be the one described in the previous analysis [23] and the final one used for this analysis. For the first three angular regions ($58.5^\circ \leq \theta < 67.5^\circ$) a more stringent criterion which requires the AoPs of the first five triggered T5 stations was used to build the Fisher polynomial. For the remaining two angular regions ($67.5^\circ \leq \theta < 76.5^\circ$) only the first four triggered T5 stations were required. The form of the Fisher polynomial used in the previous analysis is given below:

$$\mathcal{F} = \sum_{i=1}^{4 \text{ or } 5} C_i A_o P_i + C_p \prod_{i=1}^{4 \text{ or } 5} A_o P_i \quad (5.7)$$

where C_i and C_p are the corresponding Fisher coefficients.

A modified version of this baseline polynomial was used for this analysis. The product term was found to not have a significant contribution to the separation and was thus removed

for this analysis. Further, the requirement of five stations for lower angular regions was also eliminated which effectively lowered the minimum number of stations required for each event. The form of the polynomial used is :

$$\mathcal{F} = \sum_{i=1}^4 C_i A_o P_i \quad (5.8)$$

The performance comparison of the two polynomials which is also the overall is discussed in the next section.

As mentioned before to train the Fisher polynomial 20% of the measured data sample for the time period 2014-2021 as the background training sample. Since this is measured data at the detector it is already weighted by energy (cross-section is a function of primary energy) and zenith angle (affects available detection area). For the MC neutrino events (signal sample) which do not have this natural weighting, each event is weighted by a factor of $\omega = E_{MC}^{-1} \cdot \sin(\theta_{MC}) \cdot \cos(\theta_{MC})$. The fig ?? shows the Fisher value, *mathcal{F}* distributions for both signal and background training distributions for all five angular regions. An excellent separation is achieved for all angular regions.

Fisher Cut and background estimation

After the training process a cut criterion is still needed to be established to best separate the signal and background distribution. This cut is evaluated by analysing the tail of the Fisher value distribution of the background.

The tail is fit using an exponential function in the logarithmic scale ($A\mathcal{F} + B$). The fitting is done between for the range $\mu + \sigma - \mu + n\sigma$ where μ is the mean and σ is the rms value of the distribution. n takes a value depending on the last non-zero angular bin for that region. The exponential assumption is only a reasonable guess especially due to the low statistics of the last few bins. The bin size can also affect the fit and is determined for each angular region by minimising the residual fit. This bin size is also verified with the calculator available in python to negate the possibility of over binning or under binning. Table ?? shows the *observed* and *predicted* values for the exponential fit procedure. The values are calculated by integrating from the start point mentioned in the first column till the end of the \mathcal{F} distribution. The estimate using the exponential fit mostly agrees with the observed values. It agrees the best near the mean of the distribution and becomes worse near the tails. In some angular regions a secondary bump like structure is also seen. This is attributed to the form of the Fisher polynomial and the lack of the product term. The predicted values also include the uncertainties of the fit which slightly increases the predicted number of the background events. The cut, \mathcal{F}_{cut} is calculated such that after 20 years of data taking with a full SD array 0.2 events are expected to pass for each sub-angular regions with a total of 1 background event for the full search angular range.

$$\mathcal{F}_{cut} = \frac{\log[1.25 \cdot B \cdot 0.2 \cdot \Delta(\mathcal{F})/20] - A}{B} \quad (5.9)$$

The two polynomials mentioned in the above section are evaluated based on the fraction of neutrino events passing the \mathcal{F}_{cut} . As can be seen in fig. ??, The simplified Fisher polynomial either matches or outperforms the polynomial used in the previous analysis. The comparison is done only for the case where new triggers are included. The much higher number of events in this sample are required to achieve a sufficiently high background-signal separation especially in the low zenith angular regions where previously a more stringent number of station cut was needed to reduce noise. However, the new Fisher polynomial seems to perform even better for higher angles which could lead to an overall improvement of neutrino detection efficiency irrespective of energy. This is proved later in sec. 6.1. Based on this comparison the polynomial given in 5.8 was used for signal-background separation in this analysis.

Fig ?? shows the \mathcal{F}_{cut} obtained for the different angular regions.

A two-dimensional plot with the Fisher values on an event by event basis vs the zenith angle is shown in fig ??, The blue dots represent the background events and the contour represents the signal events. The black line is obtained by setting the \mathcal{F}_{cut} to the mid value of the bin and the extrapolating for a particular sub-angular region. The background events seem to be distributed non-uniformly within the angular subsamples. The linear interpolation ensures that the effective number of events is almost constant with the zenith angle. Anything above the cut line will be considered as a neutrino candidate.

Fit Range	Number of events in \mathcal{F} tails				
	Observed - Predicted				
	Region 1 (58.5°-61.5°]	Region 2 (61.5°-64.5°]	Region 3 (64.5°-67.5°]	Region 4 (67.5°-70.5°]	Region 5 (70.5°- 76.5°]
$\mu + 1\sigma$	13	14	17	19	23
$\mu + 2\sigma$	1640	1820	2040	2330	2720
$\mu + 3\sigma$	140	220	140	230	120
$\mu + 4\sigma$	140	220	140	230	120
$\mu + 5\sigma$	140	220	140	230	120
$\mu + 6\sigma$	140	220	140	230	120

Table 5.3: Table to test captions and labels.

5.5.4 Time evolution of selection parameters

A time evolution study of the selection parameters used in the ν analysis is very important as any missed non-physical phenomenon which impacted data taking with the SD can erroneously affect the training procedure. Since the search sample is kept "blind" and the

ν selection summary					
Inclined Sel. $\theta_{rec} \in$	Region 1 (58.5°-61.5°]	Region 2 (61.5°-64.5°]	Region 3 (64.5°-67.5°]	Region 4 (67.5°-70.5°]	Region 5 (70.5°- 76.5°]
	$\delta\theta_{rec} < 3^\circ$				
Fiducial Quality	6T5				
Young Shower Sel.	75 % of T5 stations to be ToT/ToTd/MoPS				
Angular Fit Quality	$\chi^2/ndof < 200$				
Fisher Discrim. \mathcal{F}	$\sum_{i=1}^4 C_i A o P_i$ i = number of first T5 triggered stations				
$(\theta, \mathcal{F}_{cut})$	(60,)	(63,)	(66,)	(69,)	(73.5,)

Table 5.4: Table to test captions and labels.

analysis is fixed based on the training samples, any missed error during the training procedure could result in fake neutrino candidates when the search sample is unblinded.

The first step that is taken to mitigate such instances is in the way the background training sample is chosen. Since the 20% background sample is chosen randomly over the same time period as that of the search sample it already should be a good representative of the search sample. The check is still performed to look for specific features for the selection parameters such as AoP, Fisher value, Long signal fraction and the zenith angle.

The values for these parameters is plotted vs the SD Event ID which is correlated to time and represents the time evolution of the array. Fig ?? shows the evolution of the Long signal fraction with respect to the SD Event ID number. The Long signal fraction is likely to be time dependent [222] as the signal threshold for the triggers can be affected by changes in the SD stations (PMT degradation, change in linear reflectivity etc.). There is an ongoing effort to include the affect of ageing of the detector for future detector simulations [223]. Since, this work is still ongoing it was not used for this analysis.

Fig ?? show the evolution of AoP of the stations and the value of the Fisher discriminant with respect to the SD Event ID. AoP shows a slight modulation which could be related to the effect mentioned in [222] and was also observed in the previous DG_{low} analysis. This modulation was also observed to have a slight zenith angle dependence as shown in the figure. Overall, this effect is very small and is not expected to affect the analysis.

5.5.5 Neutrino Detection Efficiency

In this section, the detection efficiency at each stage of the ν selection procedure is identified. The efficiency is affected by a myriad of factors such as neutrino flavour, NC or CC interaction, energy, zenith angle and slant depth of interaction. The list is presented in table 5.5. The

numbers are calculated with respect to the events remaining after the precedent cut. They are presented sequentially ordered according to the application of the cut in the selection chain. The values are obtained from MC simulations assuming a fully functional surface detector array.

ν selection efficiencies			
Cut		Efficiency	
		CC	NC
Inclined Selection	$58.5^\circ < \theta_{rec} \leq 76.5^\circ$	90%	96%
Fiducial Quality	6T5	90%	96%
Young Shower Selection	75 % of T5 stations to be ToT/ToTd/MoPS	90%	96%
Angular Fit Quality	$\chi^2/\text{ndof} < 200$	90%	96%
Station Cut	No. of T5 triggered stations ≥ 4	90%	96%
Neutrino Selection	\mathcal{F}_{cut}	90%	96%

Table 5.5: Table to test captions and labels.

The inclined shower selection removes $\sim x\%$ of showers. These showers were previously discussed in section 5.4. Most of these events are showers which interact very close to the ground which can lead to a mis-reconstructed zenith angle. Further, calculating the impact of $\Delta\theta_{rec}$ a stronger reduction is observed in NC than CC events. The error distributions for both channels are given in fig ???. The error seems to worsen with increasing zenith angle and reduction of shower energy. These are the two areas where the reconstruction algorithm does not perform properly as in both cases the number of triggered stations are very few and additionally in the second case certain geometrical patterns such as a line can impact the zenith angle determination.

The fiducial quality cut is already a part of the reconstruction algorithm and is thus not evaluated in this section.

The long signal trigger fraction impact

It is also observed that the Fisher discrimination has different efficiency based on the channel. It seems to perform better for the CC channel in comparison to the NC channel. This is further analysed by looking at the AoP distribution for the two channels in fig. ??. On average the CC events have a higher AoP value in comparison to the NC events. The values of AoP for NC lie in between the CC and the background events. This makes for a less efficient separation for the NC channel. Overall NC channel events seems to retain a lower electro magnetic component when they reach the ground in comparison to the CC events. This was already shown in the previous analysis.

Fig ?? shows the comparison of the neutrino detection efficiency w.r.t. the zenith angle

Write more
after the
numbers

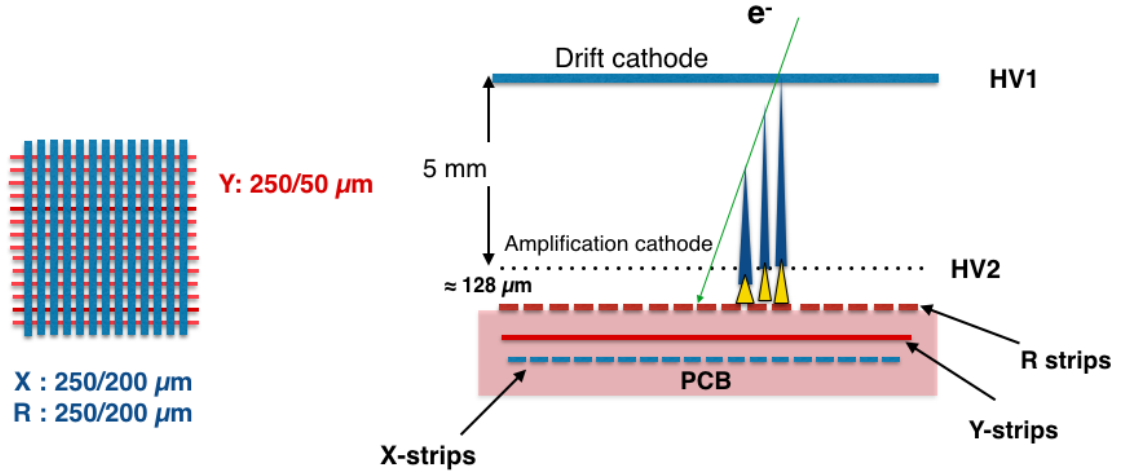


Figure 5.1: Left: Strip dimensions of the modules, Right: NA64 Micromega's working principle []

for the CC channel at different primary energies. The plot is compared to the one shown in the previous analysis. Overall the efficiency increases with energy reached maximum values for $\sim 10^{20.5}$. The efficiency increases as a function of zenith angle with a maximum efficiency for $\theta_{MC} \sim 70^\circ$. The efficiency slightly decreases for angles above $\sim 73^\circ$, since for very inclined showers the electromagnetic component at ground is significantly less, which affects the identification efficiency. Another factor contributing to this decrease for higher zenith angles is the quality cut on $\Delta\theta_{rec}$ which disproportionally affects the highest zenith angles since the angular reconstruction algorithm is not optimized for very inclined showers.

It was observed that by using the new triggers a 500-200% improvement can be achieved for the neutrino search for the DG_{low} channel especially for the CC channel. The effect of the improvement decreases for higher energy and is the most prominent for energies up to $\log E_\nu = 18.5\text{eV}$. There are several effects which contribute to this improvement. The new triggers increase the overall number of events especially for lower energies as shown in fig ???. The other factors which are different in this analysis is the reduction of the minimal T5 station requirement for the low angular regions and the change of the Fisher polynomial also contribute to the overall neutrino detection improvement in comparison to the previous analysis. A similar behaviour is observed for the NC channel albeit with a reduced overall efficiency in comparison to the CC channel.

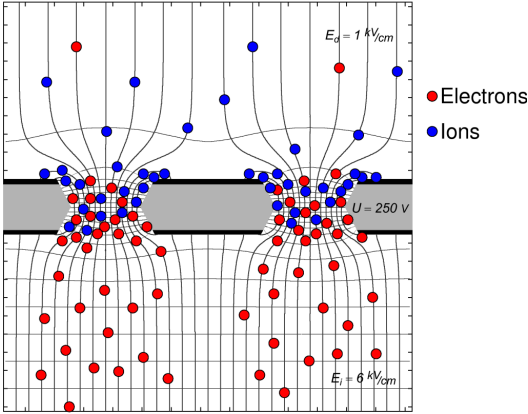


Figure 5.2: A sketch of GEM field lines [].

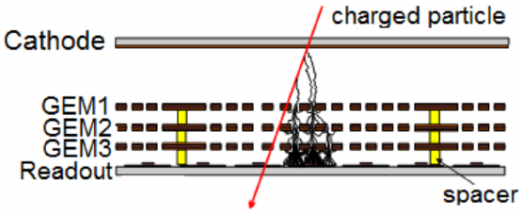


Figure 5.3: Schematic of a triple GEM detector along with the working principle []

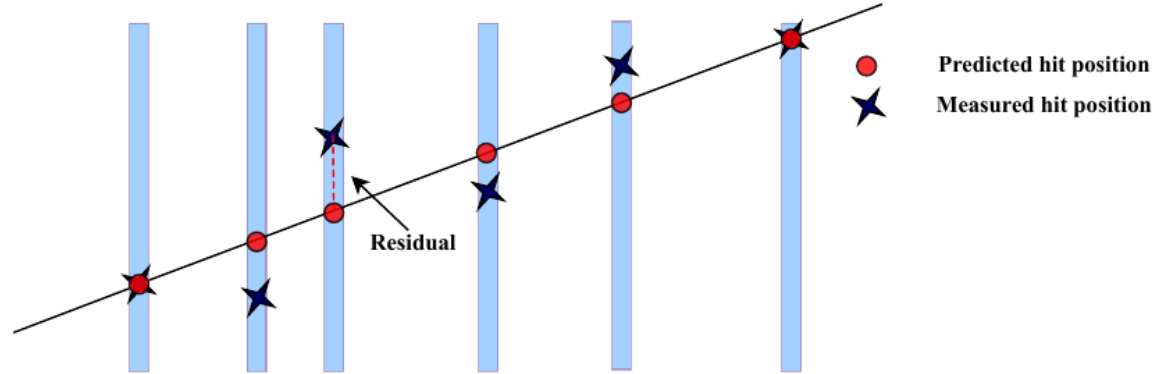


Figure 5.4: Linear regression pictorially.

Detector exposure and Limits to the diffuse flux

The chapter aims to detail the procedure used to calculate the detector exposure or sensitivity to neutrinos for the DG_{low} region. The efficiencies calculated in the last chapter are used and the final expected neutrino rates are calculated. The first part of the chapter describes the exposure calculation along with the exposure contribution from different channels. Systematic uncertainties which can arise during the full analysis along with their contribution to the exposure are also discussed. The second part of the chapter details the results of the unblinding where no possible neutrino candidates were found for the angular range. Using this information an upper limit on the incoming flux of UHE ν is calculated. This limit is further compared to the one obtained by the previous analysis for the same time period but without the contribution of new triggers. The overall improvement forms a crucial result of this work.

6.1 Exposure Calculation

One of the most accurate techniques used at Auger to calculate the exposure of the SD array to UHE ν is through extensive simulations of different detector configurations. In this method MC neutrino showers are thrown over varied detector configuration to calculate the effective or active area at each instant of time. Since the detector configuration of the SD array is constantly changing(*faulty tanks, regular maintenance etc.*), sometimes on a daily basis, this technique requires a large amount of computational time and resources making it less desirable for use in this analysis.

In this analysis, a different approach based on the 6T5 condition, which is required for each selected event in this analysis, is used for the exposure calculation. For this calculation, the 6T5 hexagon is taken to be the smallest possible detection unit for the ν event. The effective area i.e. the area seen by the incident cosmic neutrino for this detection unit at full efficiency is given by the Brillouin area [224], $A_{6T5} = 1.95\text{km}^2$ as shown by the shaded

area in fig ?? . The aperture for this detector unit is dependent on the energy of the primary neutrino ,the slant depth in the atmosphere, X , neutrino flavor, type of the interaction, zenith angle, azimuth angel and the point of impact of the shower on the ground. The effective *acceptance* of the detector unit can be written as follows:

$$A_{hex}(E_\nu, X) = \int_{\phi=0}^{\phi=2\pi} d\phi \int_{\theta_{min}=58.5^\circ}^{\theta_{max}=76.5^\circ} A_{6T5} \cdot \varepsilon(E_\nu, X, \theta) \cdot \sin\theta \cos\theta \cdot d\theta [\text{cm}^2 \text{sr}] \quad (6.1)$$

,where $\varepsilon(E_\nu, X, \theta)$ is the neutrino detection efficiency for each simulated energy, slant depth and zenith discussed in the last chapter. An example for a particular combination is given in fig. ?? . Plots for efficiency for each combination can be found in ...

The next step involves integrating the *acceptance* over the different simulated injected slant depths (as given in table 5.1). This accounts for the *effective mass* target for the neutrino identification over the 6T5 hexagon unit. It is calculated as follows.

$$M_{hex}(E_\nu) = \int_X A_{hex}(E_\nu, X) \cdot dX \quad (6.2)$$

Fig. ?? shows the effective mass for both CC and NC interaction channels for a single 6T5 hexagon unit. Like the detection efficiency it increases with energy.

Exposure calculation still needs to account for the detector configuration and its evolution over time. We reduced our array to units of 6T5 hexagons and a full SD array consisting of 1660 stations consists 1420 of these hexagons. Since the establishment of the Pierre Auger Observatory the active number of 6T5 hexagons are monitored every second. This forms a very good indicator for the time evolution of the SD array since any non-working station or large periods of instability are intrinsically recorded in the number of active 6T5 hexagons at that time. The instantaneous number of hexagons, $n_{hex}(t)$ thus can be used as an indicator of detector configurations over time. The $n_{hex}(t)$ were updated and calculated every minute and have an uncertainty of about 1.5% as mentioned in [224]. To calculate the energy dependent exposure, the effective mass of one 6T5 hexagon is multiplied by the instantaneous number of hexagons and integrated in time. Further, the ν interaction probability for each flavour($i = \nu_e, \nu_\mu, \nu_\tau$) and channel($c = \text{CC}, \text{NC}$) is also folded in. The exposure is given as:

$$\xi^{i,c}(E_\nu) = \frac{\sigma^{i,c}(E_\nu)}{m_N} \int_t M_{hex}^{i,c}(E_\nu) \cdot n_{hex}(t) \cdot dt = \frac{\sigma^{i,c}(E_\nu)}{m_N} \cdot M_{hex}^{i,c}(E_\nu) \cdot N_{hex} \quad (6.3)$$

, $\sigma^{i,c}(E_\nu)$ is the neutrino nucleon cross-section [225] and N_{hex} is the total number of active 6T5 hexagons integrated in time over the search period. The value for N_{hex} calculated for the period analysed is . The energy dependent exposure for different flavors and interaction channels is shown in fig ?? . It is necessary to point out again that the double bang showers which can be produced by ν_{tau} are not taken into account for this analysis which was also mentioned in sec. 5.2

An effective or total exposure, $\xi_{tot}(E_\nu) = \sum_i \sum_c \xi^{i,c}(E_\nu)$ is calculated by summing all the

interaction channels and assuming a 1:1:1 flavour ratio at earth (large propagation distances combined with neutrino oscillations) as shown by the red line in fig ??.

As seen in the figure the ν_e CC channels contribute the most to the total neutrino exposure (~85%). The exposure rises rapidly at lower energies and then mostly flattens with just a slight increase which is due to the energy dependent neutrino cross-section. The shape is due to the neutrino detection efficiency which is small at lower energies as shown in fig ?? in the last chapter. The next dominant channels are the ν_τ and ν_μ which have a similar detection efficiency as the NC channel but have a higher value of cross-section. The NC channel contribution is very small (~5%) due to the reasons discussed in section 5.5.5.

The exposure calculated in this analysis is compared to the one calculated using the previous analysis for the same time period in fig ??. For the CC channel a 5x improvement is seen at lower energies and a 2x improvement at higher energies. For NC this improvement is not that significant. There is a 2x improvement at lower energies and a 1.5x improvement at higher energies. The improvement at lower energies is due to the inclusion of the new triggers MoPS and ToTd which enhance the detection efficiency at lower energies. The improvement at higher energies is mainly due to the improved Fisher analysis. The total exposure is also improved by a factor of ...

6.2 Systematic uncertainties

Determine
what to
write

6.3 Data unblinding

As mentioned before in section ?? the search data comprises of all events recorded at the Observatory between 2014-2021 which have a SD ID number non-divisible by 5 i.e. 80% of all SD data recorded between 2014-2021. This search data sample was further split into a 20% test sample similarly where SD ID numbers divisible by 4 were taken to be a part of the test sample while the rest became the part of the 60% search sample. This split was done to perform the unblinding in two stages. The first where only the test sample is unblinded to detect any flaws with the analysis and if and when those flaws are fixed, the rest of the data is unblinded. This exercise turned out to be useful as a slight flaw was uncovered during the unblinding process of the 20% test sample which was corrected. Said flaw which is described in more detail later required the whole reconstruction process along with the training of the Fisher polynomial to be performed again. This also led to the unblinded 20% test sample to be blinded again since the reconstruction was altered. The splitting procedure was repeated and the total unblinding was performed again in parts. It is important to mention in all of unblinding procedure **0 neutrino events survive** the analysis selection. This section is thus split into two subsections. The first describing the unblinding of the 20% test sample along with the changes brought about by this unblinding. The second section details the full unblinding of the redone search samples (test + remaining) and discusses the interesting

features of the unblinded search samples.

6.3.1 20% test sample

The Fisher value distribution for the test sample is shown in fig ?? . As it is shown no event passes the Fisher cut in any angular region. However, there are a few events which come very close to the cut line. Five events marked with a red circle were analysed in more detail. Each of them has its own unique reason with only the one with zenith being the most interesting. This event has the ID of 66106356. After looking at detailed information about the event it was found out that the accidental station cut used is insufficient. Previously, the accidental cut (rejection of stations with Totalsignal < 3 VEM) is only applied to the event if there are more than 5 stations in the event. Since for this analysis due to the inclusion of MoPS and ToTd an overall increase in events is expected which also increases the overall number of stations with accidental stations this cut needs to be reduced a bit to take this overall increase into account. Thus, this cut was reduced to apply for events with more than 4 stations. This reduction of the cut decreases the total events passing the analysis cut by $\sim 5\%$ for the background training sample and 1 – 2% for the signal training sample. The Fisher coefficients and cut changes slightly as shown in table ?? . After this change in the reconstruction the test sample was obtained again as shown in fig ?? . The other interesting events which have \mathcal{F} values close to the \mathcal{F}_{JNU} with their respective ids are tabulated in table ?? . These events were individually evaluated. Some of these () were found to have a bad time residual fit primarily because of multiple peaks observed in stations triggered by the new triggers. Since, no segmentation algorithm was used for stations with MoPS and ToTd triggers sometimes a wrong peak was selected which affected the reconstruction for these events. A future analysis with a corrected segmentation algorithm which is functional for the new triggers MoPS and ToTd is envisaged in the future analysis upgrades. Such events are expected to be limited to less than $\sim 1\%$ of total events but still require a careful look for future analysis upgrades. A further detailed analysis was also performed for these events where the primary mass composition was extracted via the muon production distributions as mentioned in [226]. Even with large uncertainties these events are most likely due to a light deep primary. For the other three events no particular feature worth mentioning was observed.

6.3.2 Reevaluated 20% test search sample and 60% search sample

After the unblinding of the test sample and changing the cut mentioned in the section above, the unblinding was again performed in two stages. Initially a 20% part was unblinded and then the remaining 60% blinded sample was analysed. Again **0 neutrino candidates** were found after candidate selection. The results of the unblinding for each sub-angular bin is presented in fig ?? along with the Fisher value as a function of zenith angle presented in fig ?? . The results (red) are overlaid over the training(orange) and test (blue) samples with the dashed lines indicating the value of the \mathcal{F}_{JNU} obtained according to eq. ?? . As it can be seen the distributions are compatible to each other within statistical fluctuations. The overlay

also confirms that the exponential tail assumption is a reasonable enough to determine the $mathcal{F}_{cut}$. The goodness of the fit is once again presented in tab. 6.1 in the form similar to table 5.3. This time for the observed values the numbers are calculated from the much larger search sample. It is found that the tails of the distributions which typically seemed to have fit badly also fit reasonably well. The events in the search sample that have \mathcal{F} values close to the $\mathcal{F}_{\text{J}\cap\text{U}}$ were again carefully checked and were found to be either due to the issues with the segmentation algorithm or known issues such as partial shower containment or large number of non-working PMTs both issues have also been seen in previous analysis.

Fit Range	Number of events in \mathcal{F} tails Observed - Predicted				
	Region 1 (58.5°-61.5°]	Region 2 (61.5°-64.5°]	Region 3 (64.5°-67.5°]	Region 4 (67.5°-70.5°]	Region 5 (70.5°- 76.5°]
$\mu + 1\sigma$	13	14	17	19	23
$\mu + 2\sigma$	1640	1820	2040	2330	2720
$\mu + 3\sigma$	140	220	140	230	120
$\mu + 4\sigma$	140	220	140	230	120
$\mu + 5\sigma$	140	220	140	230	120
$\mu + 6\sigma$	140	220	140	230	120

Table 6.1: Table to test captions and labels.

6.4 Diffuse limit for the UHE neutrino flux

Since no neutrino candidate was found in this analysis, an upper limit to the flux of the incoming $\text{UHE}\nu_s$ can be evaluated. Let flux per unit area, A , energy, solid angle ω and time be denoted by $\phi(E_\nu) = \frac{d^6 N_\nu}{dE_\nu d\omega dA dt}$. The expected number of detected neutrinos can be calculated by folding in the total exposure $\xi_{tot}(E_\nu)$ with flux as follows,

$$N_{\text{expected}} = \int_{E_{\text{vmin}}}^{E_{\text{vmax}}} \phi(E_\nu) \cdot \xi_{\text{tot}}(E_\nu) \cdot dE_\nu \quad (6.4)$$

Assuming a differential $\text{UHE}\nu$ flux $\phi = k \cdot E_\nu^{-2}$, the integrated upper limit on the value of k is given by:

$$k_{\text{up}} = \frac{N_{\text{up}}}{\int_{E_{\text{vmin}}}^{E_{\text{vmax}}} E_\nu^{-2} \cdot \xi_{\text{tot}}(E_\nu) \cdot dE_\nu} \quad (6.5)$$

, the value of N_{up} for a given confidence level can be determined based on the number of observed events and the number of expected background events. Different statistical methods can be used to obtain the value for N_{up} based on the confidence interval. In the next sections

some of these different statistical approaches are discussed in more detail. The Feldman and Cousins limit with an extension that incorporates the systematic uncertainties discussed above is chosen as a final estimate for N_{up} .

6.4.1 Feldman and Cousins limit

Feldman-Cousins method [227] is a statistical technique used to construct confidence intervals, particularly for Poisson distributed data. This approach addressed the key shortcomings of traditional methods used to construct confidence intervals especially for cases where the number of observed events are low or zero. Traditional methods such as Gaussian approximation, which assumes that data follows a normal distribution which are used to calculate confidence intervals can often lead to incorrect interval particularly in rare event searches where the data is better described by a Poisson distribution. This can also lead to unphysical values e.g. negative value for rate of expected events. The Feldman-Cousins approach solves these problems by giving a unified method for constructing confidence intervals. The method ensures that the intervals are unbiased and do not favour one outcome over the other. It also ensures natural transition from two-sided intervals (where there is significant data) to one-sided upper limits (when there is little to no data). The method also respects physical constraints, such as non-negative value for expected event rates. It also provides intervals with more accurate coverage probabilities, reducing over-coverage issues common in other methods.

The Feldman & Cousins approach is implemented as a part of *gammapy* in python [228] which was used to get the interval for this analysis. The information was also verified with look-up tables in [227]. For a 90% confidence interval, in case of zero signal and background events, the upper and lower limits are given as $N_{up}^{90\%} = 2.44$ and $N_{low}^{90\%} = 0$ respectively. If one signal event is seen with zero background then this interval shifts to [4.36, 0.11]. It is important to note that both statistical and systematic uncertainties are not included for the intervals calculated in the Feldman & Cousins method.

6.4.2 Rolke approach

The Feldman & Cousins treatment is a frequentist method which requires the background source to be known precisely. Such a method can fail if the uncertainties are too high [229]. To solve this problem one can also use the Rolke method [230] which incorporates prior information in this case signal with a Poisson distribution and background with either a Poisson or Gaussian distribution. The method is implemented as a ROOT class under TRolke [231]. For a 90% confidence interval in the case of zero signal and background events the interval is given as [2.21, 0] assuming a Poisson distribution for both signal and background. As it is seen the interval is smaller in comparison to the Feldman & Cousins approach. This can be explained much more clearly for the case where there is one signal event and no background where the Rolke interval is [3.65, 0]. In this case according to the Feldman & Cousins approach the event has to be a signal since the lower limit is > 0 but

in the Rolke approach it is still possible that such an event in the signal region could be a background event i.e. in the Rolke approach the absence of background does not imply zero background, but it only means that the background is not too large. This is because background is treated as a Poisson number. Thus, the overall upper and lower limits in the Rolke approach are always smaller in comparison to the Feldman & Cousins method.

6.4.3 Conrad approach

The Conrad method for calculating confidence intervals allows the inclusion of systematic uncertainties in the evaluation. Using this approach the uncertainties in the background prediction, background detection and the signal detection efficiencies can be incorporated in the confidence interval calculation by integrating over the PDFs of these parameters [232]. The method computes the upper limit based on a likelihood ratio between the observed data and the null hypothesis(no signal). For this work the interval was calculated using POLE++ [233] which is a C++ program that implements the Conrad method. The systematic uncertainty on exposure was estimated to be as [] as mentioned in section 6.2. Using a uniform PDF to characterise the exposure and a Gaussian assumption for background, for a 90% confidence interval in the case of zero signal and background events the upper and lower limits are given as:

$$N_{up}^{90\%} = 2.39 N_{low}^{90\%} = 0 \quad (6.6)$$

The interval is smaller in comparison to the Feldman & Cousins method due to the uneven interval for the systematic uncertainty. For one signal event and zero background the interval changes to [].

6.4.4 Final calculation

After the determination of N_{up} using the Conrad approach the equation 6.5 can be solved to determine the upper limit to the diffused flux of $\text{UHE}\nu_s$. The integral goes from E_m in $= 10^{17.5}\text{eV}$ till $E_{max} = 10^{20.5}\text{eV}$ which is the total energy range explored in the simulations. It is also important to note that the limit is only valid for a smaller energy window. The single flavour 90% C.L. integrated limit is given by

$$k_{90} < 6.3 \times 10^{-17} \text{GeVcm}^{-2}\text{s}^{-1}\text{sr}^{-1}, \quad (6.7)$$

It applies to an energy range of $E_\nu \in [1.9 \times 10^{18} - 2.0 \times 10^{20}]$ which is the energy range for which $\sim 90\%$ total event rate is expected in the case of E_{nu}^{-2} flux. The value along with the 90% energy range is plotted as a solid line in fig ??.

The other lines in green are the *differential limits*. These are calculated by integrating the denominator of eq. 6.5 in bins of width $\Delta = 0.5\text{eV}$ in $\log_{10}(E_\nu)$. Mathematically for the i^{th} bin this can be represented as follows:

$$\text{Differential limit (i}^{\text{th}} E_\nu \text{ bin)} = \frac{N_{\text{Up}}}{\int_{\log_{10}(E^i - (\Delta \log_{10} E)/2)}^{\log_{10}(E^i + (\Delta \log_{10} E)/2)} E_\nu^{-1} \cdot \xi(E_\nu) \cdot \ln(10) \cdot d(\log_{10}(E_\nu))} \quad (6.8)$$

Assuming constant exposure and flux in each energy bin the differential limit can be estimated as:

$$\text{Approx. Differential limit (i}^{\text{th}} E_\nu \text{ bin)} = \frac{N_{\text{Up}}}{E_\nu^{-1} \cdot \xi(E_\nu) \cdot \ln(10) \cdot \Delta(\log_{10}(E_\nu))} \quad (6.9)$$

These limits provide a way to denote the sensitivity of the detector for different energies. As it can be seen from the fig. ?? for the Down-going Low analysis the Pierre Auger Observatory is the most sensitive for energies ~ 1 EeV.

Both limits are also compared to the results from the previous analysis in fig ?. As it was seen in the exposure comparison it is clear that the new triggers help improve the sensitivity at lower energies. For higher energies the improvements to the upper-limit for the diffuse flux of UHE_ν , though not as significant is still substantial. This improvement can be attributed to the changes in the Fisher analysis. The integral flux limit sees an improvement ~ 1 order of magnitude. The aim of this study was to evaluate the improvement, but it was always known that for this angular range significant improvements to the diffuse flux improvements were not expected. The diffuse flux limit and sensitivity for Auger is dominated by the Earth-skimming channel as shown in [18]. This limit is significantly lower than the DG_{low} channel and is the main driver to constrain astrophysical and cosmogenic models. However, the improvements shown in this analysis are more important in the context of point source searches. This is discussed more in the next chapter.

Source follow-up analysis

One of the most exciting fields of modern day neutrino astrophysics involves scanning the observable sky to look for neutrino sources. As mentioned in section 2.2.4 the observation of TXS 0506+056 [17] and NGC 1068 [16] which are examples of a transient source and a steady state of neutrinos has brought unprecedented excitement to the field. Any observation of a neutrino source offers a chance to significantly increase our overall knowledge about astroparticle physics. Since, Auger is one of the few experiments in the world sensitive to $\text{UHE}\nu_s$, any improvement in its point source sensitivity increases its capability for neutrino detection.

In this chapter, the point source sensitivity to ν events of the SD array is discussed for the zenith angular range explored in this thesis, DG_{low} . Based on the zero neutrino candidates found in the search performed in this work a source declination, δ dependent neutrino flux is calculated. This process includes calculating the declination dependent exposure and then converting it to a limit on the flux. The improvements to this exposure and sensitivity by the inclusion of new triggers is also discussed. Finally, the new limit is used to scan a few interesting sources which lie in the most sensitive range for the DG_{low} region.

7.1 Procedure for point source analysis

7.1.1 Source visibility

The field of view (FOV) of the Observatory and the corresponding neutrino efficiency is related to the zenith angle which in turn is related to the declination. For a given point-like source at declination δ and right ascension α (in equatorial coordinates), the time zenith angle which is the θ dependence at a certain time, t is given by:

$$\cos\theta(t) = \sin\lambda \sin\delta + \cos\lambda \cos\delta \sin(2\pi\frac{t}{T} - \alpha) \quad (7.1)$$

where T is the duration of one sidereal day and λ is the latitude of the observer ($\lambda = -35.2^\circ$ for Pierre Auger Observatory). Fig. ?? shows the FOV bands for different neutrino search channels (DG_{low}, DG_{high}, ES). These bands are plotted in equatorial coordinates as a function of $\alpha - t_{\text{GS}}$ where t_{GS} is the Greenwich Sidereal Time (GST) converted to for a mean longitude of the Observatory, l calculated as $t_{\text{GS}} = 2\pi t/T + l$. The sensitive declination ranges for different t_{GS} can be read from the plot which is very useful for real-time transient follow-up. For DG_{low} showers the SD of the Pierre Auger Observatory is sensitive to declinations between $\delta \sim -85^\circ - 40^\circ$. Another way to denote sky coverage for different neutrino searches at Auger is by calculating the time a source is visible to the Observatory for a particular declination. This is plotted in fig. ?? for all three search channels. As it can be seen from the plot all three channels are the most sensitive at two ends of their sensitive declination ranges (DG_{low} $\delta \sim -70^\circ, 35^\circ$) which is a consequence of smaller variation in zenith angle in time for certain directions. The sensitivity sharply decreases beyond these declination values. In the middle of these *two horns* is a plateau like region. It is also seen that generally the fraction of time a source is visible is comparable in the DG_{low} and DG_{high} range with both being higher in the ES range due to the size of the zenith angle windows. The fraction of visible time for vertical showers is also plotted. Even though this fraction of time is significantly high, currently no neutrino search is performed for this region as it is very difficult to differentiate between a cosmic ray and neutrino EAS for this zenith angle range.

7.1.2 Effective area and Exposure

Following this to calculate point source sensitivity, the declination dependent SD exposure is evaluated. This is done by first calculating an effective area to neutrinos of flavours i and energy E_ν is defined in the following way. For a point source spectral flux of flavour i given by $\phi_i(E_\nu) = \frac{d^4 N_\nu}{dE_\nu dA dt}$ the expected number of detected events is given by

$$\frac{dN_i}{dt} = \int_{E_{\text{min}}}^{E_{\text{max}}} dE_\nu \phi(E_\nu) \mathcal{A}_i(E_\nu) \quad (7.2)$$

The effective area is flavour dependent since for each flavour the shower development and the primary interaction ($c = \text{NC}, \text{CC}$) is substantially different. The effective area is for the DG_{low} region is given as follows:

$$\mathcal{A}_{i,j}(E_\nu, \theta(t), t) = \frac{\sigma^{i,c}(E_\nu)}{m_N} \int_X \varepsilon_{i,c}(E_\nu, \theta(t), t) A_{6T5} n_{\text{hex}}(t) dX \quad (7.3)$$

where $\varepsilon_{i,c}$ is the neutrino identification efficiency for a 6T5 unit. The declination dependence is taken into account by the $\theta(t)$ dependence of the efficiency. The effective area for electron neutrinos with CC interactions in km^2 for 2016 array and different theta is plotted in fig. ?. The effective area increases with increasing primary energy. It also increases with zenith angles till $\sim 70^\circ$ after which there is a slight decrease in the effective area which

is due to the decrease in neutrino sensitivity at higher zenith angles discussed earlier in section 5.5.5.

The exposure to point-like sources of UHE neutrinos can then be calculated by integrating the effective area for a given time interval and summing over the different flavours and channels as follows:

$$\xi(E_{\nu}, \delta) = \sum_{i,c} \int_t \mathcal{A}_{i,j}(E_{\nu}, \theta(t), t) dt \quad (7.4)$$

The exposure is δ dependent due to the dependence of effective area on $\theta(t)$. The effective area can also change with time due to the changes in the number of hexagons $n_{hex}(t)$. This change has been visualized for the DG_{low} channel for the time period of this search in fig. ???. As it can be seen in the plot the number is relatively stable especially in the period of one sidereal day apart from few outages which are removed from the searches. The directional exposure for the DGL channels for different fixed energies between 2014-2021 is shown in fig. ??. The solid line shows the exposure calculated in this study by including the new triggers while the dashed line shows the exposure calculated with the previous analysis for the same time period. Similar to the exposure calculated for the diffuse flux the exposure is significantly improved for lower energies with the improvement decreasing or vanishing for higher energies. The shape of the exposure is similar to the observation time plot in fig. ?? with the maximum exposure peaks seen at the same declinations. ES exposure published in [] is also plotted for comparison. It can be seen that generally the DG_{low} point source exposure is lower than that of ES except at higher energies where it is comparable. At these energies the different sensitive zenith angle ranges between the channels are the only differentiating factors for the exposure distribution.

7.2 Point-source neutrino flux limit

Since no neutrino candidate was discovered in the search window a point-source neutrino flux limit can be calculated. Similar to the calculation for the diffuse flux the number of expected neutrino events from a point like source at a given declination can be written as

$$N_{\text{expected}}(\delta) = \int_{E_{\min}}^{E_{\max}} \phi(E_{\nu}) \xi(E_{\nu}, \delta) dE_{\nu} \quad (7.5)$$

The point source flux is assumed to be independent of time and is assumed to be characterized as a power law, $\phi = k_{PS} E_{\nu}^{-2}$ for all declinations. The integrated upperlimit from each source can then be further calculated as follows:

$$k_{PS}^{90\%CL} = \frac{N_{Up}}{\int_{E_{\min}}^{E_{\max}} E_{\nu}^{-2} \xi(E_{\nu}, \delta) dE_{\nu}} \quad (7.6)$$

For this study initially a time period from 1 Jan 2014 till 31 December 2021 is selected.

The $N_{Up} = 2.39$ is calculated according to the Conrad approach as mentioned in section 6.4.3. The exposure is assumed to be uniform within $\pm 0.6\%$ for the time period of search as shown in [234].

The 90% C.L. declination dependent upper-limit for the DG_{low} channel is shown in fig. ?? . The limit is the stringent for the times the source is seen the longest. The limit is calculated for the energy range $\sim 2.0 \times 10^{18} \text{ eV} - \times 10^{20} \text{ eV}$. The dependence of energy intervals is minimal. This limit is also compared to the limit obtained from the previous analysis for the same time period in fig. ?? . As it can be seen the limit is significantly improved with new triggers fulfilling one of the primary objectives of this thesis. A cross-check of the diffuse limit is obtained from the point source analysis by performing double integration of the exposure, $\xi(E_\nu, \delta)$ in a similar way as done in [23].

The diffuse limit can be written as:

$$k_{PS}^{90\%CL} < \frac{N_{Up}}{\int_{\log_{10} E_{min}}^{\log_{10} E_{max}} \int_{-\pi/2}^{\pi/2} 2\pi \cdot \cos(\delta) \cdot E_\nu^{-1} \cdot \xi(E_\nu, \delta) \cdot \ln(10) \cdot d(\log_{10}(E_\nu)) \cdot d\delta} \quad (7.7)$$

The diffuse limit from point source analysis is given as:

$$k_{PS}^{90\%CL} < 2.0000 \times 10^{-8} \text{ GeV cm}^{-2} \text{ s}^{-1} \text{ sr}^{-1} \quad (7.8)$$

Which agrees with the value mentioned in eq. 6.7. It is also important to mention that even though the overall sensitive declination range for the DG_{low} analysis is small in comparison to other channels [11], the improvement presented in this thesis is still important as the sensitive declination ranges are not fully overlapping. Thus, if there is a point source at between declinations $\delta \in [-80^\circ - -68^\circ]$ then DG_{low} channel offers the only window at Auger to see $UHE\nu_s$ from such a source.

Conclusion and Outlook

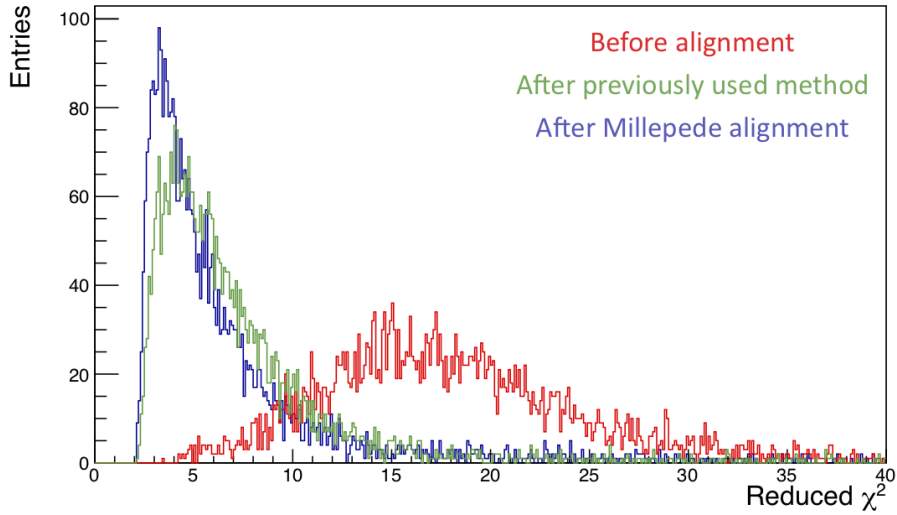


Figure 8.1: χ^2_{red} distribution for selected tracks showing the impact of Millepede alignment.

Besides detecting ultra-high-energy (UHE) cosmic rays, the Pierre Auger Observatory with its large Surface Detector (SD) array offers a remarkable exposure to neutrinos above 10^{17} eV. Any potential observation of such $\text{UHE}\nu_s$ will further our knowledge about the known universe. Since neutrinos are not deflected as they travel towards us at Earth, they offer a direct line of sight to the sources where they were produced. They are also some of the earliest particles produced in a transient source which makes their detection an important beacon for other astronomical instruments to perform a multi-messenger observation. The Pierre Auger Observatory is constantly monitoring the sky for the presence of such $\text{UHE}\nu_s$. The idea behind the detection remains the same as previous analysis at Auger where the neutrinos are assumed to induce Extensive Air Showers (EASs) close to the ground with

a large electro-magnetic component at ground ("young" showers). This strategy is only employed for horizontal showers ($\theta > 60^\circ$). Two new SD triggers, time-over-threshold-deconvolved (ToTd) and multiplicity of positive steps (MoPS) were installed in 2014 to further increase the detection efficiency/capability for low energy neutrino induced EASs. This thesis presents the first analysis of this improved efficiency for low energy neutrino showers in the zenith range $\theta \in [60^\circ, 75^\circ]$ also known as Down-going low or DG_{Low} range. In this thesis the effect of the new triggers is evaluated for two types of searches, the searches for the diffused flux of $UHE\nu_s$ and search for point-like sources of $UHE\nu_s$. For both searches an overall improvement of efficiency is observed when information from new triggers is incorporated in the analysis. A short summary of the three main contributions of this thesis along with an outlook detailing potential improvements are detailed in the next sections.

Incorporating new triggers in the DG_{Low} $UHE\nu_s$ searches

During this thesis each facet of the DG_{Low} analysis was analysed. An effort was made to maximise the potential of the analysis. A blind search strategy similar to [18, 23] was followed to avoid any bias in the analysis. The first step in this process was to include the information from the new triggers in the neutrino searches. About ~ 7 years of recorded data was available for this task. The effect of the new triggers was first evaluated on neutrino simulations by including them in the analysis chain as described in section 5.5.3. By the inclusion of new triggers an overall increase in reconstructed events was observed as shown in fig ???. This increase was most significant for lower energy neutrinos and decreased with increase in primary energy. This was an expected consequence due to the design of the new triggers. The overall increase also allowed for further modifications to the analysis which included lowering some stringent cuts as described in section 5.5.5. For the final step of the analysis a Fisher discriminate polynomial was built and trained using the simulations (signal sample) and a small fraction of recorded data, $\sim 20\%$ from the Observatory (background sample). The polynomial is built with Area over Peaks (AoPs) of the stations and a differentiation between the background and signal is performed based on a cut on the Fisher value as given in eq. 5.8. After the fixing the selection, a test sample was unblinded to catch any remaining flaws in the analysis. This proved worthwhile as a small error in the reconstruction was discovered during this process. The error was promptly corrected, and the whole selection procedure was re-evaluated, and the Fisher was retrained. Due to this change the partially unblinded test sample to be blinded again. After the correction the unblinding was again performed in two stages. The new test sample and the full blinded sample, $20\% + 60\%$ of recorded data between the period of 1 Jan 2014 to 31 December 2012 was analysed to search for neutrinos. No neutrino candidates were found in the search performed using the analysis described in this thesis.

Outlook

Even though a concerted effort was made to maximise the potential of the analysis presented in this thesis certain improvements could not be implemented and are thus summarized here for future studies. The segmentation algorithm used for reconstruction of events for neutrino searches was found to be not properly tuned for the new triggers, ToTd and MoPS. Thus, for this analysis the new triggers were completely removed from the segmentation algorithm. The primary purpose of the segmentation algorithm is to evaluate the correct start times for the WCD signals to decrease the effect of accidental muons which in turn affects the zenith angle estimation. A better tuned segmentation algorithm could thus further improve the neutrino search with new triggers. Some examples of events where the segmentation algorithm could help are presented in Appendix ???. This tuning could not be explored in this thesis but could be implemented in the future. In this thesis a cut on the saturated and active PMTs was also explored but not implemented in the final analysis. A detailed study on such a cut could also be useful to increase the efficiency of the analysis.

Improvements to the diffuse flux limit for $\text{UHE}\nu_s$ with new triggers

With no neutrino candidate detected a 90% C.L. upper limit on the diffuse flux of $\text{UHE}\nu_s$ for the DG_{low} channel was evaluated. The limit was evaluated under the assumption of a diffuse flux given by $\phi \propto E_\nu^{-2}$ with a 1:1:1 neutrino flavour ratio at earth. The integrated limit is given as:

$$k_{90} < 6.3 \times 10^{-17} \text{ GeV cm}^{-2} \text{ s}^{-1} \text{ sr}^{-1}, \quad (8.1)$$

in the energy range $E_\nu \in [1.9 \times 10^{18} - 2.0 \times 10^{20}] \text{ eV}$. The integrated limit represents the value of the normalisation of the differential flux needed to predict ~ 2.39 expected events. The number 2.39 was evaluated using a semi Bayesian extension of the Feldman & Cousins treatment accounting for systematic uncertainties on exposure [232]. This limit is one order stricter than the one obtained without the new triggers for the same time period. Even though this improvement is significant

Correct this
and the limit

Improvements to the point source searches for $\text{UHE}\nu_s$ with new triggers

Further a point sensitivity comparison was also performed to evaluate the performance of the new triggers. The methodology was adopted from [11] and an energy and declination dependent exposure was evaluated for the DG_{low} range. Using the no neutrino candidate detection ansatz a 90% C.L. upper limit on the neutrino flux from point-like sources as a function of source declination, δ was evaluated and presented in fig. ???. This limit was also

shown to improve with the inclusion of new triggers in fig. ???. The improvement though small has an impact in the overall sensitivity since the different searches (DG_{low} , DG_{high} , ES) have different FOVs. It must also be stressed that Auger is one of the constantly running experiments sensitive to Energy ranges $> 10^{18}$ eV thus any improvement to its sensitivity is an important step for the potential future detection of $UHE\nu_s$.

Bibliography

- [1] T. Wulf, *Beobachtungen über die Strahlung hoher Durchdringungsfähigkeit auf dem Eiffelturm*, Phys. Z. **11** 811–813.
- [2] V. F. Hess, *Über Beobachtungen der durchdringenden Strahlung bei sieben Freiballonfahrten*, Phys. Z. **13** (1912) 1084–1091.
- [3] J. Clay, *Penetrating radiation*, Acad. Amsterdam Proc. **30** (1927) 1115–1127.
- [4] J. Clay, *Penetrating radiation II*, Acad. Amsterdam Proc. **31** (1928) 1091–1097.
- [5] B. Rossi, *Über die Eigenschaften der durchdringenden Korpuskularstrahlung im Meeresniveau*, Zeitschrift für Physik **82** no. 3, (1933) 151–178.
- [6] K. Schmeiser and W. Bothe, *Die harten ultrastrahlschauer*, Annalen der Physik **424** no. 1-2, (1938) 161–177.
- [7] P. Auger, P. Ehrenfest, R. Maze, J. Daudin, and R. A. Fréon, *Extensive Cosmic-Ray Showers*, Rev. Mod. Phys. **11** (1939) 288–291,
<https://link.aps.org/doi/10.1103/RevModPhys.11.288>.
- [8] Nuclear Instruments and Methods in Physics Research Section A: Accelerators, Spectrometers, Detectors and Associated Equipment **798** (2015) 172–213,
<http://dx.doi.org/10.1016/j.nima.2015.06.058>.
- [9] R. Mussa, A. Vasquez, and for the Pierre Auger Collaboration, *Classification and Reconstruction of single and multiple ELVES in AUGER*, Journal of Physics: Conference Series **2398** no. 1, (2022) 012006,
<https://dx.doi.org/10.1088/1742-6596/2398/1/012006>.
- [10] P. Abreu, M. Aglietta, et al., *Limits to Gauge Coupling in the Dark Sector Set by the Nonobservation of Instanton-Induced Decay of Super-Heavy Dark Matter in the Pierre Auger Observatory Data*, Physical Review Letters **130** no. 6, (2023),
<http://dx.doi.org/10.1103/PhysRevLett.130.061001>.
- [11] A. Aab et al., *Limits on point-like sources of ultra-high-energy neutrinos with the Pierre Auger Observatory*, Journal of Cosmology and Astroparticle Physics **2019** no. 11, (2019) 004–004,
<http://dx.doi.org/10.1088/1475-7516/2019/11/004>.

- [12] *Searches for Ultra-High-Energy Photons at the Pierre Auger Observatory*, Universe **8** no. 11, (2022) 579, <http://dx.doi.org/10.3390/universe8110579>.
- [13] T. Bister, G. R. Farrar, and M. Unger, *The large-scale anisotropy and flux (de-)magnification of ultra-high-energy cosmic rays in the Galactic magnetic field*, 2024. <https://arxiv.org/abs/2408.00614>.
- [14] D. Allard, *Extragalactic propagation of ultrahigh energy cosmic-rays*, Astroparticle Physics **39-40** (2012) 33–43, <https://www.sciencedirect.com/science/article/pii/S092765051100199X>, Cosmic Rays Topical Issue.
- [15] P. A. The IceCube and T. A. collaborations, *Search for correlations between the arrival directions of IceCube neutrino events and ultrahigh-energy cosmic rays detected by the Pierre Auger Observatory and the Telescope Array*, Journal of Cosmology and Astroparticle Physics **2016** no. 01, (2016) 037, <https://dx.doi.org/10.1088/1475-7516/2016/01/037>.
- [16] R. Abbasi and others for IceCube Collaboration, *Evidence for neutrino emission from the nearby active galaxy NGC 1068*, Science **378** no. 6619, (2022) 538–543, <http://dx.doi.org/10.1126/science.abg3395>.
- [17] I. Collaboration, *Neutrino emission from the direction of the blazar TXS 0506+056 prior to the IceCube-170922A alert*, Science **361** no. 6398, (2018) 147–151, <https://www.science.org/doi/pdf/10.1126/science.aat2890>, <https://www.science.org/doi/abs/10.1126/science.aat2890>.
- [18] Pierre Auger Collaboration Collaboration, A. Aab et al., *Probing the origin of ultra-high-energy cosmic rays with neutrinos in the EeV energy range using the Pierre Auger Observatory*, Journal of Cosmology and Astroparticle Physics **2019** no. 10, (2019) 022–022, <http://dx.doi.org/10.1088/1475-7516/2019/10/022>.
- [19] LIGO Scientific Collaboration and Virgo Collaboration Collaboration, B. P. Abbott et al., *Observation of Gravitational Waves from a Binary Black Hole Merger*, Phys. Rev. Lett. **116** (2016) 061102, <https://link.aps.org/doi/10.1103/PhysRevLett.116.061102>.
- [20] LIGO Scientific Collaboration, Virgo Collaboration, Fermi GBM, INTEGRAL, IceCube Collaboration, AstroSat Cadmium Zinc Telluride Imager Team, IPN Collaboration, The Insight-Hxmt Collaboration, ANTARES Collaboration, The Swift Collaboration, AGILE Team, The 1M2H Team, The Dark Energy Camera GW-EM Collaboration, the DES Collaboration, The DLT40 Collaboration, GRAWITA: GRAVitational Wave Inaf TeAm, The Fermi Large Area Telescope Collaboration, ATCA: Australia Telescope Compact Array, ASKAP: Australian SKA Pathfinder, Las

- Cumbres Observatory Group, OzGrav, DWF (Deeper, Wider, Faster Program), AST3, CAASTRO Collaborations, The VINROUGE Collaboration, MASTER Collaboration, J-GEM, GROWTH, JAGWAR, Caltech- NAO, TTU-NRAO, NuSTAR Collaborations, Pan-STARRS, The MAXI Team, TZAC Consortium, KU Collaboration, Nordic Optical Telescope, ePESSTO, GROND, Texas Tech University, SALT Group, TOROS: Transient Robotic Observatory of the South Collaboration, The BOOTES Collaboration, MWA: Murchison Widefield Array, The CALET Collaboration, IKI-GW Follow-up Collaboration, H.E.S.S. Collaboration, LOFAR Collaboration, LWA: Long Wavelength Array, HAWC Collaboration, The Pierre Auger Collaboration, ALMA Collaboration, Euro VLBI Team, Pi of the Sky Collaboration, The Chandra Team at McGill University, DFN: Desert Fireball Network, ATLAS, High Time Resolution Universe Survey, RIMAS, RATIR, SKA South Africa/MeerKAT Collaboration, B. P. Abbott et al., *Multi-messenger Observations of a Binary Neutron Star Merger**, The Astrophysical Journal Letters **848** no. 2, (2017) L12, <http://dx.doi.org/10.3847/2041-8213/aa91c9>.
- [21] IceCube, Fermi-LAT, MAGIC, AGILE, ASAS-SN, HAWC, H.E.S.S., INTEGRAL, Kanata, Kiso, Kapteyn, Liverpool Telescope, Subaru, Swift NuSTAR, VERITAS, VLA/17B-403 Collaboration, M. G. Aartsen et al., *Multimessenger observations of a flaring blazar coincident with high-energy neutrino IceCube-170922A*, Science **361** no. 6398, (2018) eaat1378, [arXiv:1807.08816](https://arxiv.org/abs/1807.08816) [astro-ph.HE].
- [22] IceCube Collaboration, R. Abbasi et al., *Observation of high-energy neutrinos from the Galactic plane*, Science **380** no. 6652, (2023) adc9818, [arXiv:2307.04427](https://arxiv.org/abs/2307.04427) [astro-ph.HE].
- [23] J. L. Navarro Quirante, *Search for ultra-high energy neutrinos at the Pierre Auger Observatory*, 2013. <http://hdl.handle.net/10481/26377>.
- [24] V. Hess, *On the Observations of the Penetrating Radiation during Seven Balloon Flights*, 2018. <https://arxiv.org/abs/1808.02927>.
- [25] B. Rossi, *On the Magnetic Deflection of Cosmic Rays*, Phys. Rev. **36** (1930) 606–606, <https://link.aps.org/doi/10.1103/PhysRev.36.606>.
- [26] T. H. Johnson, *The Azimuthal Asymmetry of the Cosmic Radiation*, Phys. Rev. **43** (1933) 834–835, <https://link.aps.org/doi/10.1103/PhysRev.43.834>.
- [27] L. Alvarez and A. H. Compton, *A Positively Charged Component of Cosmic Rays*, Phys. Rev. **43** (1933) 835–836, <https://link.aps.org/doi/10.1103/PhysRev.43.835>.
- [28] Telescope Array Collaboration, R. U. Abbasi et al., *An extremely energetic cosmic ray observed by a surface detector array*, Science **382** no. 6673, (2023) abo5095, [arXiv:2311.14231](https://arxiv.org/abs/2311.14231) [astro-ph.HE].

- [29] A. M. Hillas, *The Origin of Ultra-High-Energy Cosmic Rays*, Annual Review of Astronomy and Astrophysics **22** (1984) 425–444.
- [30] R. D. Blandford, *Acceleration of Ultra High Energy Cosmic Rays*, Physica Scripta **2000** no. T85, (2000) 191,
<https://dx.doi.org/10.1238/Physica.Topical.085a00191>.
- [31] J. P. Rachen and P. L. Biermann, *Extragalactic ultra-high energy cosmic rays. I. Contribution from hot spots in FR-II radio galaxies.*, Astronomy and Astrophysics **272** (1993) 161–175, arXiv:astro-ph/9301010 [astro-ph].
- [32] P. Bhattacharjee and G. Sigl, *Origin and propagation of extremely high-energy cosmic rays*, Physics Reports **327** no. 3–4, (2000) 109–247,
[http://dx.doi.org/10.1016/S0370-1573\(99\)00101-5](http://dx.doi.org/10.1016/S0370-1573(99)00101-5).
- [33] N. Busca, D. Hooper, and E. W. Kolb, *Pierre Auger data, photons, and top-down cosmic ray models*, Physical Review D **73** no. 12, (2006),
<http://dx.doi.org/10.1103/PhysRevD.73.123001>.
- [34] E. Fermi, *On the Origin of the Cosmic Radiation*, Phys. Rev. **75** (1949) 1169–1174,
<https://link.aps.org/doi/10.1103/PhysRev.75.1169>.
- [35] P. BLASI, *COSMIC RAY ACCELERATION IN SUPERNOVA REMNANTS*,
http://dx.doi.org/10.1142/9789814329033_0061.
- [36] F. M. Rieger, *Active Galactic Nuclei as Potential Sources of Ultra-High Energy Cosmic Rays*, Universe **8** no. 11, (2022) 607,
<http://dx.doi.org/10.3390/universe8110607>.
- [37] K. Kotera, *Ultrahigh energy cosmic ray acceleration in newly born magnetars and their associated gravitational wave signatures*, Phys. Rev. D **84** (2011) 023002,
<https://link.aps.org/doi/10.1103/PhysRevD.84.023002>.
- [38] B. Cerutti and G. Giacinti, *A global model of particle acceleration at pulsar wind termination shocks*, Astronomy & Astrophysics **642** (2020) A123,
<http://dx.doi.org/10.1051/0004-6361/202038883>.
- [39] K. Murase, S. Inoue, and S. Nagataki, *Cosmic Rays above the Second Knee from Clusters of Galaxies and Associated High-Energy Neutrino Emission*, The Astrophysical Journal **689** no. 2, (2008) L105,
<https://dx.doi.org/10.1086/595882>.
- [40] A. Condorelli, J. Biteau, and R. Adam, *Impact of Galaxy Clusters on the Propagation of Ultrahigh-energy Cosmic Rays*, The Astrophysical Journal **957** no. 2, (2023) 80,
<https://dx.doi.org/10.3847/1538-4357/acfeef>.

-
- [41] J. G. Kirk, A. W. Guthmann, Y. A. Gallant, and A. Achterberg, *Particle Acceleration at Ultrarelativistic Shocks: An Eigenfunction Method*, The Astrophysical Journal **542** no. 1, (2000) 235, <https://dx.doi.org/10.1086/309533>.
- [42] A. Achterberg, Y. A. Gallant, J. G. Kirk, and A. W. Guthmann, *Particle acceleration by ultrarelativistic shocks: theory and simulations*, Monthly Notices of the Royal Astronomical Society **328** no. 2, (2001) 393–408, <https://academic.oup.com/mnras/article-pdf/328/2/393/3784816/328-2-393.pdf>, <https://doi.org/10.1046/j.1365-8711.2001.04851.x>.
- [43] R. Aloisio and F. Tortorici, *Super heavy dark matter and UHECR anisotropy at low energy*, Astroparticle Physics **29** no. 5, (2008) 307–316, <https://www.sciencedirect.com/science/article/pii/S0927650508000285>.
- [44] L. Marzola and F. R. Urban, *Ultra High Energy Cosmic Rays & Super-heavy Dark Matter: Observables and prospect of (non)detection*, Astroparticle Physics **93** (2017) 56–69, <https://www.sciencedirect.com/science/article/pii/S0927650516301931>.
- [45] P. Bhattacharjee and G. Sigl, *Origin and propagation of extremely high-energy cosmic rays*, Physics Reports **327** no. 3, (2000) 109–247, <https://www.sciencedirect.com/science/article/pii/S0370157399001015>.
- [46] V. Berezhinsky, B. Hnatyk, and A. Vilenkin, *Gamma ray bursts from superconducting cosmic strings*, Phys. Rev. D **64** (2001) 043004, <https://link.aps.org/doi/10.1103/PhysRevD.64.043004>.
- [47] V. Berezhinsky and A. Vilenkin, *Cosmic Necklaces and Ultrahigh Energy Cosmic Rays*, Phys. Rev. Lett. **79** (1997) 5202–5205, <https://link.aps.org/doi/10.1103/PhysRevLett.79.5202>.
- [48] K. Greisen, *End to the Cosmic-Ray Spectrum?*, Phys. Rev. Lett. **16** (1966) 748–750, <https://link.aps.org/doi/10.1103/PhysRevLett.16.748>.
- [49] G. T. Zatsepin and V. A. Kuzmin, *Upper limit of the spectrum of cosmic rays*, JETP Lett. **4** (1966) 78–80.
- [50] K.-H. Kampert and P. Tinyakov, *Cosmic rays from the ankle to the cutoff*, Comptes Rendus Physique **15** no. 4, (2014) 318–328, <https://www.sciencedirect.com/science/article/pii/S1631070514000541>, Ultra-high-energy cosmic rays: From the ankle to the tip of the spectrum.
- [51] H. Kawai, S. Yoshida, H. Yoshii, K. Tanaka, F. Cohen, M. Fukushima, N. Hayashida, K. Hiyama, D. Ikeda, E. Kido, et al., *Telescope array experiment*, Nuclear Physics B-Proceedings Supplements **175** no. SUPPL.: COMPLETE, (2008) 221–226.

- [52] AMS Collaboration, M. Aguilar et al., *First Result from the Alpha Magnetic Spectrometer on the International Space Station: Precision Measurement of the Positron Fraction in Primary Cosmic Rays of 0.5–350 GeV*, Phys. Rev. Lett. **110** (2013) 141102.
- [53] KASCADE Collaboration, G. Schatz et al., *The KASCADE experiment*, Nucl. Phys. B Proc. Suppl. **60** (1998) 151–160.
- [54] Pierre Auger Collaboration, A. Aab et al., *Inferences on mass composition and tests of hadronic interactions from 0.3 to 100 EeV using the water-Cherenkov detectors of the Pierre Auger Observatory*, Phys. Rev. D **96** no. 12, (2017) 122003, arXiv:1710.07249 [astro-ph.HE].
- [55] Pierre Auger Collaboration, A. Aab et al., *Combined fit of spectrum and composition data as measured by the Pierre Auger Observatory*, JCAP **04** (2017) 038, arXiv:1612.07155 [astro-ph.HE], [Erratum: JCAP 03, E02 (2018)].
- [56] G. A. Anastasi, *AugerPrime: The Pierre Auger Observatory upgrade*, Nuclear Instruments and Methods in Physics Research Section A: Accelerators, Spectrometers, Detectors and Associated Equipment **1044** (2022) 167497, <https://www.sciencedirect.com/science/article/pii/S0168900222007896>.
- [57] A. Arámburo-García, K. Bondarenko, A. Boyarsky, D. Nelson, A. Pillepich, and A. Sokolenko, *Ultrahigh energy cosmic ray deflection by the intergalactic magnetic field*, Physical Review D **104** no. 8, (2021), <http://dx.doi.org/10.1103/PhysRevD.104.083017>.
- [58] C. Bonifazi, *The angular resolution of the Pierre Auger Observatory*, Nuclear Physics B - Proceedings Supplements **190** (2009) 20–25, <https://www.sciencedirect.com/science/article/pii/S0920563209003028>, Proceedings of the Cosmic Ray International Seminars.
- [59] Pierre Auger Collaboration, P. Abreu et al., *Arrival Directions of Cosmic Rays above 32 EeV from Phase One of the Pierre Auger Observatory*, Astrophys. J. **935** no. 2, (2022) 170, arXiv:2206.13492 [astro-ph.HE].
- [60] Pierre Auger Collaboration, A. Aab et al., *Cosmic-ray anisotropies in right ascension measured by the Pierre Auger Observatory*, Astrophys. J. **891** (2020) 142, arXiv:2002.06172 [astro-ph.HE].
- [61] Telescope Array, Pierre Auger Collaboration, A. di Matteo et al., *UHECR arrival directions in the latest data from the original Auger and TA surface detectors and nearby galaxies*, PoS ICRC2021 (2021) 308, arXiv:2111.12366 [astro-ph.HE].

-
- [62] Particle Data Group Collaboration, S. Navas et al., *Review of particle physics*, Phys. Rev. D **110** no. 3, (2024) 030001.
- [63] Pierre Auger Collaboration, A. Abdul Halim et al., *Search for evidence of neutron fluxes using Pierre Auger Observatory data*, PoS **ICRC2023** (2023) 246.
- [64] G. Pühlhofer, F. Leuschner, and H. Salzmänn, *H.E.S.S.: The High Energy Stereoscopic System*, arXiv:2405.11104 [astro-ph.IM].
- [65] D. J. Thompson and C. A. Wilson-Hodge, *Fermi Gamma-Ray Space Telescope*, http://dx.doi.org/10.1007/978-981-16-4544-0_58-1.
- [66] *Science with the Cherenkov Telescope Array*. WORLD SCIENTIFIC, Feb., 2018. <http://dx.doi.org/10.1142/10986>.
- [67] T. P. A. Collaboration, *Searches for Ultra-High-Energy Photons at the Pierre Auger Observatory*, Universe **8** no. 11, (2022), <https://www.mdpi.com/2218-1997/8/11/579>.
- [68] L. M. Brown, *The idea of the neutrino*, Physics Today **31** no. 9, (1978) 23–28, https://pubs.aip.org/physicstoday/article-pdf/31/9/23/8285438/23_1_online.pdf, <https://doi.org/10.1063/1.2995181>.
- [69] F. Reines and C. L. Cowan, *Detection of the Free Neutrino*, Phys. Rev. **92** (1953) 830–831, <https://link.aps.org/doi/10.1103/PhysRev.92.830>.
- [70] Super-Kamiokande Collaboration, Y. Fukuda et al., *Evidence for oscillation of atmospheric neutrinos*, Phys. Rev. Lett. **81** (1998) 1562–1567, arXiv:hep-ex/9807003.
- [71] A. Bellerive, J. Klein, A. McDonald, A. Noble, and A. Poon, *The Sudbury Neutrino Observatory*, Nuclear Physics B **908** (2016) 30–51, <https://www.sciencedirect.com/science/article/pii/S0550321316300736>, Neutrino Oscillations: Celebrating the Nobel Prize in Physics 2015.
- [72] X. Qian and P. Vogel, *Neutrino mass hierarchy*, Progress in Particle and Nuclear Physics **83** (2015) 1–30, <http://dx.doi.org/10.1016/j.pnpnp.2015.05.002>.
- [73] Katrin Collaboration, M. Aker et al., *Direct neutrino-mass measurement based on 259 days of KATRIN data*, arXiv:2406.13516 [nucl-ex].
- [74] A. de Gouvêa, *Neutrino mass puzzle*, <https://cerncourier.com/a/the-neutrino-mass-puzzle/#:~:text=Though%20there%20are%20too%20many,or%20through%20a%20different%20mechanism>.

- [75] Kamiokande-II Collaboration, K. Hirata et al., *Observation of a Neutrino Burst from the Supernova SN 1987a*, Phys. Rev. Lett. **58** (1987) 1490–1493.
- [76] IceCube Collaboration, M. G. Aartsen et al., *First observation of PeV-energy neutrinos with IceCube*, Phys. Rev. Lett. **111** (2013) 021103, arXiv:1304.5356 [astro-ph.HE].
- [77] I. Collaboration*, *Evidence for High-Energy Extraterrestrial Neutrinos at the IceCube Detector*, Science **342** no. 6161, (2013) 1242856,
<https://www.science.org/doi/pdf/10.1126/science.1242856>,
<https://www.science.org/doi/abs/10.1126/science.1242856>.
- [78] (IceCube Collaboration)*, IceCube Collaboration, R. Abbasi et al., *Measurement of atmospheric neutrino mixing with improved IceCube DeepCore calibration and data processing*, Phys. Rev. D **108** no. 1, (2023) 012014, arXiv:2304.12236 [hep-ex].
- [79] M. Prado Rodriguez, *Neutrino Mass Ordering with IceCube DeepCore*, Physical Sciences Forum **8** no. 1, (2023), <https://www.mdpi.com/2673-9984/8/1/7>.
- [80] D. Scott, *The Cosmic Neutrino Background*, 2024.
<https://arxiv.org/abs/2402.16243>.
- [81] B. Pontecorvo, *Inverse beta processes and nonconservation of lepton charge*, Zh. Eksp. Teor. Fiz. **34** (1957) 247.
- [82] Z. Maki, M. Nakagawa, and S. Sakata, *Remarks on the Unified Model of Elementary Particles*, Progress of Theoretical Physics **28** no. 5, (1962) 870–880,
<https://academic.oup.com/ptp/article-pdf/28/5/870/5258750/28-5-870.pdf>,
<https://doi.org/10.1143/PTP.28.870>.
- [83] P. Lipari, M. Lusignoli, and D. Meloni, *Flavor composition and energy spectrum of astrophysical neutrinos*, Physical Review D **75** no. 12, (2007),
<http://dx.doi.org/10.1103/PhysRevD.75.123005>.
- [84] IceCube Collaboration, R. Abbasi et al., *Characterization of the astrophysical diffuse neutrino flux using starting track events in IceCube*, Phys. Rev. D **110** no. 2, (2024) 022001, arXiv:2402.18026 [astro-ph.HE].
- [85] IceCube Collaboration, R. Abbasi et al., *Constraining High-energy Neutrino Emission from Supernovae with IceCube*, Astrophys. J. Lett. **949** no. 1, (2023) L12,
arXiv:2303.03316 [astro-ph.HE].
- [86] A. Condorelli, D. Boncioli, E. Peretti, and S. Petrera, *Testing hadronic and photohadronic interactions as responsible for ultrahigh energy cosmic rays and neutrino fluxes from starburst galaxies*, Physical Review D **107** no. 8, (2023),
<http://dx.doi.org/10.1103/PhysRevD.107.083009>.

-
- [87] K. Murase and F. W. Stecker, *High-Energy Neutrinos from Active Galactic Nuclei*, http://dx.doi.org/10.1142/9789811282645_0010.
- [88] B. Zhang, Z. G. Dai, P. Mészáros, E. Waxman, and A. K. Harding, *High-Energy Neutrinos from Magnetars*, *The Astrophysical Journal* **595** no. 1, (2003) 346–351, [arXiv:astro-ph/0210382](https://arxiv.org/abs/astro-ph/0210382) [astro-ph].
- [89] V. S. Berezinsky and G. T. Zatsepin, *Cosmic neutrinos of superhigh energy*, *Yad. Fiz.* **11** (1970) 200–205.
- [90] D. Ehler, A. van Vliet, F. Oikonomou, and W. Winter, *Constraints on the proton fraction of cosmic rays at the highest energies and the consequences for cosmogenic neutrinos and photons*, *Journal of Cosmology and Astroparticle Physics* **2024** no. 02, (2024) 022, <https://dx.doi.org/10.1088/1475-7516/2024/02/022>.
- [91] R. Aloisio, D. Boncioli, A. di Matteo, A. Grillo, S. Petrera, and F. Salamida, *Cosmogenic neutrinos and ultra-high energy cosmic ray models*, *Journal of Cosmology and Astroparticle Physics* **2015** no. 10, (2015) 006, <https://dx.doi.org/10.1088/1475-7516/2015/10/006>.
- [92] K.-H. Kampert and M. Unger, *Measurements of the cosmic ray composition with air shower experiments*, *Astroparticle Physics* **35** no. 10, (2012) 660–678, <https://www.sciencedirect.com/science/article/pii/S0927650512000382>.
- [93] R. Alves Batista, R. M. de Almeida, B. Lago, and K. Kotera, *Cosmogenic photon and neutrino fluxes in the Auger era*, *JCAP* **01** (2019) 002, [arXiv:1806.10879](https://arxiv.org/abs/1806.10879) [astro-ph.HE].
- [94] Z. Myers and A. Nusser, *Searching for neutrinos from WIMP annihilations in the Galactic stellar disc*, *Monthly Notices of the Royal Astronomical Society* **387** no. 4, (2008) 1712–1718, <https://academic.oup.com/mnras/article-pdf/387/4/1712/3818137/mnras0387-1712.pdf>, <https://doi.org/10.1111/j.1365-2966.2008.13366.x>.
- [95] C. A. Argüelles, D. Delgado, A. Friedlander, A. Kheirandish, I. Safa, A. C. Vincent, and H. White, *Dark matter decay to neutrinos*, *Phys. Rev. D* **108** (2023) 123021, <https://link.aps.org/doi/10.1103/PhysRevD.108.123021>.
- [96] J. A. Formaggio and G. P. Zeller, *From eV to EeV: Neutrino cross sections across energy scales*, *Reviews of Modern Physics* **84** no. 3, (2012) 1307–1341, <http://dx.doi.org/10.1103/RevModPhys.84.1307>.
- [97] S. L. Glashow, *Resonant Scattering of Antineutrinos*, *Phys. Rev.* **118** (1960) 316–317, <https://link.aps.org/doi/10.1103/PhysRev.118.316>.

- [98] IceCube Collaboration, M. G. Aartsen et al., *Detection of a particle shower at the Glashow resonance with IceCube*, Nature **591** no. 7849, (2021) 220–224, [arXiv:2110.15051 \[hep-ex\]](#), [Erratum: Nature 592, E11 (2021)].
- [99] A. Garcia-Soto, D. Garg, M. H. Reno, and C. A. Argüelles, *Probing quantum gravity with elastic interactions of ultrahigh-energy neutrinos*, Phys. Rev. D **107** (2023) 033009, <https://link.aps.org/doi/10.1103/PhysRevD.107.033009>.
- [100] A. Cooper-Sarkar, P. Mertsch, and S. Sarkar, *The high energy neutrino cross-section in the Standard Model and its uncertainty*, Journal of High Energy Physics **2011** no. 8, (2011), [http://dx.doi.org/10.1007/JHEP08\(2011\)042](http://dx.doi.org/10.1007/JHEP08(2011)042).
- [101] F. D. Aaron, H. Abramowicz, I. Abt, L. Adamczyk, M. Adamus, A.-d. Martin, C. Alexa, V. Andreev, S. Antonelli, P. Antonioli, et al., *Combined measurement and QCD analysis of the inclusive $e\pm p$ scattering cross sections at HERA*, Journal of High Energy Physics **2010** no. 1, (2010) 1–63.
- [102] G. Altarelli and G. Parisi, *Asymptotic freedom in parton language*, Nuclear Physics B **126** no. 2, (1977) 298–318, <https://www.sciencedirect.com/science/article/pii/0550321377903844>.
- [103] Y. L. Dokshitzer, *Calculation of the Structure Functions for Deep Inelastic Scattering and $e^+ e^-$ Annihilation by Perturbation Theory in Quantum Chromodynamics.*, Sov. Phys. JETP **46** (1977) 641–653.
- [104] V. N. Gribov and L. N. Lipatov, *Deep inelastic ep scattering in perturbation theory*, Sov. J. Nucl. Phys. **15** no. 4, (1972) 438–450, <https://cds.cern.ch/record/427157>.
- [105] IceCube Collaboration, M. G. Aartsen et al., *The IceCube Neutrino Observatory: Instrumentation and Online Systems*, JINST **12** no. 03, (2017) P03012, [arXiv:1612.05093 \[astro-ph.IM\]](#), [Erratum: JINST 19, E05001 (2024)].
- [106] E. Andres et al., *The AMANDA neutrino telescope: Principle of operation and first results*, Astropart. Phys. **13** (2000) 1–20, [arXiv:astro-ph/9906203](#).
- [107] K. Arisaka et al., *KAMIOKA Nucleon Decay Experiments; status and performance*, AIP Conf. Proc. **114** (1984) 54–76.
- [108] A. Creusot, *The Antares detector*, Nuclear Instruments and Methods in Physics Research Section A: Accelerators, Spectrometers, Detectors and Associated Equipment **718** (2013) 489–491, <https://www.sciencedirect.com/science/article/pii/S0168900212014088>, Proceedings of the 12th Pisa Meeting on Advanced Detectors.

-
- [109] A. Margiotta, *The KM3NeT deep-sea neutrino telescope*, Nuclear Instruments and Methods in Physics Research Section A: Accelerators, Spectrometers, Detectors and Associated Equipment **766** (2014) 83–87, <https://www.sciencedirect.com/science/article/pii/S0168900214006433>, RICH2013 Proceedings of the Eighth International Workshop on Ring Imaging Cherenkov Detectors Shonan, Kanagawa, Japan, December 2-6, 2013.
- [110] Y. Malyskin, *Baikal-GVD neutrino telescope: Design reference 2022*, Nuclear Instruments and Methods in Physics Research Section A: Accelerators, Spectrometers, Detectors and Associated Equipment **1050** (2023) 168117, <https://www.sciencedirect.com/science/article/pii/S0168900223001079>.
- [111] P-ONE Collaboration, M. Agostini et al., *The Pacific Ocean Neutrino Experiment*, Nature Astron. **4** no. 10, (2020) 913–915, [arXiv:2005.09493](https://arxiv.org/abs/2005.09493) [astro-ph.HE].
- [112] G. A. Askar'yan, *Excess negative charge of an electron-photon shower and its coherent radio emission*, Zh. Eksp. Teor. Fiz. **41** (1961) 616–618.
- [113] J. Alvarez-Muñiz, A. Romero-Wolf, and E. Zas, *Practical and accurate calculations of Askaryan radiation*, Phys. Rev. D **84** (2011) 103003, <https://link.aps.org/doi/10.1103/PhysRevD.84.103003>.
- [114] ANITA Collaboration, P. W. Gorham et al., *The Antarctic Impulsive Transient Antenna Ultra-high Energy Neutrino Detector Design, Performance, and Sensitivity for 2006-2007 Balloon Flight*, Astropart. Phys. **32** (2009) 10–41, [arXiv:0812.1920](https://arxiv.org/abs/0812.1920) [astro-ph].
- [115] H. Schoorlemmer et al., *Energy and Flux Measurements of Ultra-High Energy Cosmic Rays Observed During the First ANITA Flight*, Astropart. Phys. **77** (2016) 32–43, [arXiv:1506.05396](https://arxiv.org/abs/1506.05396) [astro-ph.HE].
- [116] RNO-G Collaboration, J. A. Aguilar et al., *Design and Sensitivity of the Radio Neutrino Observatory in Greenland (RNO-G)*, JINST **16** no. 03, (2021) P03025, [arXiv:2010.12279](https://arxiv.org/abs/2010.12279) [astro-ph.IM], [Erratum: JINST 18, E03001 (2023)].
- [117] IceCube-Gen2 Collaboration, M. G. Aartsen et al., *IceCube-Gen2: the window to the extreme Universe*, J. Phys. G **48** no. 6, (2021) 060501, [arXiv:2008.04323](https://arxiv.org/abs/2008.04323) [astro-ph.HE].
- [118] R. Lahmann, *Status and recent results of the acoustic neutrino detection test system AMADEUS*, Nuclear Instruments and Methods in Physics Research Section A: Accelerators, Spectrometers, Detectors and Associated Equipment **662** (2012) S216–S221, <https://www.sciencedirect.com/science/article/pii/S016890021002704X>, 4th International workshop on Acoustic and Radio EeV Neutrino detection Activities.

- [119] T. Karg, *Status and recent results of the South Pole Acoustic Test Setup*, Nuclear Instruments and Methods in Physics Research Section A: Accelerators, Spectrometers, Detectors and Associated Equipment **662** (2012) S36–S41, <http://dx.doi.org/10.1016/j.nima.2010.10.122>.
- [120] A. Marinelli, P. Migliozi, and A. Simonelli, *Acoustic neutrino detection in a Adriatic multidisciplinary observatory (ANDIAMO)*, Astroparticle Physics **143** (2022) 102760, <http://dx.doi.org/10.1016/j.astropartphys.2022.102760>.
- [121] Radar Echo Telescope Collaboration, S. Prohira et al., *The Radar Echo Telescope for Cosmic Rays: Pathfinder experiment for a next-generation neutrino observatory*, Phys. Rev. D **104** no. 10, (2021) 102006, arXiv:2104.00459 [astro-ph.IM].
- [122] IceCube Collaboration, M. G. Aartsen et al., *Search for a diffuse flux of astrophysical muon neutrinos with the IceCube 59-string configuration*, Phys. Rev. D **89** no. 6, (2014) 062007, arXiv:1311.7048 [astro-ph.HE].
- [123] ANTARES Collaboration, A. Albert et al., *ANTARES Search for Point Sources of Neutrinos Using Astrophysical Catalogs: A Likelihood Analysis*, Astrophys. J. **911** no. 1, (2021) 48, arXiv:2012.15082 [astro-ph.HE].
- [124] IceCube Collaboration, R. Abbasi et al., *Search for Point Sources of High Energy Neutrinos with Final Data from AMANDA-II*, Phys. Rev. D **79** (2009) 062001, arXiv:0809.1646 [astro-ph].
- [125] Baikal-GVD Collaboration, V. A. Allakhverdyan et al., *Search for directional associations between baikal gigaton volume detector neutrino-induced cascades and high-energy astrophysical sources*, Mon. Not. Roy. Astron. Soc. **526** no. 1, (2023) 942–951, arXiv:2307.07327 [astro-ph.HE].
- [126] D. Eichler, *High-energy neutrino astronomy-A probe of galactic nuclei*, Astrophysical Journal, Part 1, vol. 232, Aug. 15, 1979, p. 106–112. **232** (1979) 106–112.
- [127] V. Berezhinsky and V. Ginzburg, *On high-energy neutrino radiation of quasars and active galactic nuclei*, Monthly Notices of the Royal Astronomical Society **194** no. 1, (1981) 3–14.
- [128] LIGO Scientific Collaboration, J. Abadie et al., *Implications For The Origin Of GRB 051103 From LIGO Observations*, Astrophys. J. **755** (2012) 2, arXiv:1201.4413 [astro-ph.HE].
- [129] ANTARES, IceCube, Pierre Auger, LIGO Scientific, Virgo Collaboration, A. Albert et al., *Search for High-energy Neutrinos from Binary Neutron Star Merger GW170817 with ANTARES, IceCube, and the Pierre Auger Observatory*, Astrophys. J. Lett. **850** no. 2, (2017) L35, arXiv:1710.05839 [astro-ph.HE].

-
- [130] SNEWS Collaboration, S. Al Kharusi et al., *SNEWS 2.0: a next-generation supernova early warning system for multi-messenger astronomy*, New J. Phys. **23** no. 3, (2021) 031201, arXiv:2011.00035 [astro-ph.HE].
- [131] M. W. E. Smith et al., *The Astrophysical Multimessenger Observatory Network (AMON)*, Astropart. Phys. **45** (2013) 56–70, arXiv:1211.5602 [astro-ph.HE].
- [132] Pierre Auger Collaboration, A. Aab et al., *Multi-Messenger Physics with the Pierre Auger Observatory*, Front. Astron. Space Sci. **6** (2019) 24, arXiv:1904.11918 [astro-ph.HE].
- [133] IceCube, Pierre Auger, Telescope Array, Auger, ANTARES Collaboration, A. Albert et al., *Search for Spatial Correlations of Neutrinos with Ultra-high-energy Cosmic Rays*, Astrophys. J. **934** no. 2, (2022) 164, arXiv:2201.07313 [astro-ph.HE].
- [134] W. Heitler, *The quantum theory of radiation*. Courier Corporation, 1984.
- [135] J. Matthews, *A Heitler model of extensive air showers*, Astroparticle Physics **22** no. 5, (2005) 387–397, <https://www.sciencedirect.com/science/article/pii/S0927650504001598>.
- [136] J. Alvarez-Muñiz, R. Engel, T. K. Gaisser, J. A. Ortiz, and T. Stanev, *Hybrid simulations of extensive air showers*, Phys. Rev. D **66** (2002) 033011, <https://link.aps.org/doi/10.1103/PhysRevD.66.033011>.
- [137] T. Pierog and K. Werner, *Muon Production in Extended Air Shower Simulations*, Phys. Rev. Lett. **101** (2008) 171101, arXiv:astro-ph/0611311.
- [138] J. Linsley, *Proc. 15th ICRC, Plovdiv,*.
- [139] J. Fowler, L. Fortson, C. Jui, D. Kieda, R. Ong, C. Pryke, and P. Sommers, *A measurement of the cosmic ray spectrum and composition at the knee*, Astroparticle Physics **15** no. 1, (2001) 49–64, [http://dx.doi.org/10.1016/S0927-6505\(00\)00139-0](http://dx.doi.org/10.1016/S0927-6505(00)00139-0).
- [140] T. Wibig, *Testing the superposition model in small CORSIKA shower simulations*, Journal of Physics G: Nuclear and Particle Physics **49** no. 3, (2022) 035201, <http://dx.doi.org/10.1088/1361-6471/ac4da7>.
- [141] J.-S. Li, D.-H. Zhang, H.-L. Li, and N. Yasuda, *Projectile fragmentation of 500AMeV 56Fe in nuclear emulsion*, Nuclear Instruments and Methods in Physics Research Section B: Beam Interactions with Materials and Atoms **307** (2013) 503–506, <https://www.sciencedirect.com/science/article/pii/S0168583X13000657>, The 18th International Conference on Ion Beam Modifications of Materials (IBMM2012).

- [142] J. Albrecht, L. Cazon, H. Dembinski, A. Fedynitch, K.-H. Kampert, T. Pierog, W. Rhode, D. Soldin, B. Spaan, R. Ulrich, and M. Unger, *The Muon Puzzle in cosmic-ray induced air showers and its connection to the Large Hadron Collider*, *Astrophysics and Space Science* **367** no. 3, (2022), <http://dx.doi.org/10.1007/s10509-022-04054-5>.
- [143] L. D. Landau and I. Pomeranchuk, *Limits of applicability of the theory of bremsstrahlung electrons and pair production at high-energies*, *Dokl. Akad. Nauk Ser. Fiz.* **92** (1953) 535–536.
- [144] A. B. Migdal, *Bremsstrahlung and Pair Production in Condensed Media at High Energies*, *Phys. Rev.* **103** (1956) 1811–1820, <https://link.aps.org/doi/10.1103/PhysRev.103.1811>.
- [145] A. Sandrock, J.-M. Alameddine, and F. Riehn, *Validation of Electromagnetic Showers in CORSIKA 8*, 2023. <https://arxiv.org/abs/2308.07112>.
- [146] T. K. Gaisser and A. M. Hillas, *Reliability of the Method of Constant Intensity Cuts for Reconstructing the Average Development of Vertical Showers*, Jan., 1977.
- [147] K. Greisen, *Cosmic Ray Showers*, *Annual Review of Nuclear and Particle Science* **10** no. Volume 10., (1960) 63–108, <https://www.annualreviews.org/content/journals/10.1146/annurev.ns.10.120160.000431>.
- [148] K. Kamata and J. Nishimura, *The Lateral and the Angular Structure Functions of Electron Showers*, *Progress of Theoretical Physics Supplement* **6** (1958) 93–155, <https://academic.oup.com/ptps/article-pdf/doi/10.1143/PTPS.6.93/5270594/6-9> <https://doi.org/10.1143/PTPS.6.93>.
- [149] A. M. Hillas, *Angular and energy distributions of charged particles in electron-photon cascades in air*, *Journal of Physics G: Nuclear Physics* **8** no. 10, (1982) 1461, <https://dx.doi.org/10.1088/0305-4616/8/10/016>.
- [150] A. Fedosimova, P. Kharchevnikov, I. Lebedev, and A. Temiraliev, *Applying universality in the development of cascade processes for the research of high energy cosmic particles in space experiments*, *EPJ Web Conf.* **145** (2017) 10004.
- [151] A. Bridgeman, *Shower universality reconstruction of data from the Pierre Auger Observatory and validations with hadronic interaction models*, *PoS ICRC2017* (2017) 323.
- [152] R. Ulrich, J. Blümer, R. Engel, F. Schüssler, and M. Unger, *On the measurement of the proton-air cross section using air shower data*, *New Journal of Physics* **11** no. 6, (2009) 065018, <https://dx.doi.org/10.1088/1367-2630/11/6/065018>.

-
- [153] L. Cazon, R. Conceição, M. A. Martins, and F. Riehn, *Proton-air interactions at ultra-high energies in muon-depleted air showers with different depths*, 2024. <https://arxiv.org/abs/2406.08620>.
- [154] H. E. Bergeson, G. L. Cassiday, T. W. Chiu, D. A. Cooper, J. W. Elbert, E. C. Loh, D. Steck, W. J. West, J. Linsley, and G. W. Mason, *Measurement of light emission from remote cosmic-ray air showers*, *Physical Review Letters* **39** (1977) 847–849.
- [155] R. Baltrusaitis, R. Cady, G. Cassiday, R. Cooperv, J. Elbert, P. Gerhardy, S. Ko, E. Loh, M. Salamon, D. Steck, and P. Sokolsky, *The Utah Fly’s Eye detector*, *Nuclear Instruments and Methods in Physics Research Section A: Accelerators, Spectrometers, Detectors and Associated Equipment* **240** no. 2, (1985) 410–428, <https://www.sciencedirect.com/science/article/pii/0168900285906588>.
- [156] R. Baltrusaitis, G. Cassiday, R. Cooper, B. Dawson, J. Elbert, B. Fick, D. Liebing, E. Loh, P. Sokolsky, and D. Steck, *The Fly’s Eye detector: Present and future*, *Nuclear Instruments and Methods in Physics Research Section A: Accelerators, Spectrometers, Detectors and Associated Equipment* **264** no. 1, (1988) 87–92, <https://www.sciencedirect.com/science/article/pii/0168900288911072>.
- [157] P. A. Cherenkov, *Visible luminescence of pure liquids under the influence of γ -radiation*, *Dokl. Akad. Nauk SSSR* **2** no. 8, (1934) 451–454.
- [158] M. Dyakonov, S. Knurenko, V. Kolosov, D. Krasilnikov, F. Lischenyuk, I. Sleptsov, and S. Nikolsky, *The use of Cherenkov detectors at the Yakutsk cosmic ray extensive air shower array*, *Nuclear Instruments and Methods in Physics Research Section A: Accelerators, Spectrometers, Detectors and Associated Equipment* **248** no. 1, (1986) 224–226, <https://www.sciencedirect.com/science/article/pii/0168900286905188>.
- [159] L. Kuzmichev et al., *Cherenkov EAS arrays in the Tunka astrophysical center: From Tunka-133 to the TAIGA gamma and cosmic ray hybrid detector*, *Nucl. Instrum. Meth. A* **952** (2020) 161830.
- [160] J. Cortina, F. Goebel, and T. Schweizer, *Technical Performance of the MAGIC Telescopes*, 2009. <https://arxiv.org/abs/0907.1211>.
- [161] F. D. Kahn and I. Lerche, *Radiation from Cosmic Ray Air Showers*, *Proceedings of the Royal Society of London Series A* **289** no. 1417, (1966) 206–213.
- [162] H. R. Allan, R. W. Clay, and J. K. Jones, *RADIO PULSES FROM EXTENSIVE AIR SHOWERS.*, *Nature (London)* 227: 1116-18 (12 Sep 1970). (1970), <https://www.osti.gov/biblio/4100652>.

- [163] T. Huege, *Radio detection of cosmic ray air showers in the digital era*, Physics Reports **620** (2016) 1–52,
<http://dx.doi.org/10.1016/j.physrep.2016.02.001>.
- [164] LOFAR Collaboration, M. P. van Haarlem et al., *LOFAR: The LOw-Frequency ARray*, Astron. Astrophys. **556** (2013) A2, arXiv:1305.3550 [astro-ph.IM].
- [165] Pierre Auger Collaboration, A. Aab et al., *Energy Estimation of Cosmic Rays with the Engineering Radio Array of the Pierre Auger Observatory*, Phys. Rev. D **93** no. 12, (2016) 122005, arXiv:1508.04267 [astro-ph.HE].
- [166] K. Fang et al., *The Giant Radio Array for Neutrino Detection (GRAND): Present and Perspectives*, PoS ICRC2017 (2018) 996, arXiv:1708.05128 [astro-ph.IM].
- [167] W. Galbraith and J. V. Jelley, *Light Pulses from the Night Sky associated with Cosmic Rays*, Nature **171** no. 4347, (1953) 349–350.
- [168] E. Bagge, E. Böhm, R. Fritze, U. J. Roose, M. Samorski, C. Schnier, R. Staubert, K. O. Thielheim, J. Trümper, L. Wiedecke, and W. Wolter, *The extensive air shower experiment at Kiel*,
<https://ui.adsabs.harvard.edu/abs/1965ICRC....2..738B>.
- [169] J. Linsley, L. Scarsi, and B. Rossi, *Extremely energetic cosmic-ray event*, Physical Review Letters **6** no. 9, (1961) 485 – 487,
<https://www.scopus.com/inward/record.uri?eid=2-s2.0-4244058634&doi=10.1103%2fPhysRevLett.6.485&partnerID=40&md5=5741b7821c94f79cff419ba9768039c8>, Cited by: 62.
- [170] A. Bueno, A. Gascón, J. Illana, and M. Masip, *Propagation of B mesons in the atmosphere*, Journal of Cosmology and Astroparticle Physics **2012** (2011) .
- [171] S. Y. BenZvi et al., *The Lidar System of the Pierre Auger Observatory*, Nucl. Instrum. Meth. A **574** (2007) 171–184, arXiv:astro-ph/0609063.
- [172] B. Fick, M. Malek, J. Matthews, R. Meyhandan, M. Mostafa, M. Roberts, and P. Sommers, *The Central Laser Facility at the Pierre Auger Observatory*, Journal of Instrumentation **1** (2006) P11003.
- [173] L. Wiencke and (for the Pierre Auger Collaboration), *Atmospheric calorimetry above 1019 ev: Shooting lasers at the Pierre Auger Cosmic-Ray Observatory*, Journal of Physics: Conference Series **160** no. 1, (2009) 012037,
<https://dx.doi.org/10.1088/1742-6596/160/1/012037>.
- [174] J. R. Hörandel, *Status and prospects of the Auger Radio Detector*, PoS ECRS (2023) 095.

-
- [175] Pierre Auger Collaboration, A. Abdul Halim et al., *Status and Performance of the Underground Muon Detector of the Pierre Auger Observatory*, PoS **ICRC2023** (2023) 267.
- [176] Pierre Auger Collaboration, G. Cataldi, *The upgrade of the Pierre Auger Observatory with the Scintillator Surface Detector*, PoS **ICRC2021** (2021) 251.
- [177] Pierre Auger Collaboration, J. Abraham et al., *The Fluorescence Detector of the Pierre Auger Observatory*, Nucl. Instrum. Meth. A **620** (2010) 227–251, arXiv:0907.4282 [astro-ph.IM].
- [178] J. Rosado, F. Blanco, and F. Arqueros, *On the absolute value of the air-fluorescence yield*, Astropart. Phys. **55** (2014) 51–62, arXiv:1401.4310 [astro-ph.IM].
- [179] F. Salamida, *The analysis of hybrid events in the Pierre Auger Observatory*, Nuclear Instruments and Methods in Physics Research Section A: Accelerators, Spectrometers, Detectors and Associated Equipment **588** no. 1, (2008) 207–210, <https://www.sciencedirect.com/science/article/pii/S0168900208000685>, Proceedings of the First International Conference on Astroparticle Physics.
- [180] Pierre Auger Collaboration, A. Aab et al., *A Three Year Sample of Almost 1600 Elves Recorded Above South America by the Pierre Auger Cosmic-Ray Observatory*, Earth Space Sci. **7** no. 4, (2020) e2019EA000582.
- [181] Pierre Auger Collaboration, I. Allekotte et al., *The Surface Detector System of the Pierre Auger Observatory*, Nucl. Instrum. Meth. A **586** (2008) 409–420, arXiv:0712.2832 [astro-ph].
- [182] Pierre Auger Collaboration, X. Bertou et al., *Calibration of the surface array of the Pierre Auger Observatory*, Nucl. Instrum. Meth. A **568** (2006) 839–846, arXiv:2102.01656 [astro-ph.HE].
- [183] Pierre Auger Collaboration, M. Aglietta et al., *Response of the Pierre Auger Observatory water Cherenkov detectors to muons*, in *29th International Cosmic Ray Conference*. 7, 2005.
- [184] Pierre Auger Collaboration, S. Dasso and H. Asorey, *The scaler mode in the Pierre Auger Observatory to study heliospheric modulation of cosmic rays*, Adv. Space Res. **49** (2012) 1563–1569, arXiv:1204.6196 [astro-ph.SR].
- [185] P. Billoir, *New proposal to improve local trigger of the Surface Detector*, 2011. <https://www.auger.org/gap-notes/>.
- [186] Pierre Auger Collaboration, P. Abreu et al., *AugerPrime Upgraded Electronics*, PoS **ICRC2021** (2021) 230.

- [187] Pierre Auger Collaboration, A. Abdul Halim et al., *The dynamic range of the upgraded surface-detector stations of AugerPrime*, PoS **ICRC2023** (2023) 343.
- [188] Pierre Auger Collaboration, A. Aab et al., *Design and implementation of the AMIGA embedded system for data acquisition*, JINST **16** no. 07, (2021) T07008, arXiv:2101.11747 [astro-ph.IM].
- [189] Pierre Auger Collaboration, A. Abdul Halim et al., *Search for primary photons at tens of PeV with the Pierre Auger Observatory*, PoS **ICRC2023** (2023) 238.
- [190] S. Argiro, S. L. C. Barroso, J. Gonzalez, L. Nellen, T. C. Paul, T. A. Porter, L. Prado, Jr., M. Roth, R. Ulrich, and D. Veberic, *The Offline Software Framework of the Pierre Auger Observatory*, Nucl. Instrum. Meth. A **580** (2007) 1485–1496, arXiv:0707.1652 [astro-ph].
- [191] Pierre Auger Collaboration, A. Abdul Halim et al., *Update on the Offline Framework for AugerPrime and production of reference simulation libraries using the VO Auger grid resources*, PoS **ICRC2023** (2023) 248.
- [192] D. Heck, J. Knapp, J. N. Capdevielle, G. Schatz, and T. Thouw, *CORSIKA: A Monte Carlo code to simulate extensive air showers*,.
- [193] S. J. Sciutto, *AIRES: A system for air shower simulations*, arXiv:astro-ph/9911331.
- [194] R. Brun and F. Rademakers, *ROOT: An object oriented data analysis framework*, Nucl. Instrum. Meth. A **389** (1997) 81–86.
- [195] *Python Instrumentation Kit*, <https://github.com/HDembinski/pyik>.
- [196] J. Pivarski et al., *Uproot*, 2024.
- [197] G. Corcella, I. G. Knowles, G. Marchesini, S. Moretti, K. Odagiri, P. Richardson, M. H. Seymour, and B. R. Webber, *HERWIG 6: An Event generator for hadron emission reactions with interfering gluons (including supersymmetric processes)*, JHEP **01** (2001) 010, arXiv:hep-ph/0011363.
- [198] S. Ostapchenko, *Monte Carlo treatment of hadronic interactions in enhanced Pomeron scheme: I. QGSJET-II model*, Phys. Rev. D **83** (2011) 014018, arXiv:1010.1869 [hep-ph].
- [199] F. Riehn, R. Engel, A. Fedynitch, T. K. Gaisser, and T. Stanev, *Hadronic interaction model Sibyll 2.3d and extensive air showers*, Phys. Rev. D **102** no. 6, (2020) 063002, arXiv:1912.03300 [hep-ph].

-
- [200] T. Pierog, I. Karpenko, J. M. Katzy, E. Yatsenko, and K. Werner, *EPOS LHC: Test of collective hadronization with data measured at the CERN Large Hadron Collider*, Phys. Rev. C **92** no. 3, (2015) 034906, arXiv:1306.0121 [hep-ph].
- [201] A. Ferrari, P. R. Sala, A. Fasso, and J. Ranft, *FLUKA: A multi-particle transport code (Program version 2005)*,.
- [202] G. Battistoni et al., *Overview of the FLUKA code*, Annals Nucl. Energy **82** (2015) 10–18.
- [203] W. R. Nelson and Y. Namito, *THE EGS4 CODE SYSTEM: SOLUTION OF gamma-ray AND ELECTRON TRANSPORT PROBLEMS*, 2, 1990.
- [204] Pierre Auger Collaboration, P. Abreu et al., *Description of Atmospheric Conditions at the Pierre Auger Observatory using the Global Data Assimilation System (GDAS)*, Astropart. Phys. **35** (2012) 591–607, arXiv:1201.2276 [astro-ph.HE].
- [205] A. M. Hillas, *Shower simulation: Lessons from MOCCA*, Nucl. Phys. B Proc. Suppl. **52** (1997) 29–42.
- [206] D. Heck and J. Knapp, *Upgrade of the Monte Carlo code CORSIKA to simulate extensive air showers with energies $> 10^{20}$ eV*, in *Spring Meeting of the Germany Physical Society (DPG) on Particle Physics (In German)*. 7, 1998.
- [207] Pierre Auger Collaboration, M. Kobal, *A thinning method using weight limitation for air-shower simulations*, Astropart. Phys. **15** (2001) 259–273.
- [208] *EGI, European Grid Infrastructure.*, <http://www.egi.eu/>.
- [209] Pierre Auger Collaboration, J. Lozano Bahilo, *Mass production of extensive air showers for the Pierre Auger Collaboration using Grid technology*, J. Phys. Conf. Ser. **368** (2012) 012015.
- [210] B. T. Stokes, R. Cady, D. Ivanov, J. N. Matthews, and G. B. Thomson, *Dethinning Extensive Air Shower Simulations*, Astropart. Phys. **35** (2012) 759–766, arXiv:1104.3182 [astro-ph.IM].
- [211] GEANT4 Collaboration, S. Agostinelli et al., *GEANT4—a simulation toolkit*, Nucl. Instrum. Meth. A **506** (2003) 250–303.
- [212] J. Allison et al., *Geant4 developments and applications*, IEEE Trans. Nucl. Sci. **53** (2006) 270.
- [213] J. Allison et al., *Recent developments in Geant4*, Nucl. Instrum. Meth. A **835** (2016) 186–225.

- [214] D. Veberic, *Estimation of the Total Signal in Saturated Stations of Pierre Auger Surface Detector*, 2013.
- [215] Pierre Auger Collaboration, A. Aab et al., *Reconstruction of events recorded with the surface detector of the Pierre Auger Observatory*, JINST **15** no. 10, (2020) P10021, [arXiv:2007.09035 \[astro-ph.IM\]](#).
- [216] X. B. C. Medina, *GAP Note 2004-030 (Auger key protected)*,.
- [217] R. Colalillo and R. Mussa, *Observation of high energy radiation in the Surface Detectors of the Pierre Auger Observatory in correspondance with lightning strikes*,.
- [218] F. James and M. Roos, *Minuit: A System for Function Minimization and Analysis of the Parameter Errors and Correlations*, Comput. Phys. Commun. **10** (1975) 343–367.
- [219] *An illustrative example of Fisher’s linear discriminant*, <https://sthalles.github.io/fisher-linear-discriminant/>.
- [220] *Conversations with Jaime Alvarez-Muñiz*,.
- [221] *Scikit-learn: Linear Discriminant Analysis*, <https://scikit-learn.org/0.16/modules/generated/sklearn.lda.LDA.html>.
- [222] Pierre Auger Collaboration, R. Sato, *Long term performance of the surface detectors of the Pierre Auger Observatory*,.
- [223] Pierre Auger Collaboration, A. Abdul Halim et al., *The Time Evolution of the Surface Detector of the Pierre Auger Observatory*, PoS **ICRC2023** (2023) 266.
- [224] Pierre Auger Collaboration, J. Abraham et al., *Trigger and Aperture of the Surface Detector Array of the Pierre Auger Observatory*, Nucl. Instrum. Meth. A **613** (2010) 29–39, [arXiv:1111.6764 \[astro-ph.IM\]](#).
- [225] A. Cooper-Sarkar, P. Mertsch, and S. Sarkar, *The high energy neutrino cross-section in the Standard Model and its uncertainty*, JHEP **08** (2011) 042, [arXiv:1106.3723 \[hep-ph\]](#).
- [226] Pierre Auger Collaboration, A. Aab et al., *Muons in Air Showers at the Pierre Auger Observatory: Measurement of Atmospheric Production Depth*, Phys. Rev. D **90** no. 1, (2014) 012012, [arXiv:1407.5919 \[hep-ex\]](#), [Addendum: Phys.Rev.D 90, 039904 (2014), Erratum: Phys.Rev.D 92, 019903 (2015)].
- [227] G. J. Feldman and R. D. Cousins, *A Unified approach to the classical statistical analysis of small signals*, Phys. Rev. D **57** (1998) 3873–3889, [arXiv:physics/9711021](#).

- [228] Gammapy Collaboration, A. Donath et al., *Gammapy: A Python package for gamma-ray astronomy*, Astron. Astrophys. **678** (2023) A157, arXiv:2308.13584 [astro-ph.IM].
- [229] W. A. Rolke and A. M. Lopez, *Confidence intervals and upper bounds for small signals in the presence of background noise*, Nucl. Instrum. Meth. A **458** (2001) 745–758, arXiv:hep-ph/0005187.
- [230] W. A. Rolke, A. M. Lopez, and J. Conrad, *Limits and confidence intervals in the presence of nuisance parameters*, Nucl. Instrum. Meth. A **551** (2005) 493–503, arXiv:physics/0403059.
- [231] *TRolke Class Reference*, <https://root.cern/doc/v628/classTRolke.html>.
- [232] J. Conrad, O. Botner, A. Hallgren, and C. Perez de los Heros, *Including systematic uncertainties in confidence interval construction for Poisson statistics*, Phys. Rev. D **67** (2003) 012002, arXiv:hep-ex/0202013.
- [233] J. Conrad and F. Tegenfeldt, *Likelihood ratio intervals with Bayesian treatment of uncertainties: Coverage, power and combined experiments*, arXiv:physics/0511055.
- [234] Pierre Auger Collaboration, A. Aab et al., *Observation of a Large-scale Anisotropy in the Arrival Directions of Cosmic Rays above 8×10^{18} eV*, Science **357** no. 6537, (2017) 1266–1270, arXiv:1709.07321 [astro-ph.HE].

Testing hadronic models

This appendix includes the comparison of residuals obtained from alignment using the previously used method and Millepede. The reduced chi-square comparison plots for the two methods were shown earlier. It also includes the residual versus position plots for the Micromega detectors.

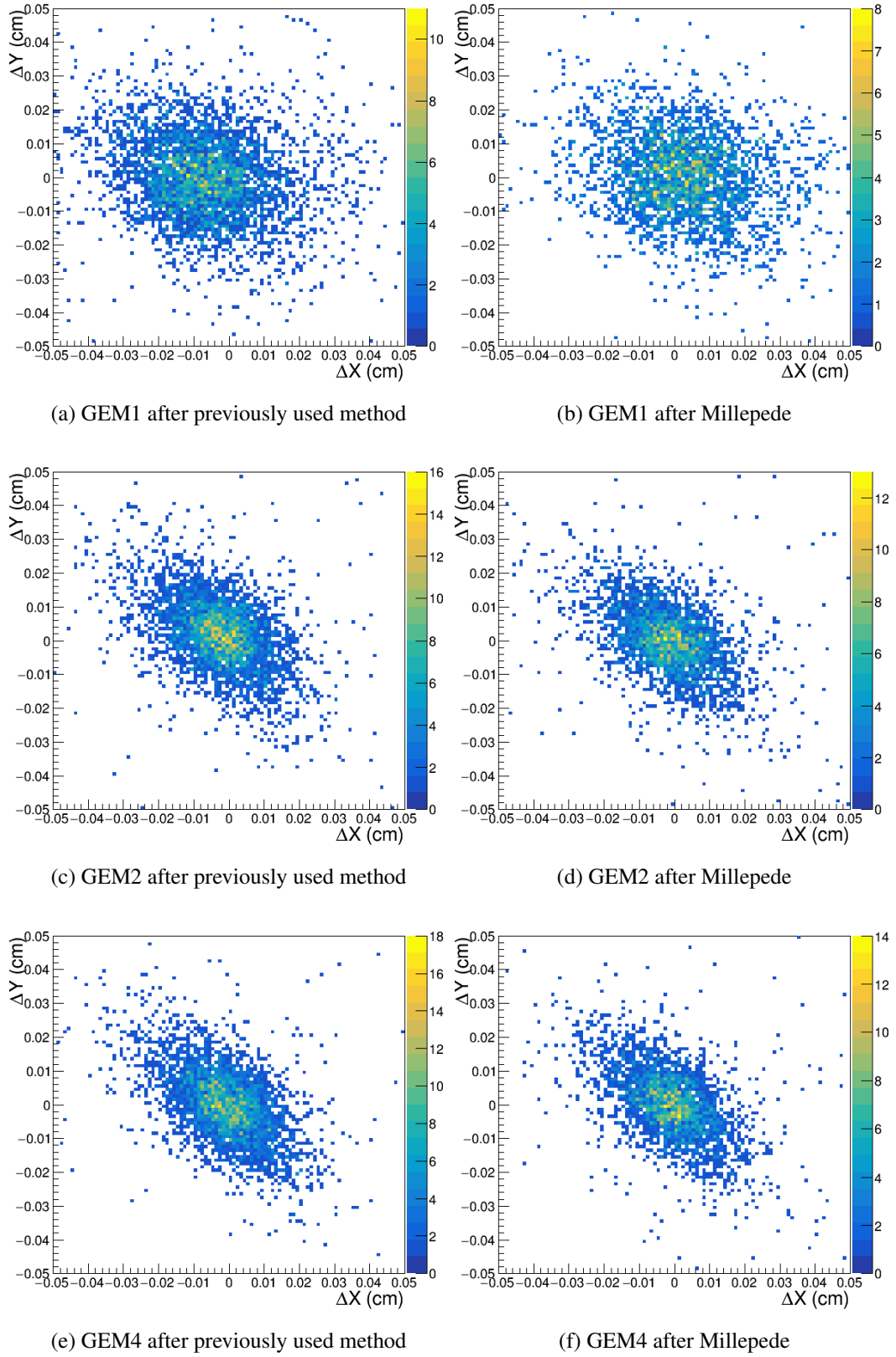
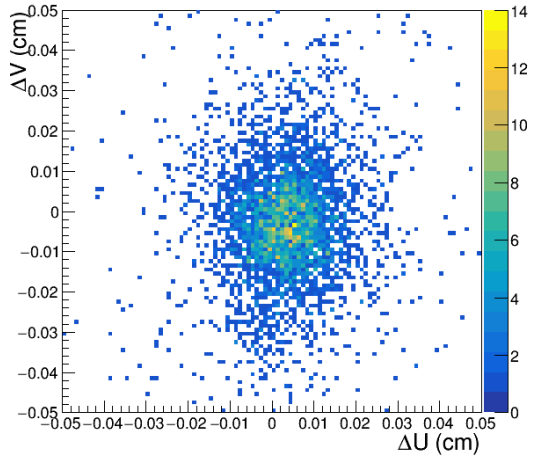
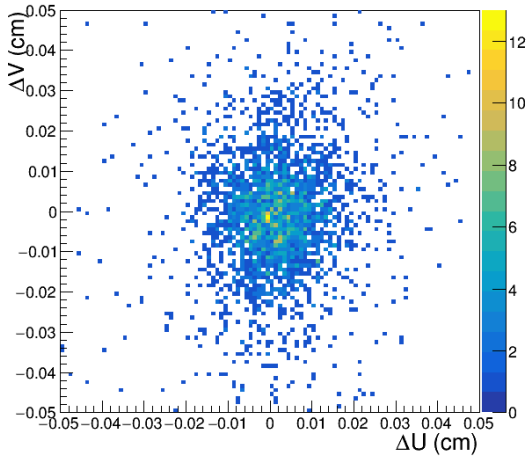


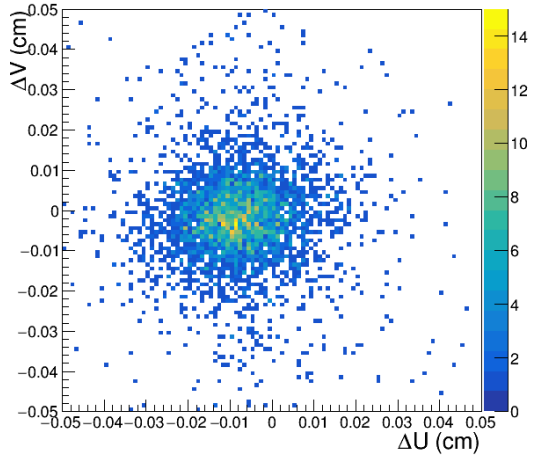
Figure A.1: Residual of GEM detectors.



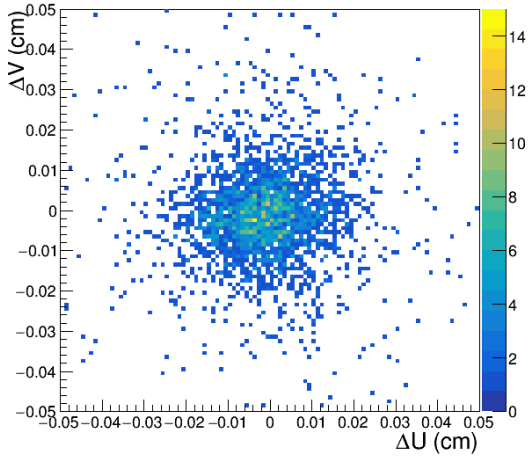
(a) MM1 after previously used method



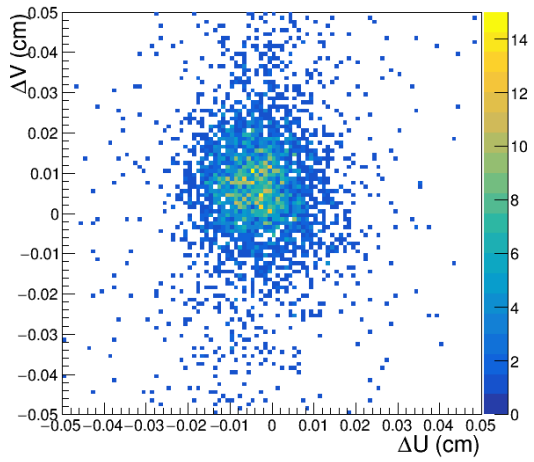
(b) MM1 after Millepede



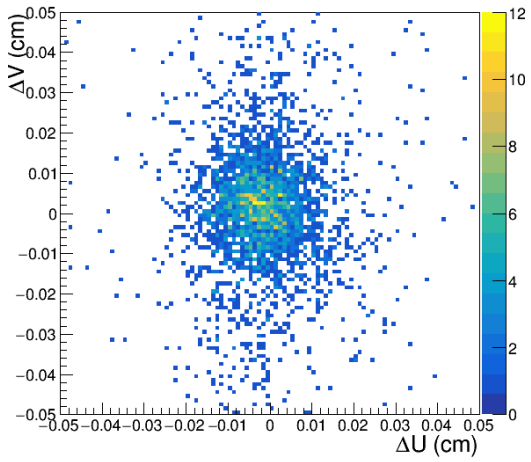
(c) MM2 after previously used method



(d) MM2 after Millepede



(e) MM3 after previously used method



(f) MM3 after Millepede

Figure A.2: Residual of Micromega detectors.

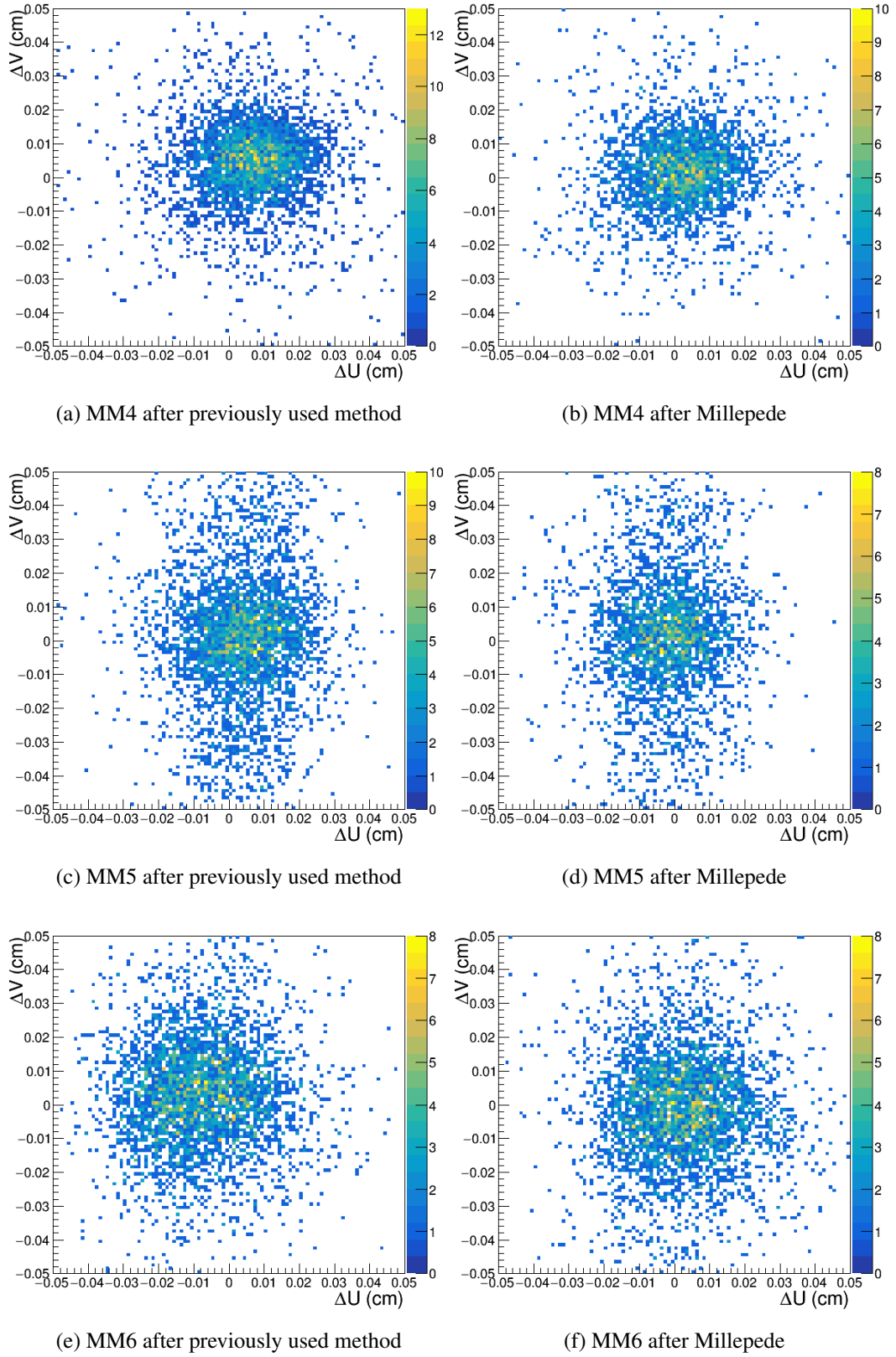
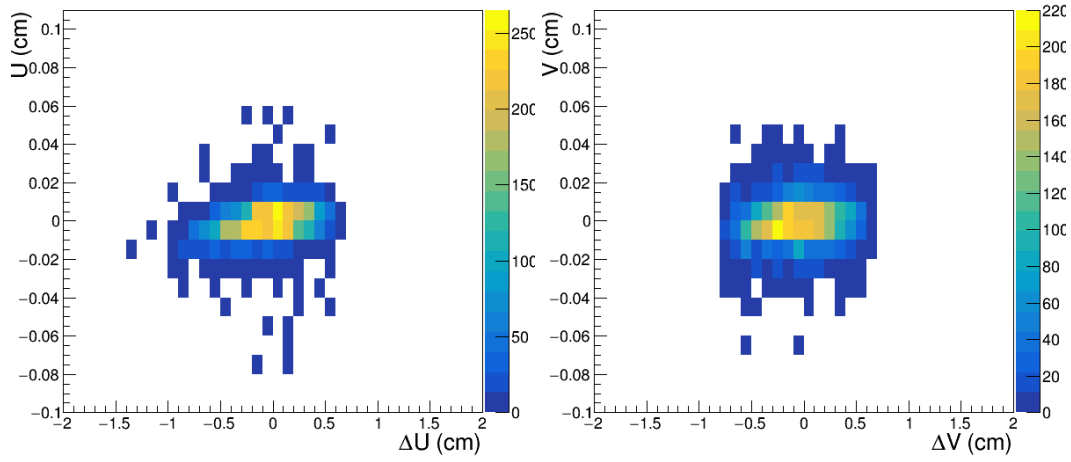
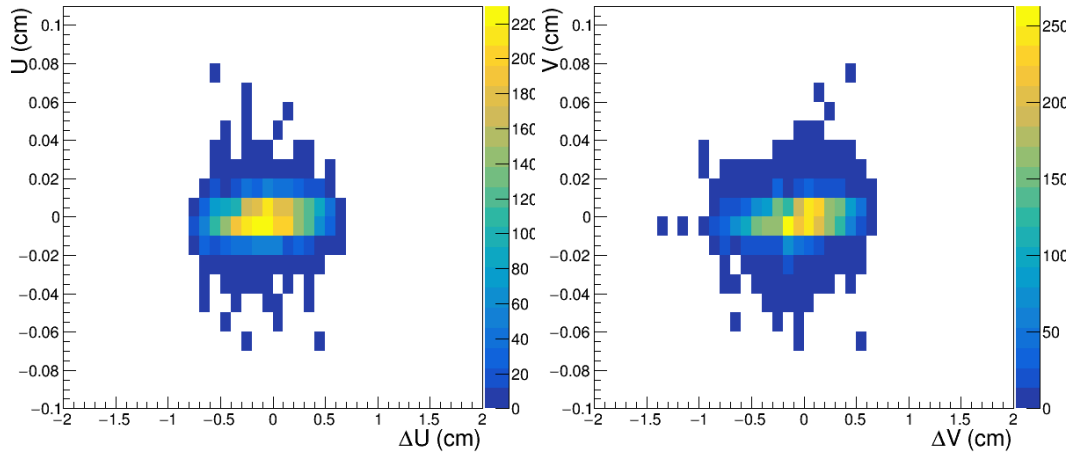


Figure A.3: Residual of Micromega detectors.



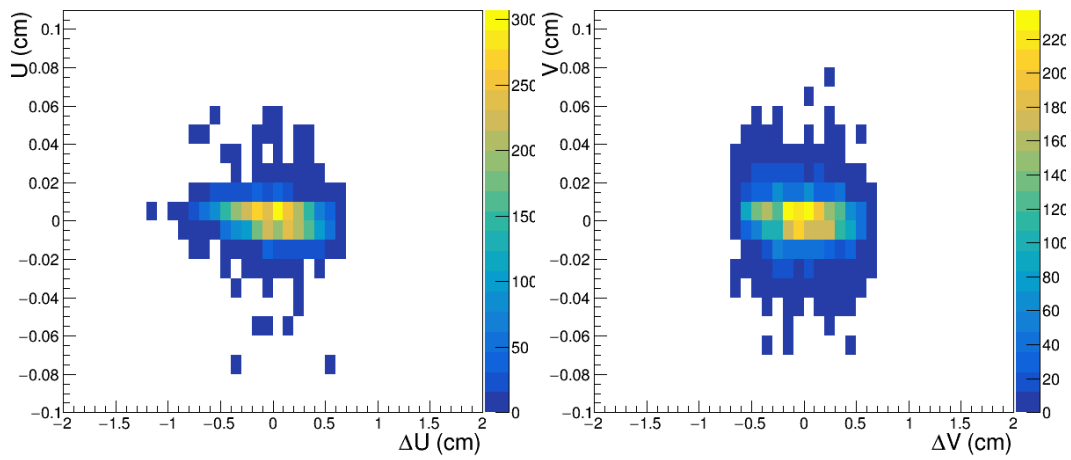
(a) MM1 U plane

(b) MM1 V plane



(c) MM2 U plane

(d) MM2 V plane



(e) MM3 U plane

(f) MM3 V plane

Figure A.4: Residual vs position for Micromega detectors

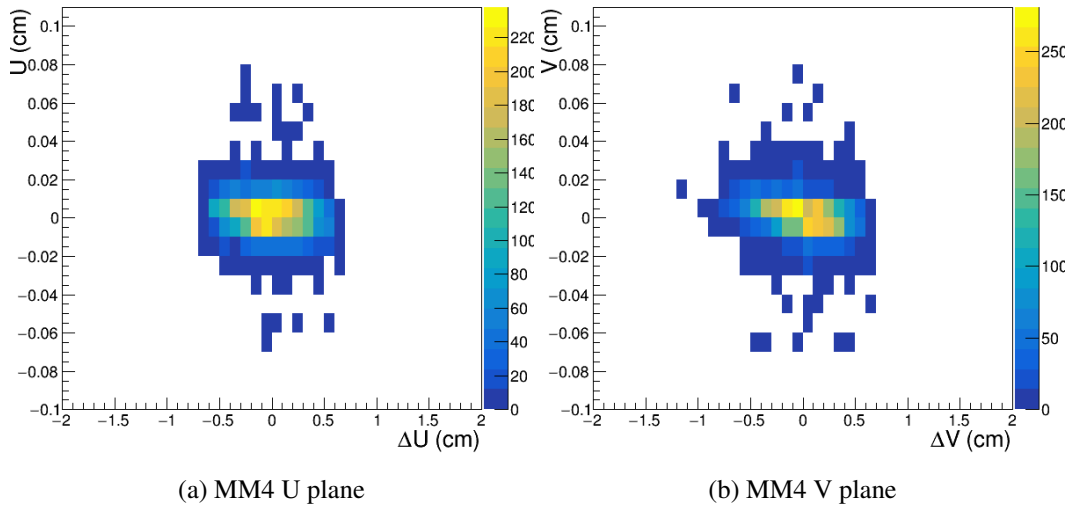


Figure A.5: Residual vs position for MM4

APPENDIX B

Adapting DGH analysis to current Offline

MX01U1	101	0	1	11	149999	0	1	0.001012	4.7205	-0.2347	-17593.5	4.7205	-0.2347	-17593.5	4.7205	-0.2347	-17593.5	0	0	0
Detector Name	Detector -ID	Channel Number	Track -ID	Particle-ID	Particle Energy (MeV)	Time	Beta	Energy Deposited (MeV)	Hit position (X) (cm)	Hit position (Y) (cm)	Hit position (Z) (cm)	Primary hit pos. (X) (cm)	Primary hit pos. (Y) (cm)	Primary hit pos. (Z) (cm)	Last hit pos. (X) (cm)	Last hit pos. (Y) (cm)	Last hit pos. (Z) (cm)	Momentum (X)	Momentum (Y)	Momentum (Z)

Figure B.1: Snippet of the format fed to CORAL

The above figure is a snippet of the modified format which was fed to CORAL for the tracking detector. The line in black is the part which was actually fed to CORAL in a compressed plain text format. The second line in the figure gives a description about the values. The green colour is an indication that the information was available in the output of the simulation while the ones in red were not available and were substituted by some reasonable values. As it can be seen in the figure each plane of the tracking detector is fed individually. For CORAL, the planes were exactly replicated with a shifted z position for each hit. The format for the calorimeters is exactly the same with only the information about the detector name, detector-ID and energy deposited available from the original simulation while the rest is replaced with zero.

List of Figures

1.1	Positron fraction measured by PAMELA (red) along with a theoretical model (black) []	1
2.1	Visible mode	24
2.2	Invisible mode	24
2.3	Current limits for invisible mode for 90% C.L. exclusion region in the $(m_{A'}, \epsilon)$ plane []	25
2.4	Current limits for invisible mode for 90% C.L. exclusion region in the $(m_{A'}, \epsilon)$ plane. The blue plane is with 2017 data and the dotted line is with 2017+2018 data for NA64. The red line is the region that might explain the X17 boson [].	25
4.1	Invisible mode setup []	37
4.2	Visible mode setup 2017 []	46
4.3	Visible mode setup 2018-top view []	46
5.1	Left: Strip dimensions of the modules, Right:NA64 Micromega's working principle []	66
5.2	A sketch of GEM field lines [].	67
5.3	Schematic of a triple GEM detector along with the working principle []	67
5.4	Linear regression pictorially.	67
8.1	χ^2_{red} distribution for selected tracks showing the impact of Millepede alignment.	81
A.1	Residual of GEM detectors.	108
A.2	Residual of Micromega detectors.	109
A.3	Residual of Micromega detectors.	110
A.4	Residual vs position for Micromega detectors	111
A.5	Residual vs position for MM4	112
B.1	Snippet of the format fed to CORAL	113